INAUGURAL–DISSERTATION

zur

Erlangung der Doktorwürde

der

Naturwissenschaftlich–Mathematischen

Gesamtfakultät

der Ruprecht–Karls–Universität

Heidelberg

vorgelegt von
Dipl.-Phys. Sven Müller
aus Verden an der Aller

Tag der mündlichen Prüfung: 20. Juni 2012

Morphological, Structural, and Compositional Characterization of Electrodeposited $\mathrm{Bi}_{1-x}\mathrm{Sb}_x$ Nanowires

Gutachter: Prof. Dr. Annemarie Pucci
            Prof. Dr. Reinhard Neumann

Zusammenfassung

$Bi_{1-x}Sb_x$ Nanodrähte mit kontrolliertem Durchmesser (20 bis 200 nm) und kontrollierter Zusammensetzung von $x = 0$ bis 0.5 und $x = 1$ wurden elektrochemisch in geätzten Ionenspurmembranen hergestellt. Diese Nanodrähte sind von Bedeutung für die Untersuchung des Einflusses von sogenannten Quantum-Size-Effekten auf die thermoelektrische Effizienz.

Der Einfluss des Elektrolyten und des Abscheidepotentials auf die elektrochemische Abscheidung von $Bi_{1-x}Sb_x$ in Polymertemplaten aus Polycarbonat (PC) und Polyethylenterephthalat (PET) wurde untersucht. Die Zusammensetzung, die kristalline Orientierung und die Kristallitgröße wurden mit Hilfe von Röntgendiffraktion und Raster- und Transmissionselektronenmikroskopie gemessen. Die Zusammensetzung der Drähte kann durch die Konzentrationen von Bismut und Antimon im Elektrolyten und die Wahl des Abscheidepotentials festgelegt werden. Nanodrähte, die in PET-Membranen hergestellt wurden, zeigten eine rauhere Oberfläche als Nanodrähte, die in PC-Membranen abgeschieden wurden. Dadurch ergibt sich ein neuer Weg, die Oberfläche von Nanodrähten zu strukturieren, um die Oberflächenstreuung von Phononen zu erhöhen, und damit die thermoelektrische Effizienz zu vergrößern.

Der Seebeckkoeffizient und der Temperaturkoeffizient des Widerstandes von Vieldrahtproben wurden in einem Kryostaten bis zu Temperaturen von etwa 30 K gemessen. Der Betrag des Seebeckkoeffizienten nahm mit sinkender Temperature ab und war niedriger als der Wert des entsprechenden makroskopischen Festkörpers.

Abstract

$Bi_{1-x}Sb_x$ nanowires with controlled diameter (20 to 200 nm) and composition over a wide range from $x = 0$ to 0.5 and $x = 1$ were fabricated by electrochemical deposition in etched ion-track templates. These nanowires are interesting for the investigation of the influence of quantum-size effects on the thermoelectric efficiency.

The influence of the electrolyte and the deposition potential on the electrochemical deposition of $Bi_{1-x}Sb_x$ nanowires in polymer templates made of polycarbonate (PC) and poly(ethylene terephthalate) (PET) was investigated. Composition, crystalline orientation, and crystallite size of the nanowires were measured using X-ray diffraction and scanning and transmission electron microscopy. It was demonstrated that the composition of the nanowires can be adjusted by the concentrations of bismuth and antimony in the electrolyte and the deposition potential. Nanowires grown in PET exhibited a pronounced surface roughness compared to the nanowires deposited in PC and offer a novel possibility for the structuring of the nanowire surface to increase the thermoelectrical efficiency by enhanced phonon surface scattering.

Seebeck coefficient and temperature dependence of the resistance of nanowire arrays were measured in a cryostat for temperatures down to ~ 30 K. The absolute value of the Seebeck coefficient decreased with decreasing temperature and was lower than the value of the respective bulk material.

Contents

Contents

1 Introduction

1.1 Overview

Thermoelectric devices are employed for the direct conversion of heat by means of a temperature difference into electrical energy and for the transfer of heat by an electrical current. In 1826, T. J. Seebeck published his work "Ueber die magnetische Polarisation der Metalle und Erze durch Temperaturdifferenz" about his observation that a temperature difference can create a voltage.[1] Decades later, also the Peltier effect and the Kelvin relations were discovered.[2] A century later, in the 1950ies, adequate materials for thermoelectrics were found in compounds based on Bi, Bi_2Te_3, $(Bi,Sb)_2Te_3$, and $Bi_2(Te,Se)_3$.[2] However the efficiency is still not high enough for large scale applications. Thus, modules using thermoelectric effects are niche products used, e.g., for portable refrigerators or radioisotope thermoelectric generators for unmanned satellite missions where the temperature gradient is created by the decay of radioactive substances.[3] The thermoelectric efficiency is expressed by a figure of merit, which in the field of thermoelectrics is defined by

$$ZT = \frac{S^2\sigma}{\kappa}T,$$

being S the Seebeck coefficient, σ the electrical conductivity, κ the thermal conductivity, and T the absolute temperature. For a higher thermoelectric efficiency, materials with reduced κ and enhanced σ and S are demanded. In 1993, Hicks and Dresselhaus proposed a new route to efficient thermoelectric materials via nanosized quantum-wells[4,5] or nanowires.[6,7]

Confinement Great efforts have been made to find low-dimensional materials as thin films (2D), nanowires (1D), and quantum dots (0D) that exhibit enhanced thermoelectric efficiencies. One material class comprises the group V semi-metals and compounds related to Bi_2Te_3.

Due to its large de Broglie wavelength of $300 - 400\,\text{Å}$,[8] quantum-size effects are expected for nanostructures of Bi with comparably large sizes. Furthermore, the mean free path of charge carriers is of the order of $100\,\mu m$, and therefore, exceptionally large.[9,10] Indeed, oscillations in the electrical conductivity due to quantum-size effects were reported for Bi and Sb thin films already in the late

1960ies[11–13] and later.[14,15] For a critical film thickness of 30 nm, a transition from semi-metal to semi-conductor was observed in Bi films.[16] A large magnetoresistance was measured for epitaxially grown thin films.[17] Thermoelectric properties of thin films made of Bi and Sb,[18–20] as well as $Bi_{1-x}Sb_x$[21] were also reported in the literature.

A confinement of the charge carriers in two dimensions leads to quantum wires. Bi nanowires, i.e., wires with a diameter smaller than ~ 100 nm, may already be called quantum wires because the conduction and valence bands are expected to split up into sub-bands due to quantum-confinement.

In 2001, the theoretical modeling of Lin et al.[22] showed promising results for the thermoelectric performance of bismuth nanowires. Based on the same model, Rabin et al. published theoretical calculations of $Bi_{1-x}Sb_x$ nanowires.[23]

However, recently, the calculations were refined, and more sub-bands were regarded.[24] Still, at very low diameters (smaller than ~ 10 nm) quantum-size effects beneficial for the thermoelectric efficiency were expected. Going to larger diameters, the model predicted a minimum in the power factor $S^2\sigma$. A systematic comparison of these calculations with measurements would help to understand and optimize the transport properties of nanomaterials.

Those calculations predict also a semi-metal to semi-conductor transition due to confinement of charge carriers for Bi and $Bi_{1-x}Sb_x$ nanowires. For bismuth nanowires, experimental findings support a semi-metal to semi-conductor transition.[25] Additionally, bulk $Bi_{1-x}Sb_x$ is already a semi-conductor for antimony concentrations x from 0.07 to 0.22.[26,27]

Synthesis   Thin films were prepared by various methods like electrodeposition[28] and molecular beam epitaxy.[21] Textured $Bi_{1-x}Sb_x$ alloys can easily be prepared by electrodeposition, which for thin films was demonstrated by Besse et al.[29,30] and Vereecken et al.[28] Experimentally, systematic *p*- and *n*-doping of $Bi_{0.91}Sb_{0.09}$ thin films with Te and Se and the influence of this doping on the thermoelectric performance was shown by Cho et al.[31] Del Frari et al. reported the preparation of ternary systems of $(Bi_{1-x}Sb_x)_2Te_3$ thin films by pulsed electrodeposition[32] and Liao et al. a method to improve the thermoelectric properties of such thin films by electric current stressing.[33]

In order to electrochemically fabricate nanowires, a template with nanochannels, such as anodic alumina or ion-track etched polymers, can be employed.[34,35] In 2002, Zhang et al. published the preparation of pure Sb nanowires with a pronounced {110} texture.[36] From the point of view of nanostructured nanowires, Dou et al. published interesting results on the preparation of Bi/BiSb superlattice nanowires.[37]

Measurements Despite the promising theoretical calculations, comprehensive and systematic measurements of S, σ, and κ on $Bi_{1-x}Sb_x$ nanowires are scarce, mainly due to the problem of contacting and control of the composition, texture, and structure. The problem of oxide layers inhibiting ohmic contacts to Bi nanowires was addressed by Cronin et al.[38] However, few platforms to contact single nanowires and characterize thermoelectrical properties were presented for InSb,[39] Bi[40–44], or Bi_2Te_3.[45,46]

For Bi nanowires, finite- and quantum-size effects have been observed in the electrical conductivity and in infrared spectra.[25,47–49] Thermoelectric transport properties have been reported also for thicker Bi nano- and sub-µm wires.[50,51]

Experimental data for bismuth nanowire arrays grown by the vapor-phase technique indicated an extremely large Seebeck coefficient of the order of 10^5 µV/K for 9 nm diameter bismuth nanowires.[52] Nikolaeva et al. showed also a strong influence of the wire diameter on the Seebeck coefficient of single sub-µm wires fabricated with the Ulitovsky method.[53]

Moore at al. presented a chip for the characterization of κ for individual Bi nanowires and reported reduced values compared to bulk material.[54] Recently, measurements of κ of individual Bi nanowires were published by Roh et al.[55] They also found that κ is decreasing with decreasing nanowire diameter which was attributed to an enhanced scattering of electrons and phonons at boundaries. For Si nanowires with a rough surface, it was shown that the thermal conductivity was decreased significantly leading to an improved thermoelectric performance.[56,57] It is also of interest to investigate whether such an enhanced phonon surface scattering occurs in $Bi_{1-x}Sb_x$ nanowires. Using PET as template material, the desired surface roughness can be achieved.

Applications In spite of their poor efficiency, the possible applications of thermoelectric devices cover a wide range. They offer a long lifetime because they do not consist of moving parts. They can salvage waste heat and turn it into electrical energy, but they do not emit exhaust gas or dangerous by-products, which makes them non-polluting during operation.

Microstructured infrared sensors based on thermoelectrics already exist,[58–60] and lowering their dimensions enables a higher integration density and a higher efficiency and sensitivity.[61] It might be possible to apply such structures as micro-coolers or dew-point sensors.[62] Micro-generators made of nanowire arrays have already been proposed.[63]

As early as 2003, Lindeberg and Hjort suggested a three-dimensional network for the nanostructuring of thermoelectric devices employing polyimide as template.[64] Successful results with parallel nanowire arrays of Sb and Ni were presented by Yousef et al.[65] Koukharenko et al. followed the general idea depositing Bi_2Te_3 in

polyimide membranes.[66] For the microstructuring of a template, Razpet et al. have transferred the regular pattern of anodic alumina onto SiO_2 by ion beam lithography,[67] and also photolithographic methods have been proposed.[63,68] Patterning the substrate by electron beam was shown by Yun et al.[69] An addressable structure of 25 electrodes, each of $10\,\mu m$ diameter, was presented by Zoski et al.[70] They were able to perform electrochemical experiments on each single electrode.

This Work   In this work, $Bi_{1-x}Sb_x$ nanowires were prepared via electrochemical deposition in ion-track etched templates.[71] As host template, polycarbonate (PC) and poly(ethylene terephthalate) (PET) were employed. Wet chemical etching allowed for an excellent control over the wire diameter over a wide range from the micrometer regime down to $\sim 20\,nm$ for both polymers. Nanochannels etched in PET exhibited a pronounced surface roughness in contrast to smooth channels etched in PC. Nanowires grown in these PET membranes adopted the surface roughness, thus a new parameter, interesting for nanostructured thermoelectrics, was found for the fabrication of $Bi_{1-x}Sb_x$ nanowires.

For the deposition of Bi, Sb, and $Bi_{1-x}Sb_x$ alloy nanowires, miscible electrolytes based on hydrochloric acid and Bi(III)- and Sb(III)-chloride, respectively, were developed. Varying electrolyte concentrations and deposition potentials at room temperature, alloy nanowires with compositions of $0 < x < 0.5$ were prepared. These nanowires were characterized by X-ray diffraction (XRD) to examine the preferred crystallographic orientation and the composition of the wires. As complementary method to analyze the composition, energy dispersive X-ray spectroscopy (EDX) in scanning and transmission electron microscopes (SEM and TEM) was employed. Further information about the structure and morphology was obtained from bright and dark field imaging (BF and DF), high resolution TEM (HR-TEM), and scanning transmission electron microscopy in an SEM (STEM-in-SEM).

A setup for the measurement of the Seebeck coefficient of nanowire arrays at cryogenic temperatures from room temperature down to temperatures of the order of $30\,K$ was built up. The Seebeck voltage was measured with a nanovoltmeter while the temperature difference over the sample was varied around a given setpoint. Additionally, $I - U$ curves were obtained with a sourcemeter in order to measure the resistance of the sample.

This work is divided into five parts: an introduction into the field, the fabrication of the nanowire arrays from irradiation of polymer foils to electrodeposition, the characterization of these nanowires (as arrays or individually) by various methods, the measurement of transport properties, and a summary and outlook. At the beginning of some sections a table of symbols is given for better orientation since some symbols have a different meaning according to the context.

1.2 Thermoelectrics

symbol	quantity
$\vec{E}$	electrical field
I, R	current and resistance
$\vec{j}, \vec{q}$	electrical and thermal current density
$\kappa_{e,L}$	thermal conductivity of charge carriers and lattice
n	charge carrier density
Π, S, τ	Peltier, Seebeck, and Thomson coefficient
σ	electrical conductivity
ZT, η	figure of merit, efficiency
T	absolute temperature
x	Sb concentration

In Figure 1.1, simple thermoelectric modules for the application of thermoelectric effects are shown. The Seebeck effect can be applied to generate a voltage by a temperature difference (Figure 1.1(a)). Using the Peltier effect, heating and cooling is possible by applying a current (Figure 1.1(b)).

In general, the current density is given by

$$\vec{j} = \sigma(\vec{E} - S\nabla T), \tag{1.1}$$

where $\vec{E}$ denotes the electrical field and S the Seebeck coefficient. S is defined at $\vec{j} = 0$, hence $\vec{E} = S\nabla T$. Thus, a temperature gradient can be used to generate
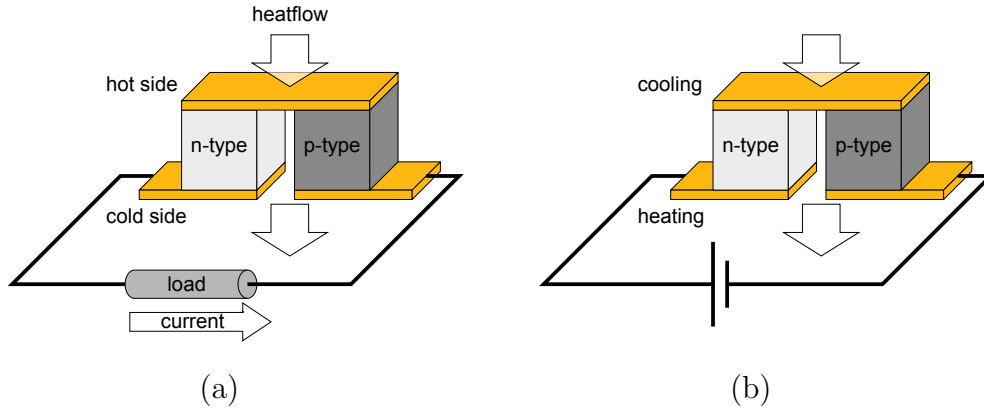

Figure 1.1: Peltier module consisting of an n-type and a p-type leg to show the basic principles. (a) Generation of power by temperature gradient and (b) heating and cooling by Peltier effect.

electrical power. The Peltier coefficient Π describes the effect that heat is transported differently by the charge carriers in different materials, and the thermal current density becomes

$$\vec{q} = \Pi\vec{j} - \kappa\nabla T. \tag{1.2}$$

In addition to Joule heating, the Thomson effect occurs if there is a temperature gradient along the sample. Thus, there is a heat absorption or emission proportional to current density and temperature gradient with a proportionality constant τ. The three coefficients are interconnected by the Kelvin relations:

$$\Pi = ST \text{ and } \tau = T\frac{\mathrm{d}S}{\mathrm{d}T}. \tag{1.3}$$

For an assessment of the thermoelectric efficiency of a material, a quantity called thermoelectric figure of merit $Z \cdot T$ is introduced. ZT is a function of the Seebeck coefficient S, the electrical and thermal conductivity σ and κ, respectively, and the absolute temperature T, and defined by

$$ZT = \frac{S^2\sigma}{\kappa}T, \tag{1.4}$$

where κ is the sum of contributions from the charge carriers κ_e and the lattice κ_L to the thermal conductivity.

For bulk material, these quantities are in general interconnected and a function of the charge carrier density n as indicated in Figure 1.2(a). κ_e and σ are connected by the Wiedemann-Franz law

$$\frac{\kappa_e}{\sigma} = \frac{1}{3}\left(\frac{\pi k_B}{e}\right)^2 T = LT, \tag{1.5}$$

with the theoretical Lorenz number $L = 2.44 \cdot 10^{-8}\,\mathrm{W\Omega K^{-2}}$. For nanomaterials, L can be different from the bulk counterpart, as shown by Völklein et al. for Pt nanowires.[72] However, κ_e still increases with increasing σ. κ_L is not a function of the charge carrier density, and therefore, it can be used to independently optimize ZT in nano-structured materials.[4] In general, S decreases for larger n. Thus, thermoelectric materials with highest ZT are expected in the range of semimetals and semiconductors, as can be seen in Figure 1.2(a).

The efficiency of a thermoelectric generator operating between the temperatures T_h and T_c was derived to be

$$\eta = \frac{RI^2}{(S_p - S_n)IT_h + \kappa(T_h - T_c) - \frac{1}{2}RI^2}, \tag{1.6}$$

where R denotes the resistance of the device and I the electrical current.[73] Then, the maximal thermoelectrical efficiency $(d\eta/dI = 0)$ is given by

$$\eta_{\text{max}} = \frac{T_h - T_c}{T_h} \frac{\sqrt{1 + ZT_m} - 1}{\sqrt{1 + ZT_m} + T_c/T_h} \xrightarrow{ZT_m \to \infty} \frac{T_h - T_c}{T_h} = \eta_c. \tag{1.7}$$

Here, the figure of merit ZT_m is taken at the mean temperature $T_m = \frac{1}{2}(T_h + T_c)$. The limit for $ZT_m \to \infty$ is given by a term similar to the Carnot efficiency η_c. For $ZT_m = 1$, which is about the maximum value for commercial generators at room temperature today, and $T_c = 300$ and $T_h = 400\,\text{K}$ the maximum theoretical efficiency is $4.8\,\%$, and if the generator is working between 300 and $320\,\text{K}$, it only amounts to $1.1\,\%$. Because of these low efficiencies, materials with larger ZT values are desirable.

Using a thermopile as a sensor, the maximum specific sensitivity was shown to be proportional to $\sqrt{ZT}$, and the response time is proportional to the square of the length of a leg.[74] Because of parasitic thermal conductance, it is also important to regard the medium surrounding the thermopile to optimize the sensitivity.[58]

Figure 1.2(b) shows common materials used in modules. At room temperature, Bi_2Te_3 has a large ZT and by doping it can be fabricated as n- and p-type material. At liquid nitrogen temperatures, $\text{Bi}_{1-x}\text{Sb}_x$ has maxima in ZT at Sb concentrations of $x = 0.08$ and 0.16.[75] Therefore, in this work $\text{Bi}_{1-x}\text{Sb}_x$ nanowires were prepared with emphasis on Bi-rich alloys.
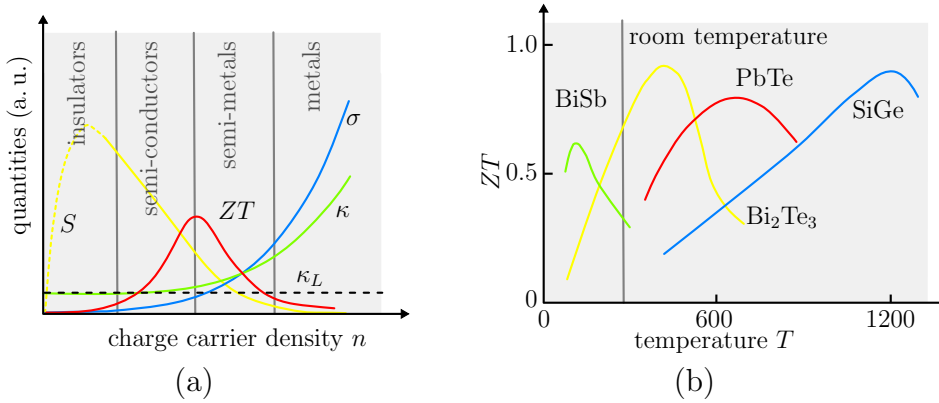

Figure 1.2: (a) Thermoelectrical properties as a function of charge carrier density according to Rowe.[73] (b) Figure of merit ZT for different bulk materials as function of T according to Sommerlatte et al.[76]

1.3 Properties of Bismuth and Bismuth-Antimony

symbol	quantity
a, c, u	lattice parameters and atom position in the unit cell
d	interplanar lattice spacing
hkl	Miller indices
θ	diffraction angle
x	Sb concentration

1.3.1 Crystalline Structure

Bismuth, antimony, and their alloys belong to the rhombohedral space group 166 (R$\bar{3}$m), which is sometimes also called A$_7$ structure. In this work, hexagonal indices are used for simplicity and all vectors refer to the hexagonal base. In Figure 1.3, the rhombohedral primitive unit cell, the a- and c-axis, and the two atoms of the base placed at $(0, 0, \pm u)$ are shown. The hexagonal unit cell contains six atoms at $(0, 0, \pm u)$, $(2/3, 1/3, 1/3 \pm u)$, and $(1/3, 2/3, 2/3 \pm u)$. u was measured with high accuracy by Cucka et al. up to $x = 0.3$ for a large temperature range, and amounts to about 0.234.[77] In Figure 1.3, also an orthogonal right-handed base of binary, bisectrix, and trigonal axes is indicated. Due to space group symmetry, tensors of rank 2 describing physical properties of the crystal have only two independent components, parallel and perpendicular to the trigonal axis.[78]
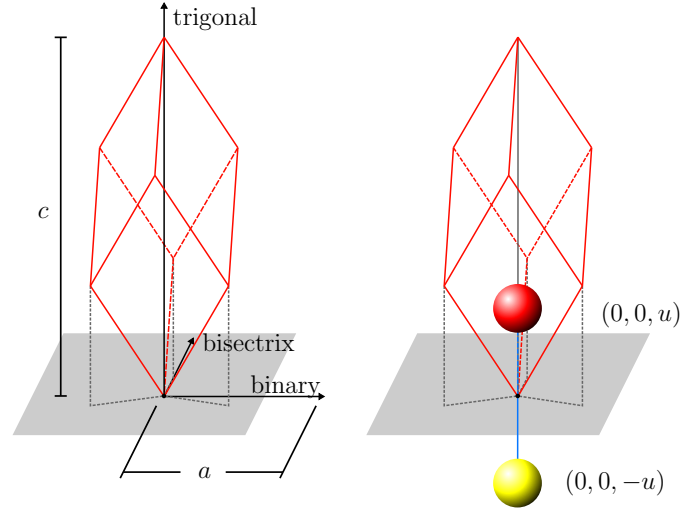

Figure 1.3: Primitive rhombohedral unit cell and the atoms of the base.

	Bi	$Bi_{0.5}Sb_{0.5}$	Sb
d_{110} (nm)	0.227	0.221	0.215
d_{012} (nm)	0.328	0.320	0.311
d_{003} (nm)	0.395	0.387	0.376

Table 1.1: *d*-spacings for Bi, $Bi_{0.5}Sb_{0.5}$, and Sb calculated from the unit cell data in Dismukes et al.[79]

The lattice parameters of $Bi_{1-x}Sb_x$ alloys almost follow Vegard's law from $a = 4.5465\,\text{Å}$ and $c = 11.8616\,\text{Å}$ for pure Bi to $a = 4.3085\,\text{Å}$ and $c = 11.2732\,\text{Å}$ for pure Sb at room temperature.[79] This is in excellent agreement with Cucka et al.,[77] where also values for $T = 78\,\text{K}$ are provided: $a = (4.534 - 21.92 \cdot 10^{-4}\,x)\,\text{Å}$ and $c = (11.814 - 48.57 \cdot 10^{-4}\,x)\,\text{Å}$ for $x \leq 0.3$.

If the hexagonal description is used, the *d*-spacings between lattice planes (hkl) are given by

$$\frac{1}{d_{hkl}^2} = \frac{4}{3}\,\frac{h^2 + hk + k^2}{a^2} + \frac{l^2}{c^2}. \tag{1.8}$$

In HR-TEM the lattice planes (012), (110), and (003) are mostly observed due to their large reflecting power. The corresponding *d*-spacings are given in Table 1.1, for Bi, Sb, and $Bi_{0.5}Sb_{0.5}$. In Table 1.2, intensities in powder diffraction and *d*-spacings of a Bi standard powder are presented. Furthermore, diffraction angles are calculated for Bi, Sb, and $Bi_{0.5}Sb_{0.5}$ for Cu-K$_\alpha$ radiation. The difference in 2θ between Bi and Sb is already 1.5° for {012} reflections. In addition, the minimal angles of the $\{hkl\}$ planes to the *c*-axis are also listed for Bi. The angle to the trigonal axis is of interest for thermoelectrical properties.

1.3.2 Band Structure

symbol	quantity
d	nanowire diameter
D	density of states
E_{g}, E_Δ	characteristic band structure parameters for Bi
$E_{L,T}$	dispersion relations at L- and T-point
$\vec{k}$	wave vector
m^*	effective mass
$\mu_{e,h}$	mobilities of electrons and holes
ρ	resistivity

{hkl}	d_{hkl} (Å)	I_0	2θ (°)			min($\angle$({hkl}, [001])) (°)
			Bi	Bi$_{0.5}$Sb$_{0.5}$	Sb	
{012}	3.2800	100	27.16	27.88	28.67	56.4
{110}	2.2730	29	39.61	40.76	41.90	90.0
{113}	1.9711	6	46.02	47.30	48.68	45.1
{202}	1.8686	13	48.69	50.10	51.56	71.6
{024}	1.6505	7	56.02	57.61	59.36	56.4
{122}	1.4436	10	64.50	66.49	68.53	69.0
{214}	1.3303	5	70.78	72.95	75.29	52.5

Table 1.2: *d*-spacings and intensities I_0 of reflections of equivalent lattice planes {hkl} in a powder diffraction pattern of pure Bi normalized to 100 (selection from JCPDS-44-1246 PDF-2 Sets 1-89 of those observed in the experimental part). Furthermore, the 2θ values expected for XRD were calculated for Cu-K$_{\alpha 1}$ radiation.

For a theoretical description of the transport properties of Bi$_{1-x}$Sb$_x$, three points of the Brillouin zone are of special interest, namely the T, H, and L points. For pure bismuth, the dispersion relation is parabolic for holes, and it is strongly non-parabolic for electrons due to strong coupling between the L-point electrons. The two dispersion relations $E_{\mathrm{T}}(\vec{k})$ for holes and $E_{\mathrm{L}}(\vec{k})$ for electrons are given by the Lax two-band model:[80]

$$E_{\mathrm{T}}(\vec{k}) = \frac{\hbar^2 k_x^2}{2m_x} + \frac{\hbar^2 k_y^2}{2m_y} + \frac{\hbar^2 k_z^2}{2m_z} \tag{1.9}$$

$$E_{\mathrm{L}}(\vec{k}) = \frac{E_{\mathrm{gap}}}{2} \left[\sqrt{1 + \frac{2\hbar^2}{E_{\mathrm{g}}} \left(\frac{k_x^2}{m_x} + \frac{k_y^2}{m_y} + \frac{k_z^2}{m_z} \right)} - 1 \right]. \tag{1.10}$$

The band overlap E_Δ and the direct band gap E_{g} at the L-point are expressed according to the empirical formulae

$$\begin{aligned} E_\Delta(T) &= [38 + 4.4 \cdot 10^{-2} \cdot (T - 80) - 4.58 \cdot 10^{-4} \cdot (T - 80)^2 \\ &\quad + 7.39 \cdot 10^{-6} \cdot (T - 80)^3] \text{ meV} \end{aligned} \tag{1.11}$$

$$E_{\mathrm{gap}}(T) = (13.6 + 2.1 \cdot 10^{-3} \cdot T + 2.5 \cdot 10^{-4} \cdot T^2) \text{ meV} \tag{1.12}$$

taken from Lin et al.[81] The former equation applies for temperatures above 80 K. Below 80 K, E_Δ is assumed to be 38 meV.

Furthermore, an important property of the band structure is the mobility of charge carriers. In bulk bismuth, the mobilities are also given by empirical formulas according to Sun:[82]

$$
\mu_e(T) = \begin{pmatrix} 1.05 \cdot 10^6 \cdot T^{-2.22} & 0 & 0 \\ 0 & 6.91 \cdot 10^4 \cdot T^{-2.46} & -1.09 \cdot 10^5 \cdot T^{-2.33} \\ 0 & -1.09 \cdot 10^5 \cdot T^{-2.33} & 1.74 \cdot 10^6 \cdot T^{-2.47} \end{pmatrix},
$$

$$
\mu_h(T) = \begin{pmatrix} 2.27 \cdot 10^5 \cdot T^{-2.27} & 0 & 0 \\ 0 & 2.27 \cdot 10^5 \cdot T^{-2.27} & 0 \\ 0 & 0 & 3.10 \cdot 10^2 \cdot T^{-1.15} \end{pmatrix}
$$

in $m^2V^{-1}s^{-1}$. Here, T is the value of the absolute temperature. For $Bi_{1-x}Sb_x$, a schematic of the changes of the band structure due to alloying is given in Figure 1.4. In pure Bi, the holes are located at the T point and the electrons at the L point. However, the band overlap decreases when alloying with Sb until the alloy becomes a semiconductor at $x = 0.07$. Simultaneously, the band edge of the H point increases, so at $x = 0.22$ the alloy will be a semimetal again.
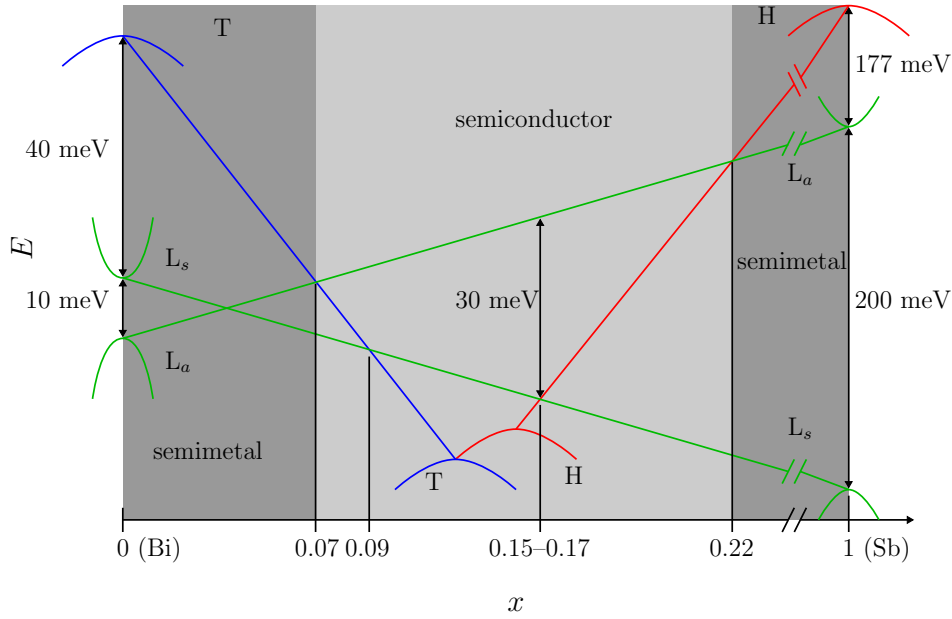

Figure 1.4: Band structure of $Bi_{1-x}Sb_x$ at $0\,K$ as a function of x according to Lenoir et al. (energies not to scale).[26]
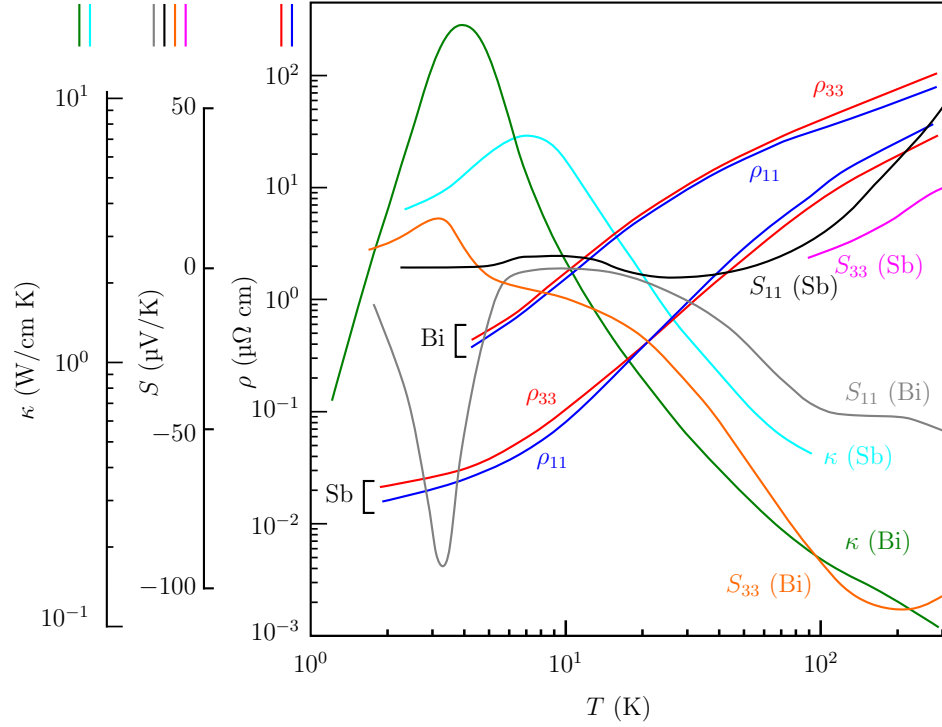
17

Figure 1.5: Overview over thermoelectric properties, $\rho = \sigma^{-1}$, S, and κ, of bulk Bi and Sb as functions of temperature and orientation. Data taken from the review paper by Issi.[83]

1.3.3 Transport Properties of Bismuth and Antimony

In Figure 1.5, thermoelectric properties of bulk Bi and Sb are summarized for the temperature regime relevant for this work. The data for $\rho = \sigma^{-1}$, S, and κ were collected from the review paper about group V semimetals by Issi.[83] For S and ρ, it is distinguished between values with respect to the a- and c-axis (indices $ij = 11$ and 33, respectively).

As we have seen from Figure 1.2(b), the maximum ZT value for bulk $Bi_{1-x}Sb_x$ is at low temperatures. At 70 K, there are two maxima in the ZT, namely 0.4 and 0.5 for $x = 0.08$ and $x = 0.16$.[75]

1.4 Size Effects

symbol	quantity
E, E_F	energy, Fermi energy
f	Fermi-Dirac distribution
l_e	electron mean free path
K_i, L_i	special functions to represent the transport properties
q	electrical charge
τ	average scattering time

1.4.1 Finite-Size Effects

The electrical conductivity of nanowires can be decreased by additional scattering of charge carriers at grain boundaries and surface. Two models describe these effects, namely the model of Dingle for scattering at the surface,[84] and the model of Mayadas and Shatzkes for scattering at grain boundaries.[85]

In 1937, Fuchs calculated the influence of additional scattering of charge carriers at the surface of thin films.[86] Twenty-two years later, Dingle applied the theoretical considerations to thin wires with a circular cross-section and a spherical Fermi surface.[84] He concluded that the effect of the scattering events on σ is a function of two parameters, the specularity p, with $0 \leq p \leq 1$, and the ratio of the wire diameter d and the electron mean free path l_e.

For $p = 1$, all scattering processes at the surface are specular, i. e. totally elastic. This implies that the scattering process does not influence the conductivity. For $p < 1$, the electrons are scattered inelastically with a probability of $(1 - p)$. This leads to a decrease of the conductivity. For $p = 0$, when all electrons are scattered diffusely, the conductivity reaches its lower bound.

The model of Mayadas and Shatzkes describes the scattering of charge carriers at grain boundaries introduced as potential barriers. A simple approximation to this problem is the assumption of a potential barrier V_0 at the positions x_i where the grain boundaries are located. Thus, the total potential is given by

$$V(x) = V_0 \sum_i \delta(x - x_i),$$

where δ denotes the Dirac distribution. Then, the influence of grain boundary scattering on the conductivity is a function of three parameters, namely the mean grain size D_{grain}, the mean free path of the electrons l_e, and the probability p_{grain} of an electron being scattered at a grain boundary. The correction factor then turns out to be

$$\frac{\sigma}{\sigma_0} = 1 - \frac{3}{2}\alpha + 3\alpha^2 - 3\alpha^3 \ln\left(1 + \frac{1}{\alpha}\right), \tag{1.13}$$

with the value for bulk σ_0 and

$$\alpha = \frac{l_e}{D_{\mathrm{grain}}} \frac{p_{\mathrm{grain}}}{1 - p_{\mathrm{grain}}}. \tag{1.14}$$

Here, the ratio σ/σ_0 is a monotonically decreasing function of the parameter α (for $\alpha \lesssim 1000$). For the limit $\alpha \to 0$, σ/σ_0 converges to 1, whereas for large α the ratio σ/σ_0 approaches 0. This behavior is comprehensible, if one takes a closer look at equation 1.14. At fixed p_{grain}, α is larger for smaller grain sizes D_{grain}, i.e. the electrons encounter more boundaries and the conductivity is more reduced. On the other hand, an increase of p_{grain} also leads to an increase of α because the electrons are scattered with a higher probability.

1.4.2 Quantum-Size Effects

When the size of the nanowires is comparable to the Fermi wavelength, quantum-size effects are expected. Hicks and Dresselhaus proposed a semi-classical approach using the Boltzmann transport equation

$$\frac{\partial f}{\partial t} + \vec{v} \cdot \nabla_{\vec{r}} f + \frac{q}{\hbar} \vec{E} \cdot \nabla_{\vec{k}} f = \left. \frac{\partial f}{\partial t} \right|_{\mathrm{collision}}, \tag{1.15}$$

with the velocity $\vec{v}$, the Fermi-Dirac distribution

$$f_0(\vec{k}) = \frac{1}{\exp(\frac{E(\vec{k})-E_F}{k_B T}) + 1}, \tag{1.16}$$

and quantized energy levels for the charge carriers.[4,6] The properties σ, S, and κ derived by regarding two bands can be represented by a set of functions K_i, which can be defined as follows:[2]

$$K_i = -\frac{2T}{Nm^*} \int_0^\infty E^{i+1} D(E) \tau(E) \frac{\partial f_0(E)}{\partial E} \mathrm{d}E, \tag{1.17}$$

being N the dimensionality of the system, D the density of states, and τ the average scattering time. With these K_i, σ, S, and κ_e can be written as

$$\sigma = \frac{q^2}{T} K_0, \tag{1.18}$$

$$S = -\frac{1}{qT} \left(E_F - \frac{K_1}{K_0} \right), \text{ and} \tag{1.19}$$

$$\kappa_e = \frac{1}{T^2} \left(K_2 - \frac{K_1^2}{K_0} \right). \tag{1.20}$$

The density of states $D(E)$ appearing in Equation 1.17 is defined by

$$D(E) = \frac{1}{V} \frac{\mathrm{d}N}{\mathrm{d}E},$$ (1.21)

where N and V denote the number of states and the volume, respectively. For bulk Bi, $D(E)$ can be derived as[87]

$$D_{\mathrm{T}}(E) = \frac{\sqrt{2}}{\pi^2 \hbar^3} \sqrt{m^*_{x,T} m^*_{y,T} m^*_{z,T}} \sqrt{E}$$ (1.22)

$$D_{\mathrm{L}}(E) = \sum_{\text{L-points}} \frac{\sqrt{2}}{\pi^2 \hbar^3} \sqrt{m^*_{x,L} m^*_{y,L} m^*_{z,L}} \sqrt{\frac{E^2}{E_g} + E} \left(\frac{2E}{E_g} + 1 \right).$$ (1.23)

However, for a nanowire with sufficiently small diameter d, the charge carriers are confined in two dimensions, having discrete energy levels E_{ij} in these directions according to quantum mechanics. Thus, $D(E)$ will have a different form:[81]

$$D(E) = \frac{\sqrt{2m^*}}{\pi \hbar d^2} \frac{1}{\sqrt{E - E_{ij}}}.$$ (1.24)

If we consider a nanowire with wire axis along the z-axis and a square cross-section, the charge carriers are confined normal to the wire direction in a two-dimensional square box with an edge length d. At the T-point, these levels are given by the eigenvalues

$$E_{ij} = \frac{1}{2} \left(\frac{\pi \hbar}{d} \right)^2 \left(\frac{i^2}{m^*_x} + \frac{j^2}{m^*_y} \right),$$ (1.25)

with natural numbers i and j. Due to the low effective masses of bismuth, appearing here in the denominator, quantum size effects are more pronounced. At the L-point, these levels have a different form due to the dispersion relation in Equation 1.10:

$$E^{\mathrm{L}}_{ij} = \frac{E_{\text{gap}}}{2} \left(\sqrt{1 + \frac{4E_{ij}}{E_{\text{gap}}}} - 1 \right).$$ (1.26)

The comparison of both cases, bulk material and quantum wire, is illustrated in Figure 1.6. For the quantum wire, the bands split up into subbands. The L and T point bands overlap for bulk material, but for nanowires with small diameters there is a gap. The critical diameter for the semimetal to semiconductor transition is a function of the temperature, the diameter, and, in $\mathrm{Bi}_{1-x}\mathrm{Sb}_x$ alloys, the concentration of Sb.[23]

With these quantized energy levels, we also obtain individual properties σ_{ij}, S_{ij}, and κ_{ij}. In general, the current densities for each subband ij are

$$\vec{j}_{ij} \;=\; \sigma_{ij}(\vec{E} - S_{ij}\nabla_{\vec{r}}T) \tag{1.27}$$

$$\vec{j}_{Q,ij} \;=\; S_{ij}T\vec{j}_{ij} - \kappa_{ij}\nabla_{\vec{r}}T, \tag{1.28}$$

taking into account the contributions from the Seebeck effect and the Peltier effect, respectively. Then, with $\vec{j} = \sum \vec{j}_{ij}$ and $\vec{j}_Q = \sum \vec{j}_{Q,ij}$, the calculations can be generalized to multiple subbands leading to

$$\sigma \;=\; \sum_{ij} \sigma_{ij} \tag{1.29}$$

$$S \;=\; \left(\sum_{ij} S_{ij}\sigma_{ij} \right) \sigma^{-1} \tag{1.30}$$

$$\kappa \;=\; \sum_{ij} \kappa_{ij} + T \left[\sum_{ij} S_{ij}^2 \sigma_{ij} - \left(\sum_{ij} S_{ij}\sigma_{ij} \right)^2 \sigma^{-1} \right]. \tag{1.31}$$

Obviously, the total Seebeck coefficient is the sum of the individual coefficients weighted by their individual conductivities, and the total thermal conductivity becomes a function of the individual conductivities and Seebeck coefficients. With equations 1.18, 1.19, and 1.20, one obtains
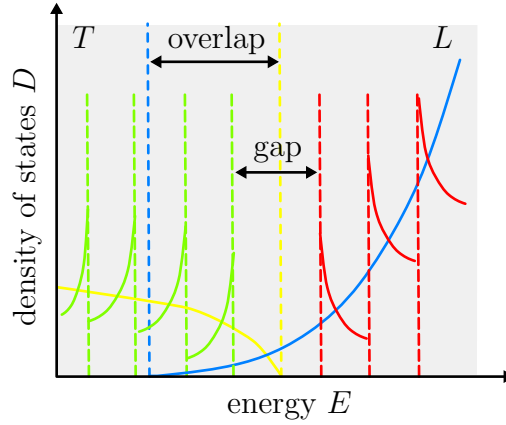
Figure 1.6: Schematic of the density of states for thin Bi nanowires (green and red) compared to bulk (yellow and blue). The corresponding band edges are indicated by dashed lines. For sufficiently small diameters, the band overlap is turned into a band gap.

$$\sigma \;=\; \frac{q^2}{T}\sum_{ij} K_{0,ij} \tag{1.32}$$

$$S \;=\; -\frac{1}{qT}\left[E_F - \left(\sum_{ij} K_{1,ij}\right)\cdot\left(\sum_{ij} K_{0,ij}\right)^{-1}\right] \tag{1.33}$$

$$\kappa \;=\; \frac{1}{T^2}\left[\sum_{ij}(K_{2,ij} - 2E_F K_{1,ij} + E_F^2 K_{0,ij})\right.$$
$$\left.- \left(\sum_{ij}(K_{1,ij} - E_F K_{0,ij})\right)^{2}\cdot\left(\sum_{ij} K_{0,ij}\right)^{-1}\right]. \tag{1.34}$$

Lin et al. introduced functions L_i which are linear combinations of the functions K_i according to[81]

$$L_{0,ij} \;=\; \frac{q^2}{T}K_{0,ij} \tag{1.35}$$

$$L_{1,ij} \;=\; \frac{q^2}{T}(K_{1,ij} - E_F K_{0,ij}) \tag{1.36}$$

$$L_{2,ij} \;=\; \frac{q^2}{T}(K_{2,ij} - 2E_F K_{1,ij} + E_F^2 K_{0,ij}). \tag{1.37}$$

These L_i have the convenient property of being additive, so the transport properties simply become

$$\sigma \;=\; \sum_{ij} L_{0,ij} \tag{1.38}$$

$$S \;=\; \frac{1}{qT}\left(\sum_{ij} L_{1,ij}\right)\cdot\left(\sum_{ij} L_{0,ij}\right)^{-1} \tag{1.39}$$

$$\kappa \;=\; \frac{1}{q^2 T}\left[\sum_{ij} L_{2,ij} - \left(\sum_{ij} L_{1,ij}\right)^{2}\cdot\left(\sum_{ij} L_{0,ij}\right)^{-1}\right]. \tag{1.40}$$

Theoretical calculations made so far with these equations assumed that effective masses for quantum wires are the same as for bulk material and considered only one subband.[23,81] Since there are more and more sub-bands contributing to the transport quantities for increasing wire diameter, numerical calculations demand also more and more processing power. Recently, Cornett and Rabin made calculations regarding 300 subbands.[24] However, there is still need for systematic comparison of this model with experimental data.

2 Synthesis of Bi$_{1-x}$Sb$_x$ Nanowires

symbol	quantity
e	elementary charge
E	ion energy in irradiation processes
I	averaged ionization energy of the target atoms
m_e	free electron mass
R_p	projected range
x	path of ion in matter
Z_eff	effective charge of the ions
Z_target	nuclear charge of the target atoms

2.1 Etched Ion-Track Membranes as Templates

In many works reporting about the template-based electrodeposition of nanowires, anodized alumina oxide (AAO) was used as template. In this work, nanowires were deposited in polymeric etched ion-track templates fabricated by irradiation with swift heavy ions and wet-chemical etching. The use of polymer templates offers several important advantages. First, the thermal conductivity is much lower than in AAO, which is important for thermoelectric applications. Second, the polymer can be easily dissolved with organic solvents without affecting the nanowire surface. By combining ion irradiation and etching, diameter and channel density were adjusted independently.

Table 2.1 displays some important properties of the two polymers, polycarbonate (PC) and poly(ethylene terephthalate) (PET), employed in this work. In Figure 2.1, their chemical structures are also shown. Their low thermal conductivities, 0.19 and 0.13 W m^{-1} K^{-1}, respectively, are suitable for the thermoelectric characterization of embedded nanowire arrays.

For some measurements, the membrane has to be dissolved to deliberate the nanowires which can be achieved by using the solvents listed in Table 2.1. To avoid oxidation, the nanowires were kept inside the templates as long as possible before characterization.

property	PC[88]	PET[89]
full name	polycarbonate	poly(ethylene terephthalate)
trade name	Makrofol N/KG (yellow dye)	Hostaphan RN12/RN36
fabrication	normal cast film	biaxially oriented
company	Bayer (Mobay)	Hoechst (Mitsubishi)
thickness (µm)	30, 60	12, 36
κ ($\mathrm{W\,m^{-1}\,K^{-1}}$)	~ 0.19	~ 0.13
melting temp. (°C)	230	260
density ($\mathrm{g\,cm^{-3}}$)	1.2	1.4
solvents	dichloromethane	(9:1 v/v) chloroform
	N,N-dimethylformamide	+ hexafluoro-2-propanol
sum formula	$(C_{16}H_{14}O_3)_n$	$(C_{10}H_8O_4)_n$

Table 2.1: Summary of some properties of PC and PET according to manufacturers.
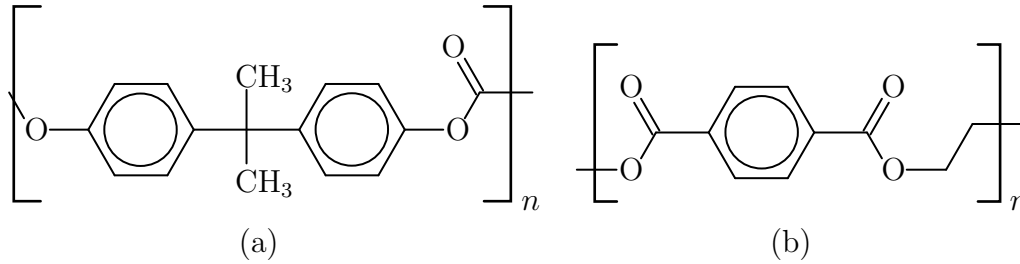
Figure 2.1: Chemical structures of employed polymers: (a) polycarbonate and (b) poly(ethylene terephthalate).

2.1.1 Irradiation of Polymers with Swift Heavy Ions

As mentioned above, etched ion-track track templates are fabricated in two steps: irradiation with swift heavy ions and chemical etching. The polymer foils used for the experiments were irradiated at the UNILAC linear accelerator facility at the GSI Helmholtz Centre for Heavy Ion Research in Darmstadt. For the creation of tracks in PC and PET, gold and uranium ions with a specific energy of 11.1 MeV/u were employed, the total ion energies being 2.2 and 2.6 GeV, respectively. Along their trajectories through the polymer, the ions lose energy. It is distinguished between nuclear energy loss $dE/dx|_n$ due to interaction with the atomic core and electronic energy loss $dE/dx|_e$ due to interaction with the electrons in the target material. Then, the total energy loss is given by $dE/dx = dE/dx|_e + dE/dx|_n$. The electronic energy loss is described by the Bethe-Bloch formula[90]

$$-\frac{dE}{dx}\bigg|_e = 4\pi N_A m_e c^2 r_e^2 \frac{Z_{\text{target}}}{A} \frac{Z_{\text{eff}}^2}{\beta^2} \left[\frac{1}{2} \ln\left(\frac{2m_e c^2 \beta^2 \gamma^2 T_{\max}}{I^2}\right) - \beta^2 - \frac{\delta(\beta\gamma)}{2}\right], \quad (2.1)$$

being β the velocity of ions relative to the speed of light c, δ and U correction terms, E the ion energy in the irradiation process, I the averaged ionization energy of the target atoms, Z_{target} the nuclear charge of the target atoms, $T_{\max}$ the maximum energy transferred to an atom, and Z_{target} the effective charge of the ions.

The Barkas formula gives the effective charge of the ion

$$Z_{\text{eff}} = Z\left[1 - \exp\left(-\frac{125\beta}{Z^{2/3}}\right)\right], \quad (2.2)$$

being Z the atomic number of the ion. Z_{eff} has to be introduced due to the fact that ions passing through matter permanently lose and catch electrons until an equilibrium is reached.[91]

When all energy is transferred to the target, the ion is stopped. The mean value of the depth, in which this occurs is called the projected range, which is given by

$$R_p = \int_{E_0}^{0} \left(\frac{dE}{dx}\right)^{-1} dE. \quad (2.3)$$

In order to produce uniform tracks in the polymer foils, it is necessary to select heavy ions[92] (e.g. Au or U ions) and a foil thickness that is smaller than R_p. These quantities can be estimated using the SRIM program.[93] Figure 2.2 shows energy loss and projected range of Au and U ions in both polymers, PC and PET. In Figure 2.2(b), the total initial energy is marked by dashed gray lines. The final energy after passing 90 μm polymer is marked by vertical colored dashed lines.

There are two models describing how tracks in solids are created by swift heavy ions:
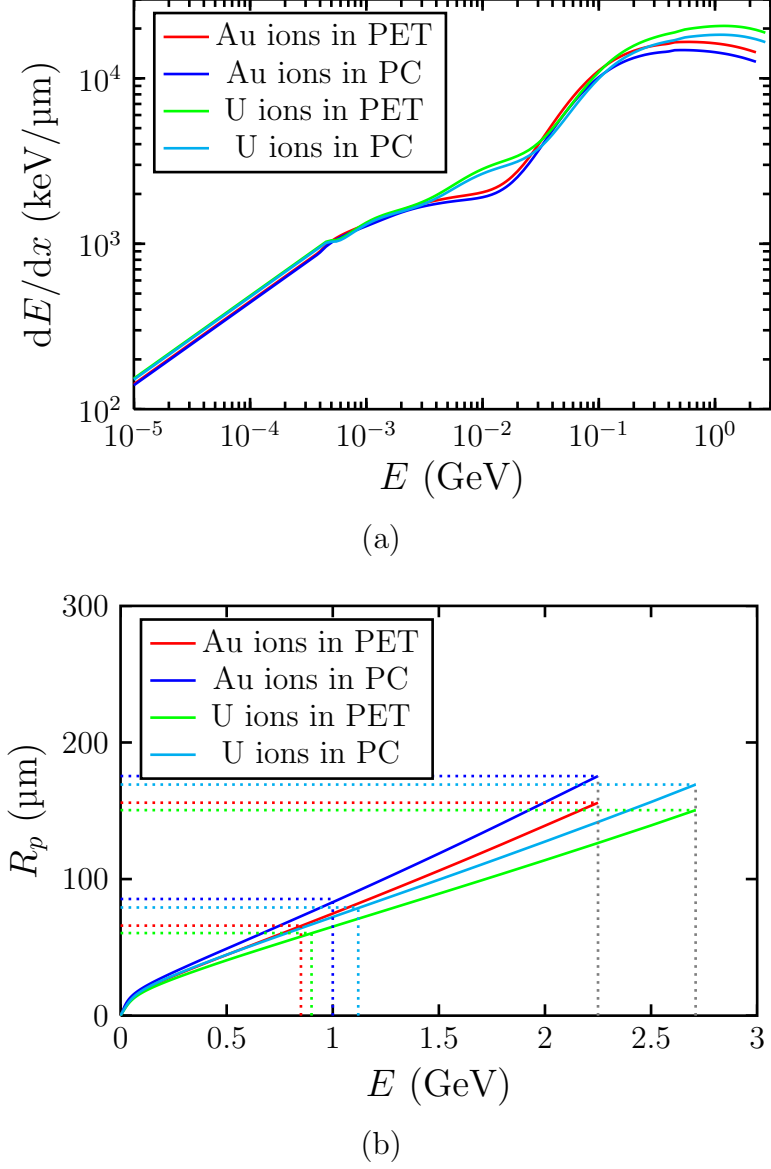
(a)

(b)

Figure 2.2: SRIM[93] calculations providing the total energy loss (a) and the projected range (b) as functions of the total energy for Au and U ions with an initial energy of $11.1\,\mathrm{MeV/u}$ passing PC and PET.

1. The Coulomb explosion model assumes, that the atoms along the trajectory are ionized and the repulsion of these ions leads to the formation of a track.[94]

2. The thermal spike model assumes that the energy deposited leads to a strongly elevated temperature along the trajectory of a swift heavy ion.[95]

2.1.2 Chemical Etching

symbol	quantity
α	opening angle of the nanochannel
c	concentration of ions in the electrolyte
D	diffusion coefficient
F	Faraday constant
μ	mobility of ions
I, j	current and current density during deposition
L	length of nanochannel
U	potentials in electrochemistry
t	time
$v_\mathrm{t}, v_\mathrm{b}$	etching velocity of the track and bulk material
ϕ	number of channels per unit area / electrical potential
z	electrical charge

The ion-tracks created during irradiation can be selectively etched and enlarged to nanochannels by introducing the foil into an adequate etching solution. In order to achieve nearly cylindrical channels, the etching rate along the latent track has to be much larger than the etching rate in undamaged bulk material. As can be derived from Figure 2.3, for small opening angle α, the ratio given by the relationship[96]

$$\sin \alpha \approx \frac{v_\mathrm{b}}{v_\mathrm{t}}. \tag{2.4}$$

In practice, an aspect ratio of the order of 10^3 can be obtained in PC and PET. An appropriate etchant for PC and PET is a solution of concentrated sodium hydroxide.[97] In this work, tracks in PC and PET templates were etched at $50\,°\mathrm{C}$ in 6 and $2\,\mathrm{mol/l}$ NaOH, respectively. The etching rates were determined from the resulting wire diameters for different etching times. One obtains $\sim 20\,\mathrm{nm/min}$ for PC and $\sim 5\,\mathrm{nm/min}$ for PET.

For a given etching time, the diameter values display some scattering around an average. For thick nanowires and sub-µm wires, Ensinger and Vater report errors of $10\,\%$ for $80 < d < 100\,\mathrm{nm}$ and $\sim 5\,\%$ for $d > 100\,\mathrm{nm}$.[98] In this work, it has been observed that the error increases further for smaller diameters, resulting in
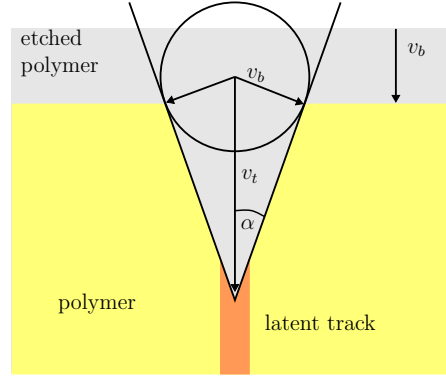
Figure 2.3: Schematic of the ion-track etching process.

about 10 % for thicker nanowires ($d \approx 100\,\mathrm{nm}$) and 20 % for thinner nanowires ($d \approx 25\,\mathrm{nm}$), which can be attributed to irregular break-through times during the etching process.

Before etching, the samples are irradiated with UV light for one hour on each side to improve the etching homogeneity and selectivity.[97,99]

2.2 Electrochemical Deposition of Bi$_{1-x}$Sb$_x$

2.2.1 Experimental Setup

Prior to deposition, a gold layer was sputtered onto one side of the etched ion-track membrane. Then, the sample was placed between two Teflon compartments as schematically depicted in Figure 2.4(a). In the compartment on the right-hand side, the sputtered gold layer was reinforced by electrochemically deposited gold serving as cathode.

For this work, the former two-electrode setup employed for the deposition of pure Bi nanowires was extended to a three-electrode setup by the integration of a self-designed potentiostat and a reference electrode in order to control the deposition potential in a reproducible manner. As reference electrode, a saturated calomel electrode (SCE) by Meinsberg was employed. This electrode is based on the reaction of mercury to calomel and vice versa, $\mathrm{Hg_2Cl_2(s) + 2\,e^- \rightleftharpoons 2\,Hg(l) + 2\,Cl^-}$, and has a standard potential $U_{\mathrm{ref}}^{\ominus}$ in V versus the standard hydrogen electrode (SHE) of

$$U_{\mathrm{ref}}^{\ominus} = 0.2412 - 6.61 \cdot 10^{-4}(T-25) - 1.75 \cdot 10^{-6}(T-25)^2 - 9.0 \cdot 10^{-10}(T-25)^3$$

with the temperature T in °C.[100] A Pt$_{90}$Ir$_{10}$ spiral served as counter electrode. These three electrodes were arranged in the setup as depicted in Figure 2.4(a) and connected to a potentiostat. The potentiostat controlled the voltage at the reference electrode U_{ref} to the desired voltage U by comparison of U_{ref} with $-U$ over a voltage divider, and then provided a voltage to the counter electrode (CE) in order to keep $U_{\mathrm{ref}} = U$. In Figure 2.4(b), the circuit of the potentiostat is depicted. For the impedance converters and the closed loop control, a high-precision operational amplifier OPA404P with a high input impedance and a high slew rate, both necessary for electrochemical purposes, was selected. $-U$ was provided by a PCI-6229 DAQ card by National Instruments which also acquired the output voltage U_{out}. Finally, the deposition current was measured with a Keithley 6485 Picoammeter by measuring the current from working electrode to ground.

2.2.2 Choice of Electrolytes and Deposition Potentials

For the deposition of bismuth-antimony alloys according to the equation

$$(1-x)\,\mathrm{Bi^{3+}} + x\,\mathrm{Sb^{3+}} + 3\,e^- \rightleftharpoons \mathrm{Bi_{1-x}Sb_x}, \tag{2.5}$$
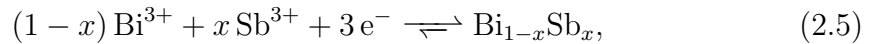
an electrolyte was developed that differed in two aspects from the one previously used for the deposition of pure bismuth nanowires.[35,101] It also based on hydrochloric acid, however, to completely dissolve the Sb(III)-chloride and, furthermore, to
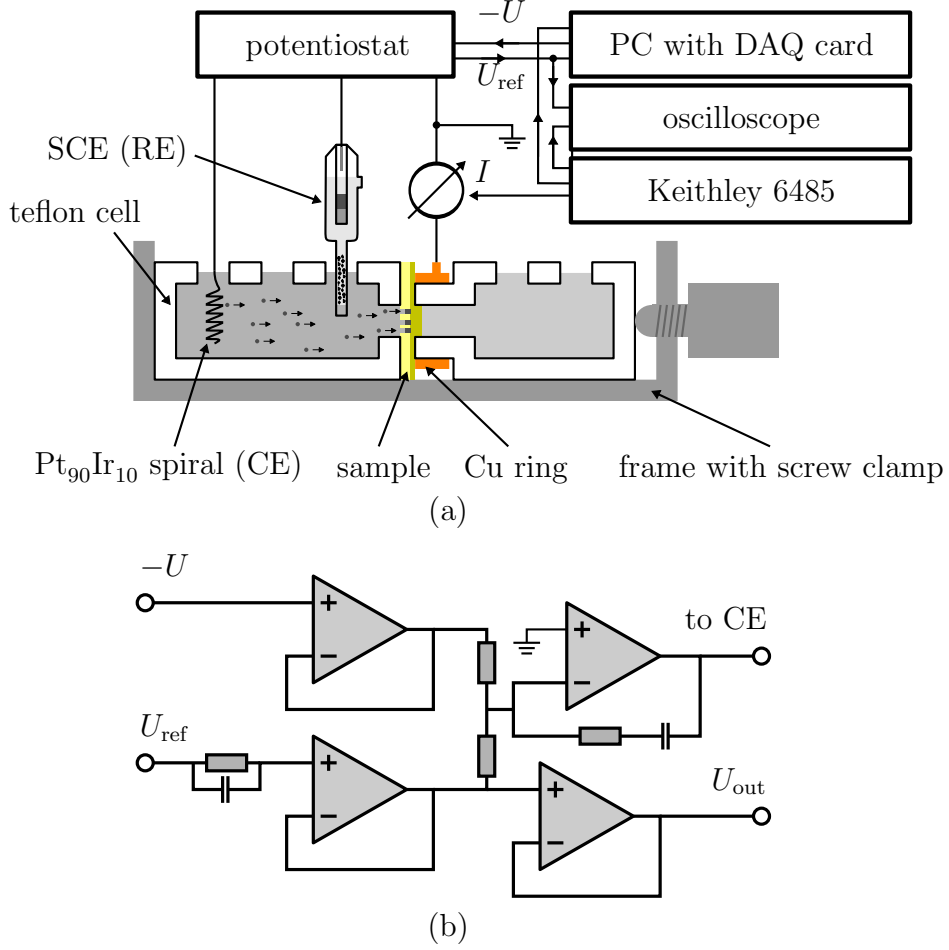
Figure 2.4: Schematic of the setup for electrochemical depositions. (a) Electrochemical cell and connections to devices and (b) potentiostat circuit.

chemical	purity grade	quantity (mol/l)	vendor
hydrochloric acid (37%)	pro analysi (p. a.)	1.95	Merck KGaA
glycerol	$\geq$ 99.5%, p. a.	1.09	Merck KGaA
NaCl	$\geq$ 99.5%, p. a.	0.2	LS Laborservice
tartaric acid	$\geq$ 99.5%, p. a.	0.3	Merck KGaA
Bi(III)-chloride	$\geq$ 98%	$0.1 \cdot (1 - r)$	Merck KGaA
Sb(III)-chloride	$\geq$ 99%, p. a.	$0.1 \cdot r$	Merck KGaA

Table 2.2: Electrolyte composition for the deposition of Bi$_{1-x}$Sb$_x$ nanowires, being r the fraction of Sb ions in the solution.

avoid reactions towards oxyanions, [28] the content of chlorides was reduced whereas the amount of acid was increased to lower the pH value. As previously, the electrolyte contained glycerol to increase the viscosity and NaCl as conducting salt. The components are listed in Table 2.2. Electrolytes with Bi(III)-chloride and Sb(III)-chloride were prepared separately and mixed according to the desired Sb concentration, the overall concentration being $c(\text{Bi}) + c(\text{Sb}) = 0.1 \,\text{mol/l}$.

Equation 2.5 is a simplification of the chemical processes occurring at the cathode. Vereecken et al. investigated in detail the standard potentials $U_0^{\ominus}$ for each reduction step (Me = Bi, Sb)

$$\text{MeCl}_n^{3-n} + 3 \, e^- \longrightarrow \text{Me} + n\text{Cl}^- \text{ with } 0 \leq n \leq 6 \qquad (2.6)$$
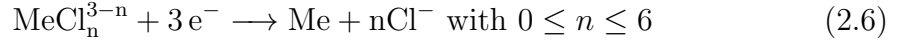
involved in the electrodeposition of Bi$_{1-x}$Sb$_x$ and found that $U_0^{\ominus}$ for Sb and Bi are very close to each other. [28,102] Thus, Vereecken et al. concluded that co-deposition of both materials is most likely. Furthermore, they report for the standard potential $U^{\ominus}(\text{Bi}_{1-x}\text{Sb}_x) = 260 \,\text{mV}$ vs. SHE = 16 mV vs. SCE. [28] Then, the equilibrium potentials can be calculated by the Nernst equation

$$U_0 = U^{\ominus} + \frac{59.2 \,\text{mV}}{3} \log_{10} \left([\text{Bi}^{3+}]^{1-x} [\text{Sb}^{3+}]^x \right). \qquad (2.7)$$

For the electrolytes presented here, we have to insert $c(\text{Bi})$, $c(\text{Sb}) = 0.1 \,\text{mol/l}$ $-c(\text{Bi})$, and $c(\text{HCl}) = 1.95 \,\text{mol/l}$ into their equations. This provides the concentrations of uncomplexed ions $[\text{Bi}^{3+}] = 0.57$ and $[\text{Sb}^{3+}] = 53.1 \,\text{nmol/l}$ and the equilibrium potential $U_0(\text{Bi}_{1-x}\text{Sb}_x)$ which will be compared to the results of cyclic voltammetry in the following section.

Cyclic Voltammetry

Cyclic voltammetry (CV) is a method to study the electrochemical properties of the electrolyte. The potential is changed at a constant rate between to prede-

fined potentials. The resulting current response at the cathode for this triangular potential is recorded for several cycles.

In order to find appropriate deposition potentials for the template based deposition of $Bi_{1-x}Sb_x$, cyclic voltammograms were recorded for different electrolytes with $c(Sb) = 0.00$, 0.015, 0.02, 0.04, and 0.10 mol/l using a Gamry potentiostat. The membranes were 30 µm thick, had a channel density of 10^7 cm^{-2}, and channel diameters of 150 nm. CVs were recorded at two different scan rates 50 and 100 mV/s. The resulting CVs are depicted in Figure 2.5(a) and (b), respectively.

Reduction peaks are seen in the potential range -300 to -200 mV vs. SCE, whereas stripping peaks are typically at -100 to 0 mV vs. SCE. The remaining peaks at higher potentials belong to reactions in the electrolyte that could not be identified. Figure 2.6 shows in detail the reduction peaks from the CV recorded at 100 mV/s.

For an electrolyte containing only Bi ($c(Bi) = 0.10$ mol/l, red) or only Sb ions ($c(Sb) = 0.10$ mol/l, black), the reduction peak is measured at -199 and -320 mV vs. SCE, respectively. Figure 2.6 shows that in mixed electrolytes, the reduction peaks for both kinds of ions are very close to the Bi reduction peak and almost overlap suggesting a co-deposition of both ion species in the nanochannels. Furthermore, the reduction peaks shift to more negative potentials for higher Sb content in the electrolyte. Shoulders on the peaks may correspond to the prepeaks attached to the reduction peaks that have been described by Vereecken et al. for thin film deposition and an electrolyte with 2.4 mol/l HCl.[28] However, they were not always resolved in the present experiments.

The reduction peak positions U_p determined from the CVs for the two different scan rates and the equilibrium potentials U_0 evaluated as the mean values of reduction and stripping peak positions are plotted in Figure 2.7. For the determination of the reduction and stripping peak positions and their errors, the mean values and the variances of six cycles were taken. Theoretical values for $U_0(Bi_{1-x}Sb_x)$ obtained from Equation 2.7 are also presented.

U_0 did not change significantly by varying the concentration of Sb, as theoretically expected. The reduction peak positions were identical for both scan rates except for the measurements with the pure Sb electrolyte. Based on these results, $Bi_{1-x}Sb_x$ nanowires were deposited at potentials between -245 to -195 mV vs. SCE.

2.2.3 Electrochemical Deposition Process in Nanochannels

In Figure 2.8, processes occurring at the cathode during deposition are shown. Ions can be directly transferred to a kink position of the crystal or they can be adsorbed at the surface. There, they can reach a kink position by surface diffusion or act as a nucleus for a new grain.[103] In order to deposit large crystallites the
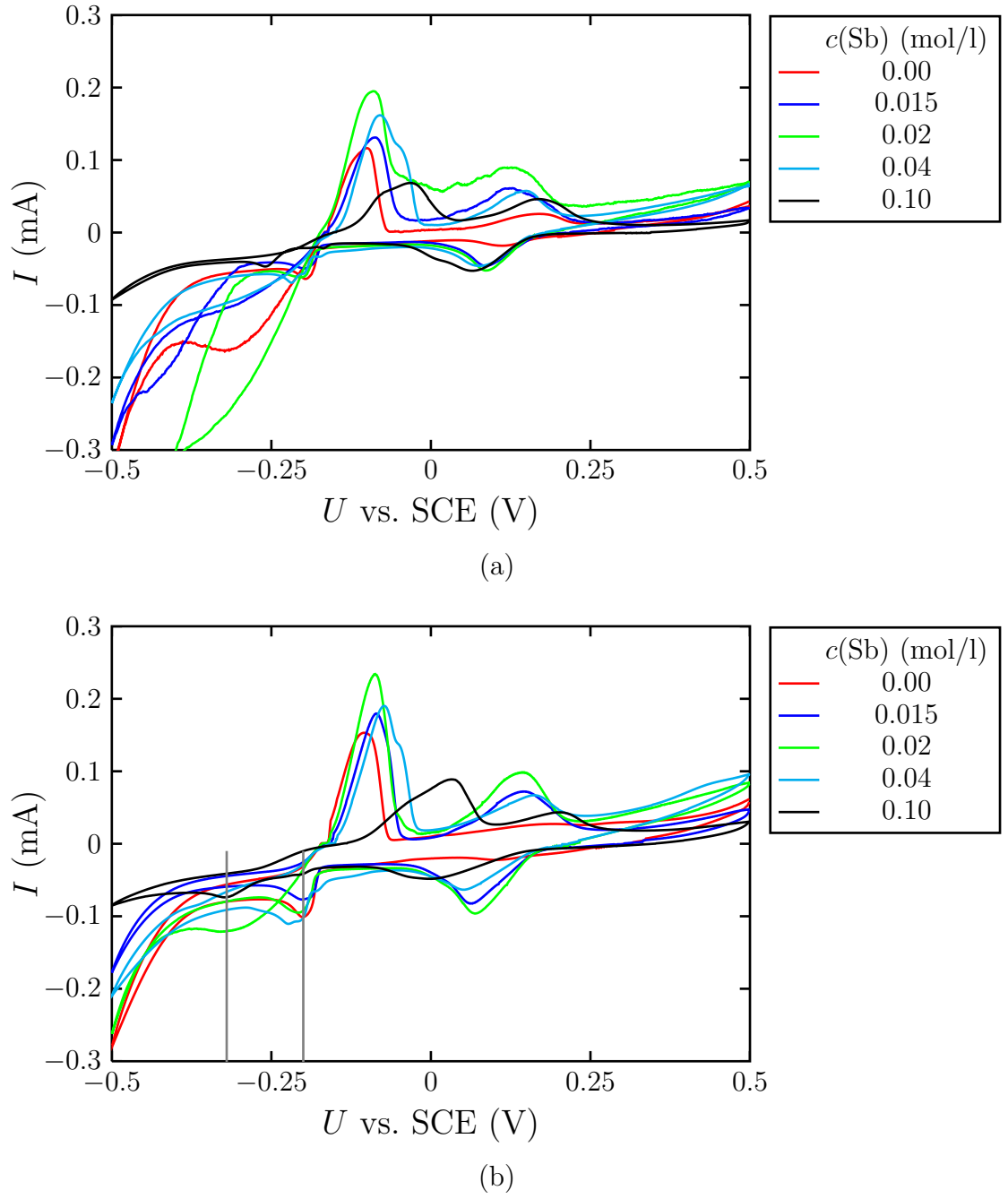
(a)

(b)

Figure 2.5: Cyclic voltammograms for different Sb concentrations in 150 nm diameter nanochannels recorded at scan rates of (a) 50 and (b) 100 mV/s. Reduction potentials for Bi and Sb are marked by gray lines.
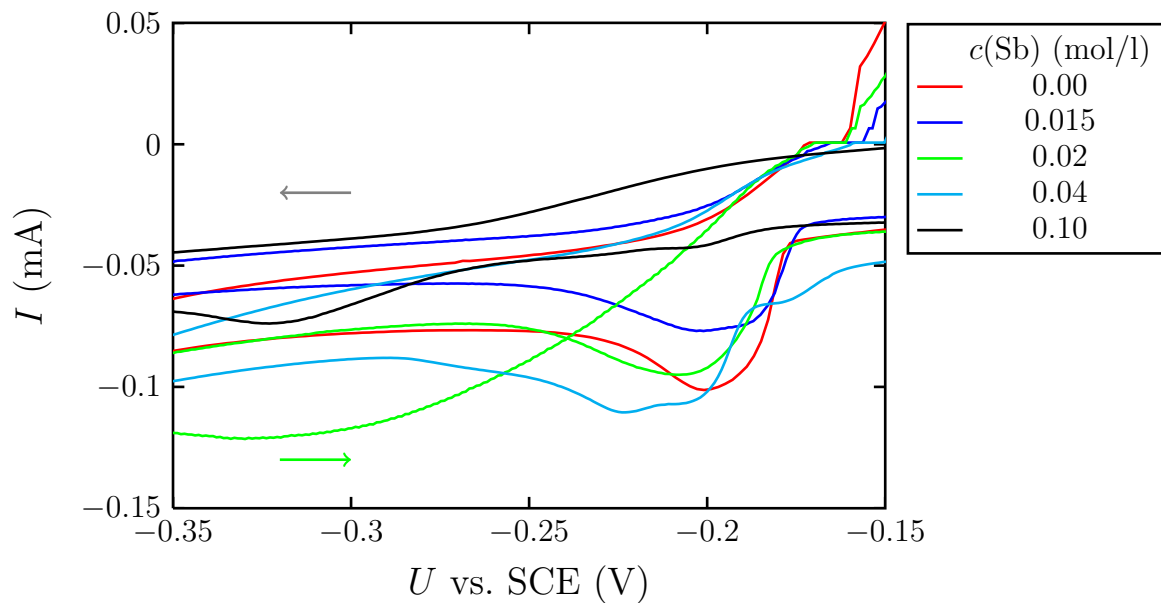
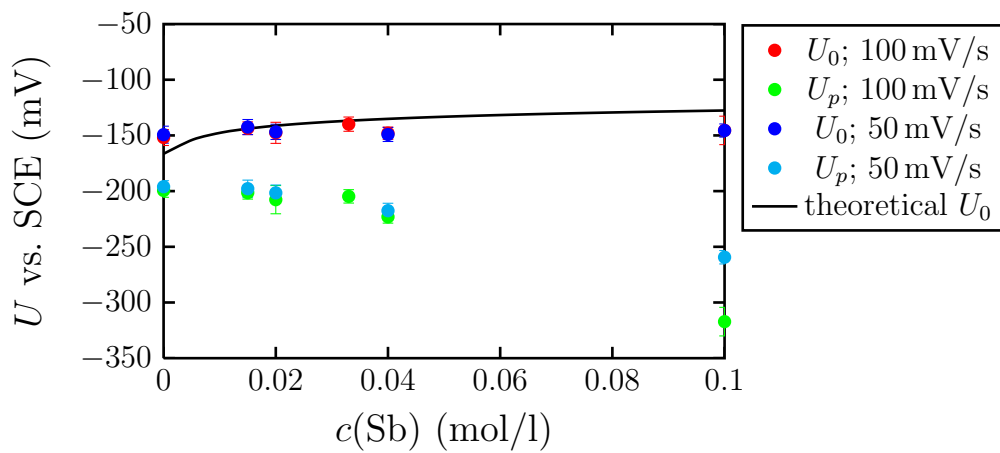Figure 2.6: Extracts of the cyclic voltammograms shown in Figure 2.5(b).

Figure 2.7: Equilibrium potential U_0 and peak potential U_p determined for different scan rates and concentrations. Theoretical values for U_0 are given as black line (compare Equation 2.7).
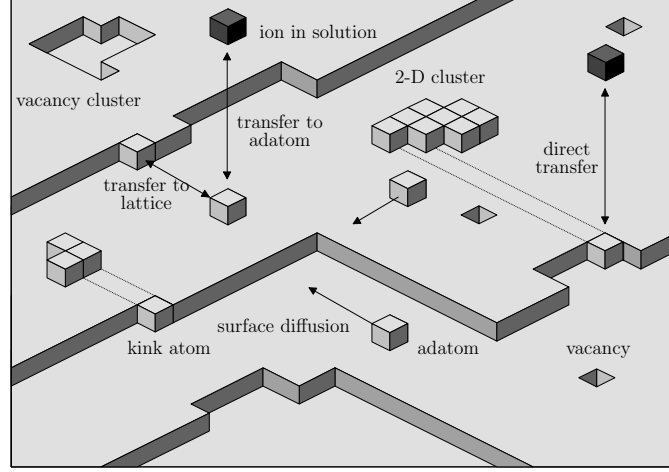
Figure 2.8: Schematic of the processes involved in the deposition according to Budevski.[103]

surface diffusion should be enhanced. At high nucleation rates, lattice defects such as vacancies or dislocations may be formed, and the growth of polycrystalline material is more likely.

Potentiostatic Electrodeposition

For an ion species i of charge z_i, the deposition process is influenced by a concentration gradient towards the cathode which leads to diffusion and an electrical field leading to migration.[104] Hence,

$$j_i = -z_i F \left(c_i \mu_i \nabla \phi + D_i \nabla c_i \right), \tag{2.8}$$

being F the Faraday constant, μ_i the ion mobilities, ϕ the electrical potential, and D the diffusion coefficient.

The electrolyte formerly used for the deposition of pure Bi and the miscible Bi and Sb electrolytes employed in this work have conductivities of 324(5), 432(5), and 435(5) mS/cm at 21.5 °C, respectively. In electrolytes with large conductivities, the migration part can be neglected and diffusion governs the deposition according to Fick's laws

$$\vec{j} = -zFD\nabla c \text{ and } \frac{\partial c}{\partial t} = \nabla \cdot (D\nabla c). \tag{2.9}$$

During the potentiostatic electrodeposition in etched ion-track templates, different regimes with characteristic $I - t$ behaviors are observed (compare with Figure 2.9):

concentration profile

geometry
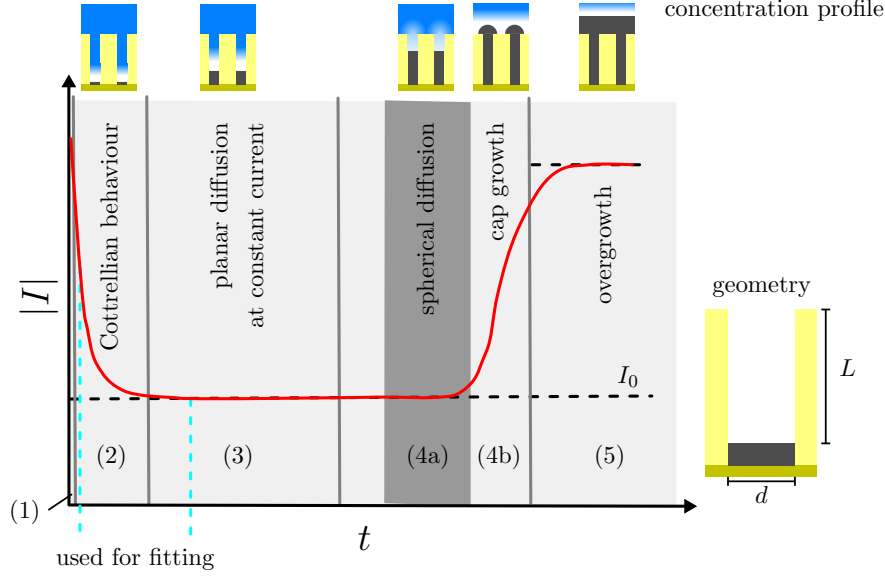
Figure 2.9: Phases distinguished during potentiostatic deposition in nanochannels. The parameters used for fitting of the deposition curves are also indicated.

1. At the beginning, the absolute value of the current drops fast due to a charging of the Helmholtz layer which possesses a capacitance.[104] Furthermore, there is charge transfer and a diffusion layer starts to form.

2. For an ideal infinite plane surface at a constant potential in a diffusion controlled regime, the solution of the time transient of the current can be analytically calculated and is commonly known as Cottrell equation:

$$j(t) = zF(c_0 - c_s)\sqrt{\frac{D}{\pi t}} \text{ and } c(x,t) = c_0 \text{ erf}\left(\frac{x}{\sqrt{4Dt}}\right), \quad (2.10)$$

being c_0 and c_s the bulk and surface concentrations, and erf the error function. However, the diffusion of ions in the electrolyte inside the nanochannels and at microdisk electrodes can differ significantly from the case of planar diffusion at a large and flat working electrode.[105–109]

3. Then, the current remains nearly constant during the deposition in the long nanochannels (length L of order of several $10\,\mu m$). Here, planar diffusion is dominant.

4. When the diffusion layers reach the channel openings, spherical diffusion

towards the opening begins. Also, when the deposition process reaches the end of the channels, so-called caps start to grow and the current increases.

5. Finally, an overlap of these spherical diffusion layers leads again to a planar diffusion. Independently of that, the caps can also grow together and form a layer on top of the sample.

Figure 2.10(a) shows typical deposition $I-t$ curves recorded for different deposition potentials using an electrolyte with $c(\mathrm{Sb}) = 0.02\,\mathrm{mol/l}$. The characteristic decrease in current at the beginning of the deposition is visible. As expected for depositions in identical membranes, the absolute value of the current increases for more negative potentials.

Curves were recorded for the deposition from three electrolytes and different deposition potentials in templates prepared under the same conditions: $70\,\mathrm{nm}$ diameter, $30\,\mu\mathrm{m}$ thick PC templates, and $\phi = 10^9$ channels cm^{-2}. For each sample, the deposition current was divided by the effective area of deposition to obtain and compare the current densities. The Teflon cell has a diameter of $8\,\mathrm{mm}$, and thus, a cross-sectional area of about $50\,\mathrm{mm}^2$. For example, the maximal effective area is only $4\,\mathrm{mm}^2$ for a channel density of $10^9\,\mathrm{cm}^{-2}$ and a channel diameter of $100\,\mathrm{nm}$.

In Figure 2.10(b), the absolute values of the current densities are plotted against the deposition potential applied for the growth of nanowires. $|j|$ increases with increasing overpotential, but a dependence on the composition of the electrolyte is not evident. For comparison, reported current densities chosen for galvanostatic deposition of thin films are $40 - 100$[30] and $70\,\mathrm{A/m}^2$.[28]

Etched ion-track membranes with a back electrode can be seen as an array of recessed microelectrodes rather than a plane surface. As a consequence, the whole deposition process is, in general, not adequately described by Equation 2.10. Bond et al. found an analytical solution for a single recessed microelectrode with diameter $d = 2r$, length L (compare Figure 2.9), no convection, and a constant concentration c_0 at the channel opening.[106] This solution can be expressed by the θ_3 function[110]

$$I = \frac{4\pi z F c_0 D r^2}{4L + \pi r}\theta_3\left(0, \frac{16Dt}{(4L + \pi r)^2}\right) \text{ and } \theta_3(0, x) = 1 + 2\sum_{n=1}^{\infty}\exp(-\pi^2 n^2 x). \quad (2.11)$$

For $t \to 0$, it approximates Equation 2.10, but for $t \to \infty$, there is a limiting current given by
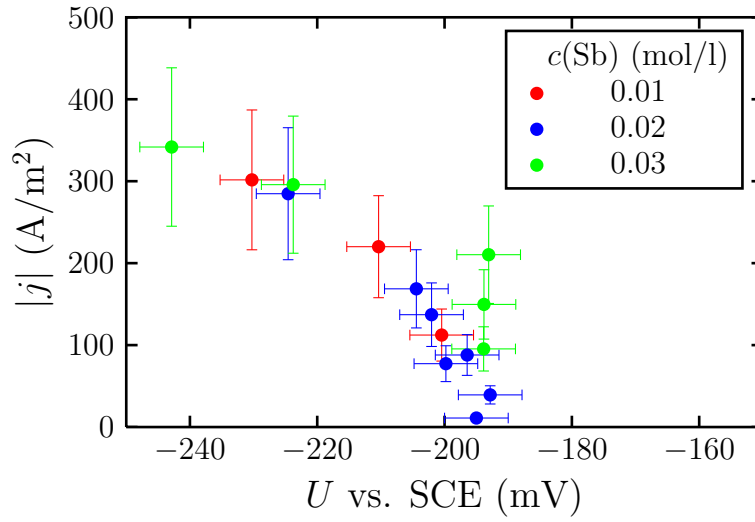
$$I_0 = \frac{4\pi z F c_0 D r^2}{4L + \pi r}. \quad (2.12)$$

In the case of multichannel polymeric membranes, the currents in Equations 2.11 and 2.12 have to be multiplied by the number of channels $N = \pi/4\,\phi\,d_{\mathrm{cell}}^2$, with channel density ϕ and $d_{\mathrm{cell}} = 8\,\mathrm{mm}$. The errors of ϕ and the channel diameter d
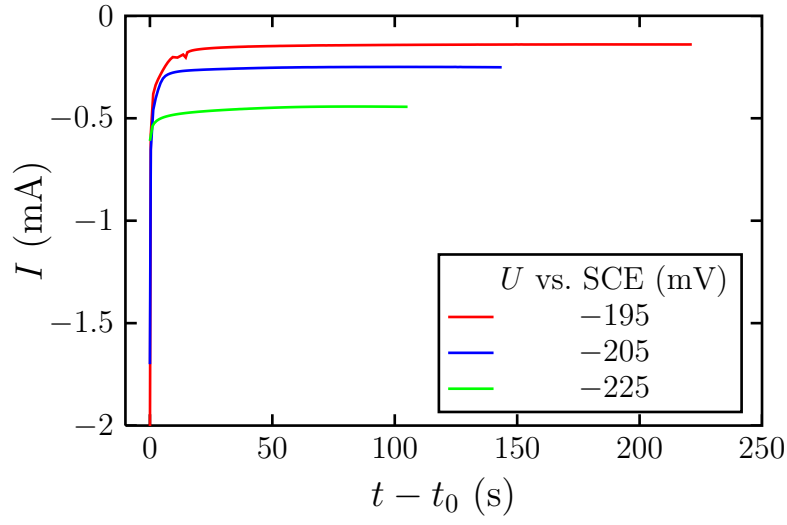
(a)

(b)

Figure 2.10: (a) Selected $I-t$ deposition curves for $c(Sb) = 0.02\,\mathrm{mol/l}$ and different deposition potentials and (b) Current densities during the deposition of nanowires with $70\,\mathrm{nm}$ diameter in $30\,\mu\mathrm{m}$ thick PC templates with 10^9 channels/cm^2.
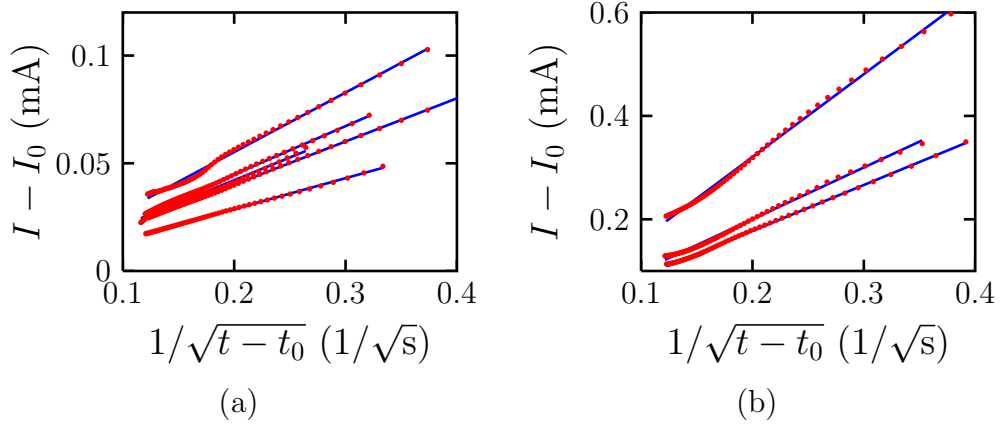
Figure 2.11: Examples of the fits for two series with different diameter of nanowires as Cottrell plots for wire diameters of (a) 30 and (b) 100 nm.

are typically over 10 %. Therefore, the effective area of deposition is also subject to a large error. As a consequence, methods that are usually highly accurate, as the determination of diffusion constants by the Cottrell equation, are much less exact for the deposition in polymeric membranes.

Values for D and N can be estimated from the deposition curves by fitting the first $20-30\,$s after the counter electrode is immersed. The Cottrellian part is proportional to $N\sqrt{D}$ according to Equation 2.10 and the limiting current to ND according to Equation 2.12. Therefore, a simplified fit function was employed

$$I(t) = \frac{p}{\sqrt{t - t_0}} + I_0, \tag{2.13}$$

with p, t_0, and I_0 being the scaling factor, the starting time, and the limiting current, respectively. Due to the charge transfer process, the first $2\,$s were not regarded. Furthermore, c_s was assumed to be zero. Strictly speaking, it is a function of the overpotential.[104]

Figure 2.11 shows examples for Cottrell plots, in this case the difference of the deposition current and the limiting current I_0 as function of $1/\sqrt{t - t_0}$, and the respective fits. In this illustration, it is not distinguished between different deposition potentials and $c(Sb)$. In most cases the deposition curves follow a straight line.

From series of depositions performed for different average diameters and template thicknesses in PC, the diffusion coefficients D obtained from the fit values from Equation 2.13 are shown in Figure 2.12 as a function of $c(Sb)$. The error bars correspond to the error of the individual fit. The red and dark blue marks belong to the deposition curves shown in Figure 2.11.
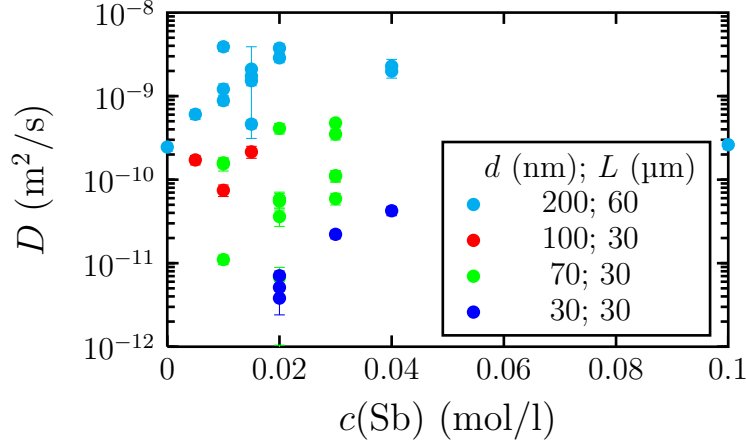
Figure 2.12: Diffusion coefficients obtained by fitting Equation 2.13 to the deposition curve for different wire diameters and template thicknesses as a function of composition of the electrolyte.

It can be seen that the values obtained for nanowire arrays deposited under the same conditions can scatter over one order of magnitude. Typical diffusion coefficients observed in bulk solutions are of the order of $10^{-9}\,\mathrm{m^2\,s^{-1}}$, as observed in this case for thick nanowires and long channels. For decreasing nanochannel diameter, the trend of the diffusion coefficient is towards lower values, as expected for nanoporous media.[111] Also, the calculated diffusion coefficients seems to be larger for higher Sb content. Errors of this analysis may be introduced by the shape of the back electrode. The sputtered gold layer can form rings reaching into the nanochannels.[112] Also, ion-track etched membranes were shown to possess additional fixed charges at the inner surface of the channel.[113,114] Finally, c_s and a possible difference of the Diffusion coefficients of Bi and Sb ions were neglected.

Pulsed Electrodeposition

In addition to the preparation by potentiostatic deposition, nanowires were also prepared using a pulsed potential. This method is expected to have various advantages such as a better control over diffusion of ions towards the cathode, a better control over the texture of the nanowires, and a more homogeneous growth process.[115]

Figure 2.13 displays schematically such pulses applied during electrodeposition, being t_A the on-time, U_A the on-potential, t_B the off-time, and U_B the off-potential. During t_A, ions will be reduced, while during t_B no reduction takes place and the thickness of the diffusion layer is decreasing.
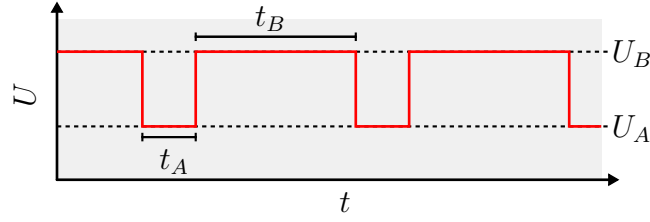
Figure 2.13: Schematic of potential pulses.

The cathodic potential was chosen at $U_A = -220\,\mathrm{mV}$ vs. SCE for $t_A = 20\,\mathrm{ms}$, followed by an off-pulse at $U_B = -150\,\mathrm{mV}$ vs. SCE for $t_B = 100\,\mathrm{ms}$. U_B was chosen as close as possible to the the equilibrium potential, where the measured current converges to $0\,\mathrm{mA}$. Due to the short time scales, the potentials and the analog output voltage of the Keithley Picoammeter where displayed on an oscilloscope. Also, the DAQ card was programmed to record both signals.

In Figure 2.14(a), different curves characteristic for the pulsed deposition are shown. The channel density was $10^9\,\mathrm{cm}^{-2}$ and the Sb concentration $c(\mathrm{Sb}) = 0.03\,\mathrm{mol/l}$. The $U - t$ curve of a selected part during the nanowire deposition shows how well the potentiostat controls the deposition potential. It is typically less than $5\,\mathrm{mV}$ off the desired potential which is worse than for potentiostatic deposition. Furthermore, the measurements of the potential show some noise probably due to the fast data acquisition at $1\,\mathrm{kHz}$.

The corresponding $I - t$ curve is depicted as well for the same time interval. Deposition (negative current values) and off-pulse both have a decreasing absolute value typical of the discharging of the Helmholtz double layer.

The mean current over such pulses is given in Figure 2.14(b). These curves show similar characteristic features like the $I - t$ curves of potentiostatic deposition: There is a plateau for the wire deposition and an increase of the absolute value of the current when caps are forming. For $c(\mathrm{Sb}) = 0.01\,\mathrm{mol/l}$, also a deposition curve for potentiostatic deposition under otherwise same conditions is included. The absolute value of the current is much larger and the cap growth starts already at $t = 250\,\mathrm{s}$. Thus, for pulsed deposition, the cap growth is delayed by a factor corresponding to the ratio between on- and off-time.

2.3 Conclusion

Electrolytes based on hydrochloric acid and Bi(III)- and Sb(III)-chlorides were developed. Both electrolytes are easily miscible for the deposition of alloy nanowires. Cyclic voltammetry was performed, to find appropriate deposition potentials for
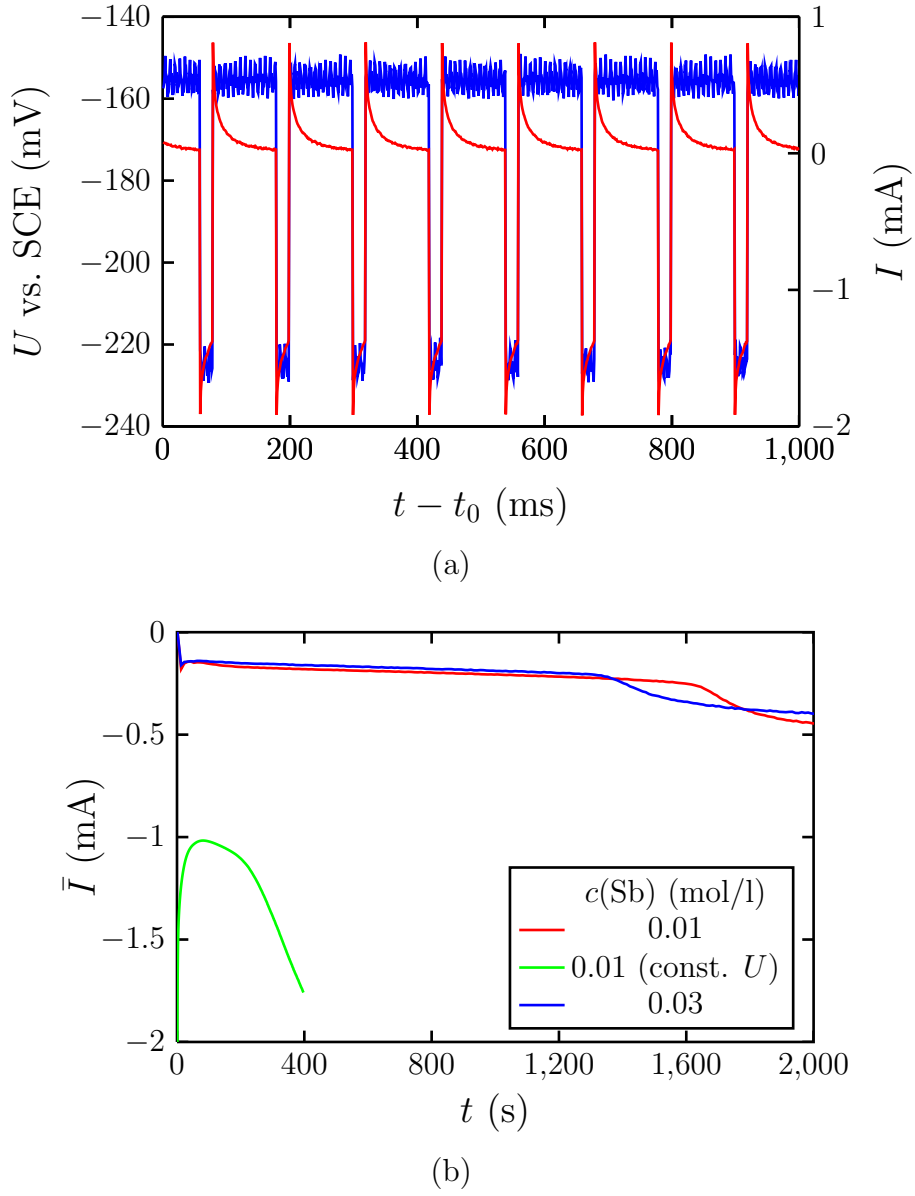
(a)

(b)

Figure 2.14: Characteristic curves of the deposition process for $d = 100\,\text{nm}$ and a channel density of $10^9\,\text{cm}^{-2}$. (a) Part of $U - t$ (blue) and $I - t$ (red) curves starting at $t_0 = 352\,\text{s}$ and (b) mean current $\bar{I}$ as function of time. For comparison a deposition curve for potentiostatic deposition is included.

the fabrication of nanowires in the nanochannels of ion-track etched polymer templates.

During deposition, the measured $I-t$ curves displayed the distinguished regimes known from the deposition of other materials in nanochannels. Most of them followed a $1/\sqrt{t}$ law at the beginning and then reached a constant current. As expected, a larger overpotential results in a larger deposition current. However, the current is not influenced significantly by the Sb concentration.

Estimated diffusion coefficients show a trend towards lower values for thinner nanochannels. In the literature, a deviation from the deposition at large, plain surfaces is expected. However, in practice, not all boundary conditions are well known. Further systematic experiments varying the channel length, the polymer material, and improving the structure of the backelectrode are necessary. In this work, the difference of the diffusion coefficients for Bi and Sb ions was neglected, and it would be interesting to investigate the influence of the overpotential on the reactant concentration at the cathode. In order to achieve a better understanding of the deposition processes, the deposition process could be simulated by, e. g., finite element methods.

Furthermore, pulsed electrodeposition with short pulses has been employed to slow down the deposition. Typically, the growth rates are lower by a factor given be the ratio of on- and off-time.

3 Characterization of Morphology, Crystalline Structure, and Composition of Smooth and Rough $\mathrm{Bi}_{1-x}\mathrm{Sb}_x$ Nanowires

symbol	quantity
$a, b, c, \alpha, \beta, \gamma$	cell parameters
A	atomic weight
β	full width at half maximum (FWHM)
$c(\mathrm{Sb})$	concentration of Sb ions in electrolyte
d_{hkl}	distance between lattice planes (hkl)
E_0	initial energy of electron beam
E_c	critical excitation energy
θ	diffraction angle
hkl	Miller indices
I	intensity of X-rays
k_{AB}	Cliff-Lorimer coefficient
λ	wavelength
μ/ρ	mass attenuation coefficient
ρ	density
τ, K	apparent size, Scherrer constant
TC	texture coefficient
x	concentration of Sb in nanowires
z	depth / depth of information
Z	atomic number
ω	circle in XRD
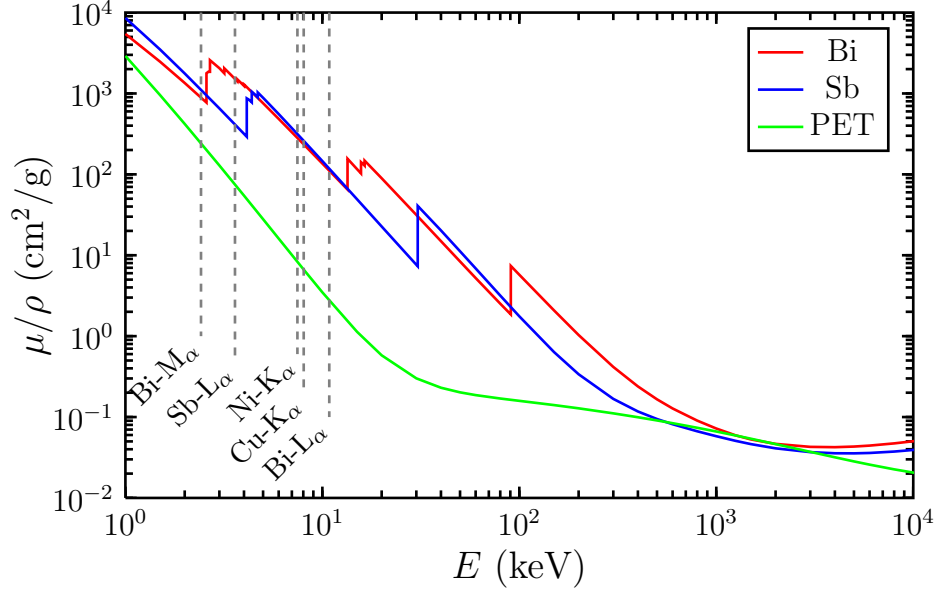
Figure 3.1: Mass attenuation coefficients of X-rays for PET, Sb, and Bi according to the database of the NIST.[116]

3.1 Experimental Methods

3.1.1 Absorption of X-Rays in Matter

The absorption of X-rays follows the law

$$I(z) = I_0 \exp[-(\mu/\rho) \cdot z], \tag{3.1}$$

being I_0 the initial intensity, z the depth, and μ/ρ the attenuation coefficient given in Figure 3.1. The absorption of X-rays plays an important role for several characterization methods employed. First, X-ray diffraction measurements are performed on a composite consisting of parallel nanowires embedded in a polymer matrix (PET and PC). Because of the much larger μ/ρ of Bi and Sb compared to a polymer like PET, the penetration depth in the membrane is larger.[116] The corresponding attenuation lengths, where the intensity drops to $1/e$, are given in Table 3.1. As a consequence, the absorption of Cu-K$_\alpha$ in the template is negligible in X-ray diffraction experiments.

Secondly, the absorption is important for the interpretation of spectra obtained from energy dispersive X-ray spectroscopy (EDX). The nanowires are so thin that the TEM-EDX spectra can be analyzed using the Cliff-Lorimer method. This method neglects absorption effects and relates the ratio of the concentrations of

	Bi-M_α	Bi-L_α	Sb-L_α	Cu-K_α
in Bi	1.1	8.6	0.67	4.3
in Sb	1.1	12	3.3	5.7
in PET	24	2300	85	1100

Table 3.1: X-ray attenuation lengths in µm.

two elements A and B in weight percent, $c_{A,B}$, with the ratio of characteristic X-rays detected, $I_{A,B}$, via a proportionality constant, the Cliff-Lorimer factor k_{AB}:[117]

$$\frac{I_A}{I_B} = k_{AB}\frac{c_A}{c_B}. \tag{3.2}$$

Other approaches include the absorption effects in quantitative TEM-EDX analysis like the so-called ζ-factor method, which also provides a material thickness from numerical iteration steps.[118,119]

However, for EDX measurements in an SEM, the quantification methods usually assume a flat surface and a thick sample. For nanowires, the results of quantitative analysis, therefore, may deviate from TEM-EDX results.

3.1.2 Electron Microscopy

The transport properties of $Bi_{1-x}Sb_x$ are anisotropic and grain boundaries and surface structure have a large influence on the thermoelectrical properties. Thus, composition, crystallite size and orientation, and surface structure of the nanowires have to be investigated in detail to be able to understand the thermoelectric properties. In this work, different microscopes were employed for the characterization of the nanowires.

1. At GSI, surface morphology and composition were characterized with a JEOL JSM-7401F high-resolution scanning electron microscope with a STEM-in-SEM detector for the detection of transmitted electrons and a Bruker XFlash 5030 detector system for quantitative analysis of the nanowires. The cold field emitter usually provides only small currents of the order of 0.25 nA for microanalysis. However, large currents could destroy or at least modify the sample significantly by heating.

2. In Tübingen[‡], the nanowires were investigated by bright-field (BF) and dark-field (DF) imaging in a Zeiss 912Ω transmission electron microscope (TEM)

[‡]Prof. O. Eibl and Dr. N. Peranio, Institut für Angewandte Physik, Universität Tübingen

with an electron energy of $E_0 = 120\,\text{keV}$ to analyze the surface and the crystallite size and orientation. The fine aperture for the DF imaging had a diameter of 750 nm. In addition, the composition of the nanowires was analyzed to accuracies typically below 1 atomic % by means of a self-calibrated TEM-EDX system.[120,121]

3. In Stuttgart[§], high-resolution transmission electron microscopy (HR-TEM) in a JEM4000FX TEM provided information about the structure of the crystallites of smooth and rough nanowires. Furthermore, quantitative analysis was performed by EDX. Here, the electron energy was $E_0 = 400\,\text{keV}$.

As will be described in detail in Section 3.1.5, nanowires were prepared on TEM-grids made of Ni or Cu and a lacey or holey carbon film as substrate for SEM and TEM analysis. This minimizes background effects for the EDX measurements and enables transmission electron microscopy and detecting transmitted electrons in the STEM-in-SEM. For EDX analysis, nanowires positioned across a hole in the middle of the carbon film were selected.
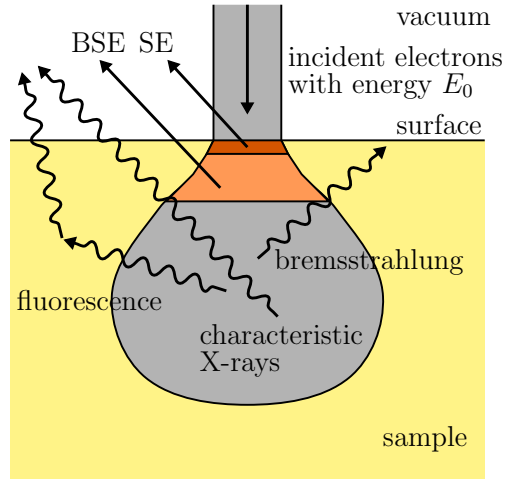
Figure 3.2: Schematic of the excitation bulb. The incident electrons lead to an emission of secondary electrons (SE) and some are backscattered (BSE). Characteristic X-rays and bremsstrahlung are also produced.

3.1.3 Energy Dispersive X-Ray Spectroscopy

When the incident electron beam interacts with the sample, several processes illustrated in Figure 3.2 occur: fluorescence, bremsstrahlung, ionization of atoms, and emission of secondary and Auger electrons. These processes form an excitation "bulb". Using Castaing's equation[122] one can estimate the depth of information obtained for different beam energies and materials:

$$z = 0.033 \left(E_0^{5/3} - E_c^{5/3} \right) \frac{A}{\rho Z}, \tag{3.3}$$

being ρ the density of the material, A the atomic weight, and Z the atomic number.

For $E_0 = 10 \, \mathrm{keV}$ and the critical excitation energies for Bi-M, $E_c = 2.580 \, \mathrm{keV}$, and Sb-L, $E_c = 4.132 \, \mathrm{keV}$, Equation 3.3 yields an information depth z of 0.35 and $0.43 \, \mu\mathrm{m}$, respectively. The nanowires are by an order of magnitude thinner than these values.

In the JEOL-SEM, E_0 can be selected up to $30 \, \mathrm{keV}$. For the excitation energy, $10 \, \mathrm{keV}$ was chosen to perform quantitative analysis by using the Sb-L and the Bi-M line series.

In Figure 3.3, the transitions and energies for the K, L, and M lines,[123] and intensities for K and L lines[124] of lines of interest in X-ray spectroscopy are collected for Bi and Sb. In the spectrum of the M lines, the intensities of the M_α lines account for 65% of the overall intensity.[125]

Figure 3.4 displays simulations performed with CASINO V2.42[126] of electrons with $E_0 = 10 \, \mathrm{keV}$, penetrating Bi and Sb films of different thickness and a spot size of $10 \, \mathrm{nm}$. The color of the trajectories illustrates the electron energy. For Bi and Sb, the backscattering rates were about 0.48 and 0.40 for thicker layers, where "bulbs" are fully developed, and 0.09 and 0.04 for the thinnest layers, respectively. In the case of nanowires, even less material is available for interaction. Thus, a decreased signal is expected.

3.1.4 X-Ray Diffraction

X-ray diffraction experiments on nanowire arrays were performed to obtain information about the preferential orientation of the grains inside the nanowires and the mean composition of the nanowires. The X-ray diffractograms were taken with a HZG-4 Seifert Analysis X-ray diffractometer and Cu-K$_\alpha$ radiation. The emission lines used for X-ray diffraction are Cu-K$_{\alpha 1}$ and Cu-K$_{\alpha 2}$ with wavelengths λ(Cu-K$_{\alpha 1}$)= 0.15405929(5) nm and λ(Cu-K$_{\alpha 2}$)= 0.15444274(5) nm and intensity ratio $1 : 0.52$.[127] The Cu-K$_\beta$ lines where sorted out with a monochromator placed

---

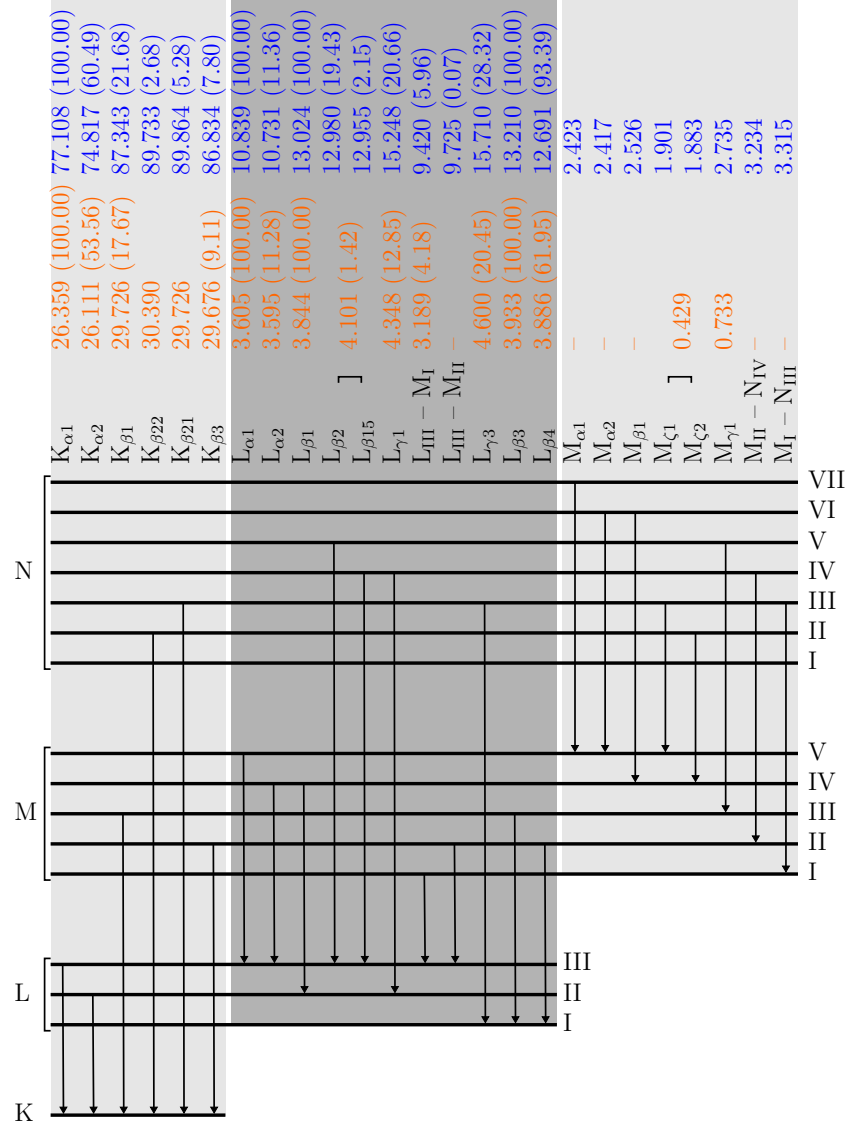[§]Dr. W. Sigle, Dr. P. Kopold, and B. Özdöl, Max Planck Institute for Intelligent Systems, Stuttgart

Figure 3.3: Characteristic X-ray emission lines especially interesting for X-ray spectroscopy. The values of the respective line energies are given in keV for bismuth (blue) and antimony (orange) with the intensity in % relative to the strongest lines of the respective series in brackets for the K and L series.
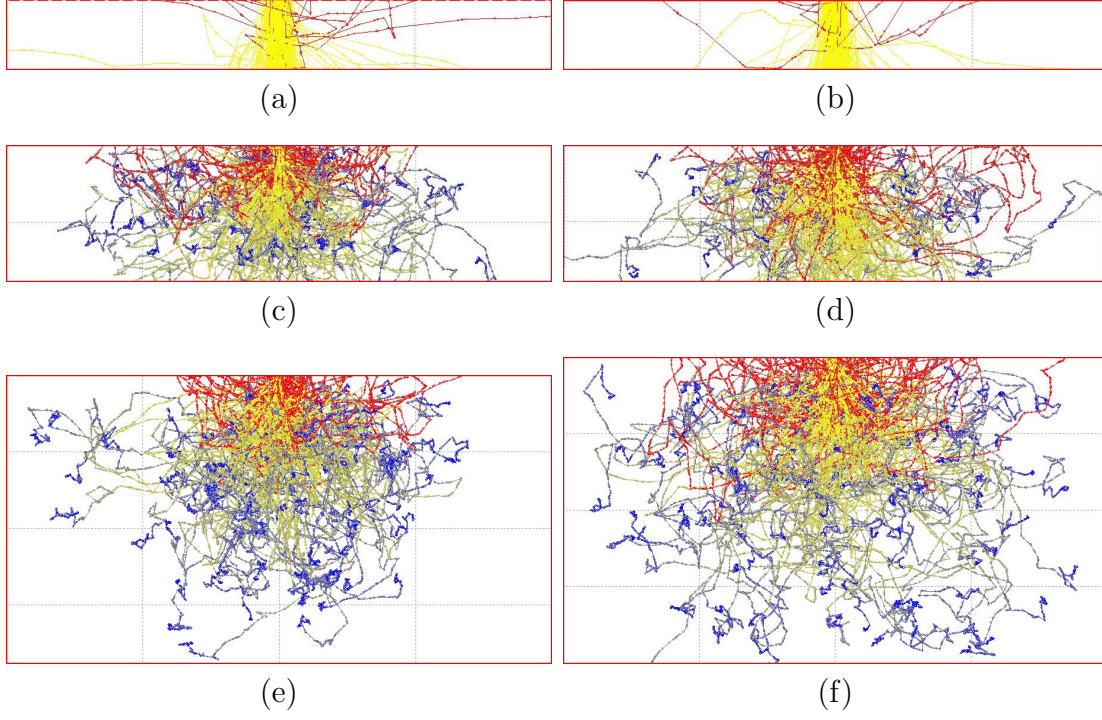
Figure 3.4: Simulation with CASINO V2.42 using $E_0 = 10\,\text{keV}$ and a spot size of $10\,\text{nm}$ for Bi (a,c,e) and Sb (b,d,f). The thicknesses were (a,b) 20 (c,d) 200, and (e,f) $2000\,\text{nm}$, the displayed width is $80\,\text{nm}$ for (a,b) and $800\,\text{nm}$ for (c–f). For (e) and (f), the displayed height was limited to 400 and $450\,\text{nm}$, respectively.

after the X-ray generator. The incident X-Rays are diffracted by lattice planes with Miller indices hkl according to Bragg's law

$$n\lambda = 2d_{hkl} \sin\theta, \tag{3.4}$$

being n the order, d_{hkl} the spacing between lattice planes, and θ the diffraction angle.

As discussed in Chapter 1.3.1, the $Bi_{1-x}Sb_x$ alloys belong to the space group $R\bar{3}m$. Due to the symmetry of this space group, the values of hkl for "allowed" reflections are confined to values for which $-h + k + l = 3n$, with n integer, holds true.[128] The shape and position of diffraction peaks can be influenced by different effects, e. g. stacking faults, grain boundaries, and chemical heterogeneities.[129,130]

In the employed Seifert Analysis software, the Pseudo-Voigt function is fitted to the peak forms:

$$F_{\mathrm{PV}}(2\theta) = I_0 \left[\frac{\eta}{1 + k(2\theta - 2\theta_0)^2} + (1 - \eta) \exp\left(-\ln 2\ k(2\theta - 2\theta_0)^2\right) \right] \tag{3.5}$$

by fit parameters k and η, and

$$\beta = 2\sqrt{\frac{1}{k}}. \tag{3.6}$$

Alternatively, the Pearson-VII function can be used:[131]

$$F_{\mathrm{P\text{-}VII}}(2\theta) = \frac{I_0}{(1 + k'(2\theta - 2\theta_0)^2)^m} \tag{3.7}$$

with m and k' as fit parameters, and a full width at half maximum of

$$\beta = 2\sqrt{\frac{2^{1/m} - 1}{k'}}. \tag{3.8}$$

A comprehensive study of the lattice parameters of $Bi_{1-x}Sb_x$ alloys was reported by Dismukes et al.: They showed that the lattice parameters a and c decrease monotonically for increasing Sb concentration, however, not perfectly following Vegard's law.[79] Therefore, a shift of the diffraction peaks in $\omega - 2\theta$ scans to larger angles is expected for larger Sb content in the nanowires, and the positions of the reflections should provide information about the Sb concentration x.

From the relative peak intensities of an $\omega - 2\theta$ scan, the texture can be calculated by comparison with standard powder diffraction patterns. These are available in the JCPDS database for pure Bi (JCPDS-44-1246 PDF-2 Sets 1-89) and Sb (JCPDS-35-732). Then, for a diffractogram with n reflections with Miller indices $\{hkl\}_i$, the texture coefficient TC is given by the definition[47]

$$TC(\{hkl\}_j) = n \cdot \frac{I(\{hkl\}_j)/I_0(\{hkl\}_j)}{\sum\limits_{i=1}^{n} I(\{hkl\}_i)/I_0(\{hkl\}_i)}. \tag{3.9}$$
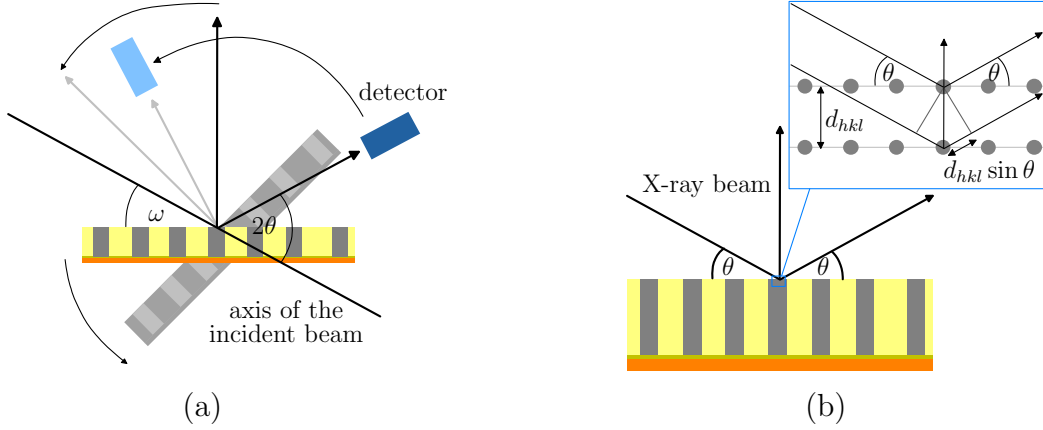
Figure 3.5: Schematic of reflecting geometry and planes important for the interpretation of the texture of the sample. (a) XRD geometry and (b) orientation of planes and nanowires.

In the case of polycrystalline samples, TC equals one for all $\{hkl\}_i$. $TC(\{hkl\}_i) > 1$ indicates a preferential orientation of the grains in the sample. As illustrated in Figure 3.5, information is obtained only parallel to the wire axis for our reflecting Bragg-Brentano geometry. However, a so-called fiber texture could be present which is sometimes observed for electrochemically deposited samples.[132] In such a case, the sample would appear "polycrystalline" perpendicular to the wire axis.

Another important property of the sample is the apparent size τ of the crystallites, which is given by the Scherrer equation[133]

$$\tau = \frac{K\lambda}{\beta_{\text{corr}} \cos\theta}, \tag{3.10}$$

being β_{corr} the FWHM of the peak without instrumental broadening and K the Scherrer constant, which is, strictly speaking, a function of hkl and the shape of the reflecting object.[134] In this work, it was assumed as 0.9.

In order to calculate β_{corr}, the instrumental broadening β_{i} (in °) was determined with an Al_2O_3 target (NIST standard 1976a)[135] and the Caglioti function[136,137]

$$\beta_{\text{i}} = \sqrt{u \tan^2(\theta) + v \tan(\theta) + w}, \tag{3.11}$$

was fitted to the measured β values of the Al_2O_3 diffraction pattern providing the values $u = 0.019(4)$, $v = -0.019(5)$, and $w = 0.008(2)$.

However, not only the apparent size of the crystallite, but also a distribution in the composition and strain can broaden the peak in X-ray scattering experiments. To analyze, if strain as deformation $\epsilon = \Delta d/d$ is present in the sample, the

method of Williamson and Hall was employed.[138,139] For Lorentzian curves β_{corr} is evaluated from the measured β by deconvolution using Stokes' method[140]

$$\beta \;=\; \beta_{\text{size}} + \beta_{\text{strain}} + \beta_{\text{i}} \tag{3.12}$$

$$\beta_{\text{corr}} \;=\; \beta - \beta_{\text{i}} = \frac{K\lambda}{\tau\cos\theta} + 4\epsilon\tan\theta \tag{3.13}$$

and for Gaussian curves by

$$\beta^2 \;=\; \beta_{\text{size}}^2 + \beta_{\text{strain}}^2 + \beta_{\text{i}}^2 \tag{3.14}$$

$$\beta_{\text{corr}}^2 \;=\; \beta^2 - \beta_{\text{i}}^2 = \left(\frac{K\lambda}{\tau\cos\theta}\right)^2 + (4\epsilon\tan\theta)^2. \tag{3.15}$$

3.1.5 Preparation of Nanowires

Due to the brittleness of $Bi_{1-x}Sb_x$ nanowires, special care is needed during the preparation and handling of the nanowires for further characterization by TEM and SEM.

For the nanowires embedded in PC, a piece of the sample with the size of a few mm^2 was placed on the side of a self-made Teflon funnel. Dichloromethane was pipetted onto the sample, until the PC was dissolved and the nanowires were washed down from the back electrode to a TEM grid that acted as "filter". The grid with the nanowires was further rinsed to remove polymer remains. Before this treatment, the Au back layer can be removed with KI/I_2 solution (1 g KI, 1 g I_2, and 20 ml water).

Nanowires embedded in PET were immersed at least one day in 20 ml 9:1 v/v chloroform 1,1,1,3,3,3-hexafluoro-2-propanol solution. Then, the wires were separated from the Au back layer by ultrasound, filtered through a grid, and rinsed again with fresh solution.

Finally, for X-ray diffraction measurements the nanowires were kept embedded in the polymer. In later experiments, the Au back electrode was removed by means of the KI/I_2 solution and the sample was placed on a silicon wafer. Then, wafer and sample were attached to a stainless steel adapter with small magnets. This led to a better alignment and flatness of the sample compared to mounting with double-faced adhesive tape.
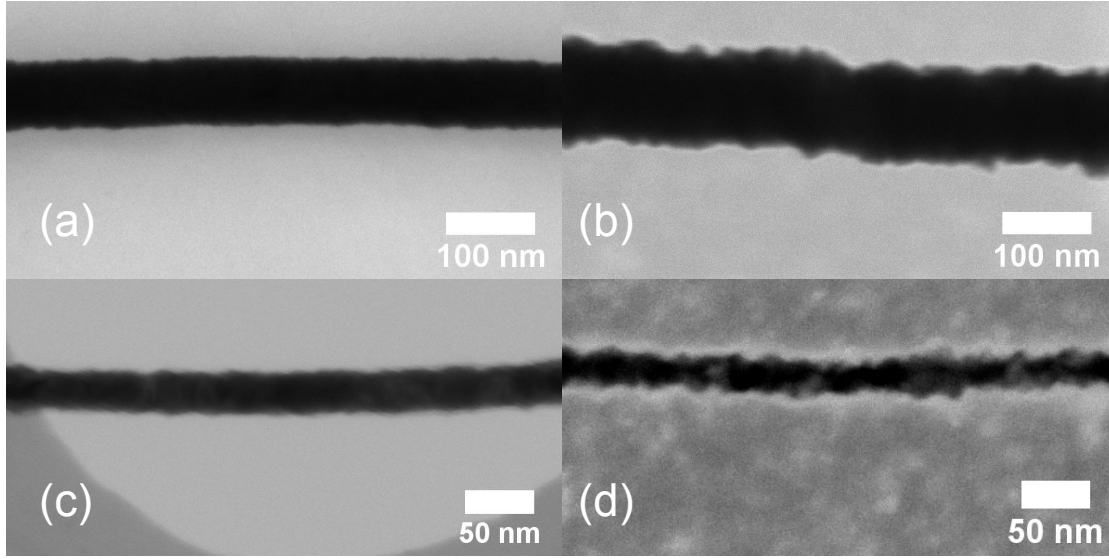
Figure 3.6: HR-SEM images of individual Bi$_{1-x}$Sb$_x$ nanowires with average diameters of (a) 70, (b) 90, (c) 30, and (d) 20 nm. The wires in (a,c) were deposited in PC membranes and exhibit smooth contours. The wires in (b,d) were deposited in PET membranes and display rougher contours.

3.2 Bi$_{1-x}$Sb$_x$ Nanowires Deposited by Potentiostatic Deposition

As discussed in Chapter 1, the surface roughness of nanowires is expected to have a large influence on the thermoelectric properties. In this work, both smooth and rough Bi$_{1-x}$Sb$_x$ nanowires were fabricated by electrodeposition in membranes of two different polymers, PC and PET, respectively.

Etching of PC foils irradiated with swift heavy ions led to channels with smooth walls, whereas etching of PET led to channels with rough walls, probably due to the partially crystalline structure of PET. Electrodeposited materials can adopt the shape and size of the hosting channels. Thus, the roughness of the channels in ion-track etched PC and PET can be visualized by using nanowires as replicas. Figure 3.6 shows Bi$_{1-x}$Sb$_x$ nanowires deposited in PC (a,c) and PET (b,d) membranes. For comparison, nanowires of similar diameters were chosen: (a,b) 70 and 90 nm and (c,d) 20 and 30 nm. The surface roughness of the nanowires deposited in PET membranes is larger than for the respective counterpart deposited in PC membranes. In this chapter, the morphology, composition, and crystalline structure of both kinds of nanowires is described.
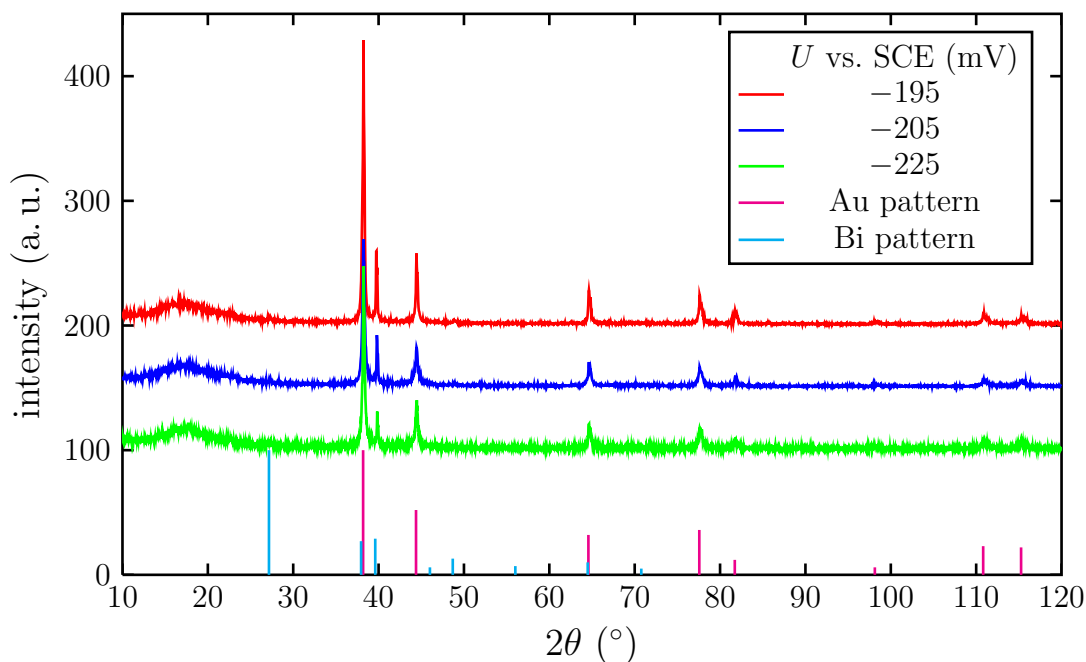
Figure 3.7: X-ray diffractograms measured on nanowire arrays with wire diameter $65 - 75\,\text{nm}$ deposited in $30\,\mu\text{m}$ thick membranes. The Sb concentration in the electrolyte was $c(\text{Sb}) = 0.01\,\text{mol/l}$ and the deposition potential was varied. Selected lines from Bi (JCPDS-44-1246 PDF-2 Sets 1-89) and Au (JCPDS-4-784 PDF-2 Sets 1-89) standard patterns are indicated.

3.2.1 Smooth Nanowires Deposited in PC Membranes

Compositional Analysis by XRD   To study the influence of both Sb concentration in the electrolyte $c(\text{Sb})$ and deposition potential U on the composition of the resulting $\text{Bi}_{1-x}\text{Sb}_x$ alloy nanowires, three electrolytes with $c(\text{Sb}) = 0.01$, 0.02, and $0.03\,\text{mol/l}$ were prepared and nanowire arrays were deposited at four different potentials $U = -195, -205, -225$, and $-245\,\text{mV}$ vs. SCE at room temperature. The PC templates had a pore density of $10^9\,\text{cm}^{-2}$, channel diameters of $\sim 70\,\text{nm}$, and a thickness of $30\,\mu\text{m}$. The resulting arrays were analyzed by XRD.

Figure 3.7 shows diffractograms measured on $\text{Bi}_{1-x}\text{Sb}_x$ nanowire arrays deposited using electrolytes with $c(\text{Sb}) = 0.01\,\text{mol/l}$ and deposition potentials of $-195, -205$, and $-225\,\text{mV}$ vs. SCE. Lines of Bi and Au standard powder diffraction patterns are also indicated. The $\omega - 2\theta$ scans exhibit Au reflections corresponding to the polycrystalline working electrode, a broad peak at $2\theta = 10 - 20°$
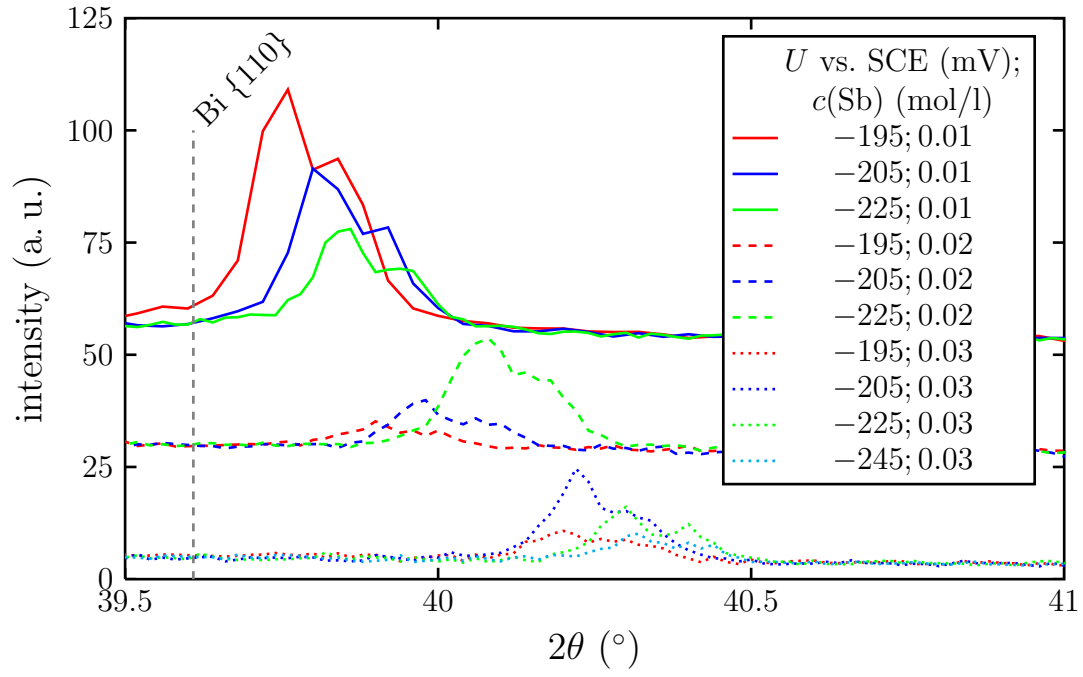
Figure 3.8: Comparison of diffraction angles of the {110} reflections of nanowire arrays ($d = 65 - 75$ nm, thickness $30\,\mu$m) for different deposition potentials and Sb concentrations.

originating from the polycarbonate matrix, and the {012} and {110} reflections of $Bi_{1-x}Sb_x$ nanowire arrays. The Au {111} reflections could coincide with the {104} reflections of $Bi_{1-x}Sb_x$ alloys. However, no {104} reflections were observed in later measurements on samples without back layer.

In Figure 3.8, the $\omega - 2\theta$ scans are shown for all three Sb concentrations and all four deposition potentials in the range from 39.5 to 40°. The {110} reflections are depicted as function of deposition conditions, U and $c(Sb)$. They shift to larger angles for larger deposition potentials. Thus, the crystalline structure of $Bi_{1-x}Sb_x$ alloy nanowires is of the same space group ($R\bar{3}m$) as their bulk counterparts.

For a quantitative analysis, the {110} reflections of $Bi_{1-x}Sb_x$ were chosen. As discussed in Chapter 1.3.1, the lattice parameters change as a function of Sb content almost following Vegard's law from $a = 4.5465$ and $c = 11.8616\,\text{Å}$ for pure Bi to $a = 4.3085$ and $c = 11.2732\,\text{Å}$ for pure Sb.[79] For each sample, the Sb concentration in the nanowires x was calculated from Equation 3.4 (Bragg's law) and Equation 1.8.

The results are summarized in Figure 3.9. x depends mainly on the Sb concentration in the electrolyte, but also, to a smaller extent, on the deposition potential U. For larger $c(Sb)$ and increasingly negative potentials, the wires become richer in Sb. The errors were derived from the β values of the peaks also giving an estimation of the width of the distribution of the Sb concentration. Thus, two complementary ways to control the composition of $Bi_{1-x}Sb_x$ nanowires were found: a "coarse tuning" by varying the electrolyte concentration and a "fine tuning" by varying the deposition potential.

To also study the influence of the wire diameter on the composition, another series of nanowires with 30 nm diameter was prepared with different $c(Sb)$ at $U = -225\,\text{mV}$ vs. SCE. For these nanowires, the {012} and {110} reflections in $\omega - 2\theta$ scans are shown in Figure 3.10. In Figure 3.11, the concentrations of Sb in arrays of nanowires with 30 nm diameter evaluated from the peak positions are shown as a function of the concentration of Sb in the electrolyte and a linear dependence of both concentrations was found. Thus, $Bi_{1-x}Sb_x$ nanowires with diameters down to 30 nm and controlled composition can be fabricated. XRD appears as suitable method to determine the average Sb concentration x in the nanowires.
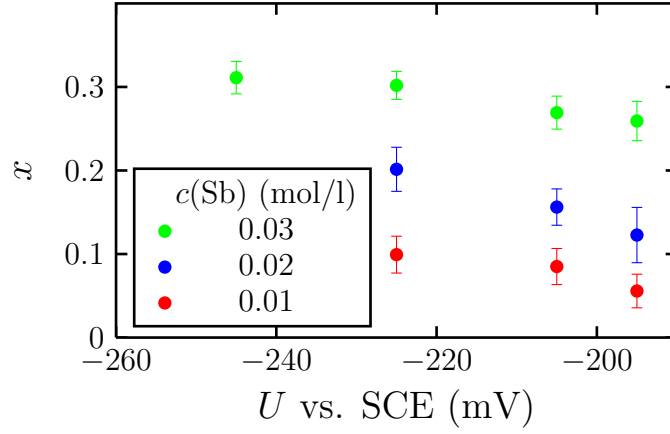
Figure 3.9: Evaluated Sb concentration x as function of Sb concentration in the electrolyte $c(Sb)$ and of deposition potential U.

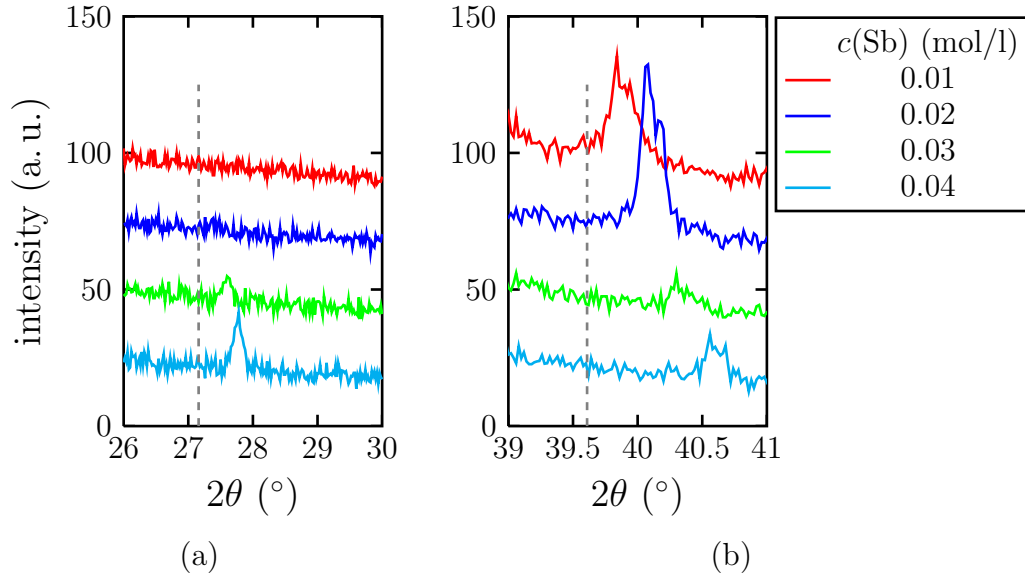Figure 3.10: $\omega - 2\theta$ scans of nanowire arrays with $30\,nm$ wire diameter deposited in $30\,\mu m$ thick PC for $U = -225\,mV$ vs. SCE and different Sb concentrations in the electrolyte $c(Sb)$. (a) {012} reflections and (b) {110} reflections. The dashed lines indicate the corresponding Bi reflections.
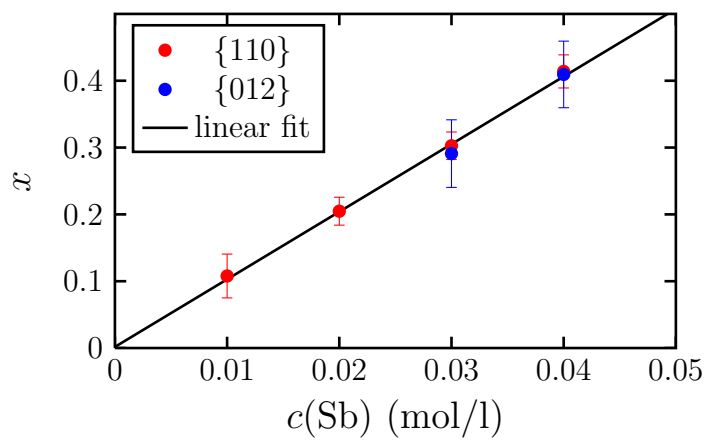
Figure 3.11: Sb concentration x as function of Sb concentration in the electrolyte $c(Sb)$ for nanowires with average diameter $30\,nm$ deposited at $U = -225$ mV vs. SCE.
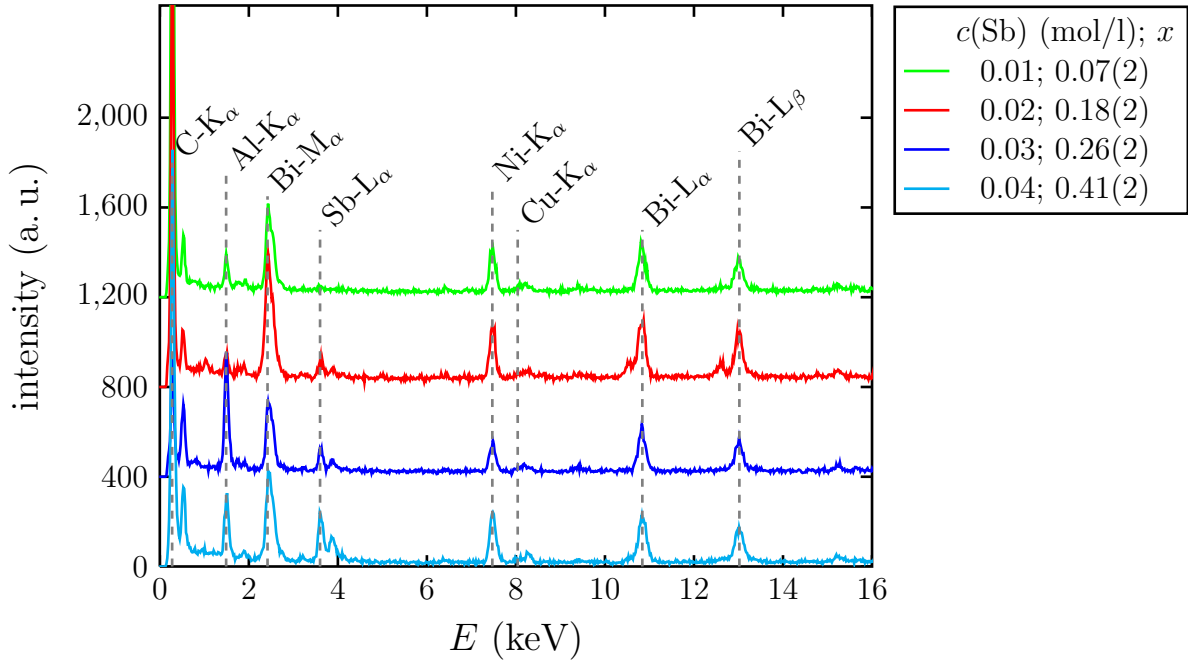
Figure 3.12: Representative TEM-EDX spectra taken of nanowires deposited from electrolytes with $c(\text{Sb}) = 0.01$, 0.02, 0.03, and $0.04\,\text{mol/l}$ at $U = -200\,\text{mV}$ vs. SCE. The resulting concentration x is also indicated.

Analysis by HR-TEM   Nanowires deposited from mixed electrolytes with different $c(\text{Sb})$ at a deposition potential $U = -200\,\text{mV}$ vs. SCE, and $20 - 30\,\text{nm}$ wire diameter were analyzed by HR-TEM. Figure 3.13 displays HR-TEM images taken of these nanowires for $c(\text{Sb}) = $ (a) 0.01, (b) 0.02, (c) 0.03, and (d) 0.04 mol/l. The d-spacings belonging to the (012) lattice planes $(3.2 - 3.3\,\text{Å})$ and to the (110) planes $(2.3\,\text{Å})$ are indicated by white lines.

In Figure 3.12, representative spectra are presented. It can be clearly seen that the intensities of the Sb-L peaks increase for increasing $c(\text{Sb})$ in the electrolyte. Ni-K peaks are attributed to signals from the TEM grid. Contaminations like Pb and Al were found in some cases and were attributed to the preparation step for TEM. After changing the procedure, no contaminations were found in later samples. Stray radiation could be excluded, since a stray aperture was used. Quantitative analysis using the Cliff-Lorimer approach led to the average concentrations 0.07, 0.18, 0.26, and 0.41, respectively. These results also show that the composition can be controlled by the deposition conditions for thinner nanowires as observed in the XRD measurements.

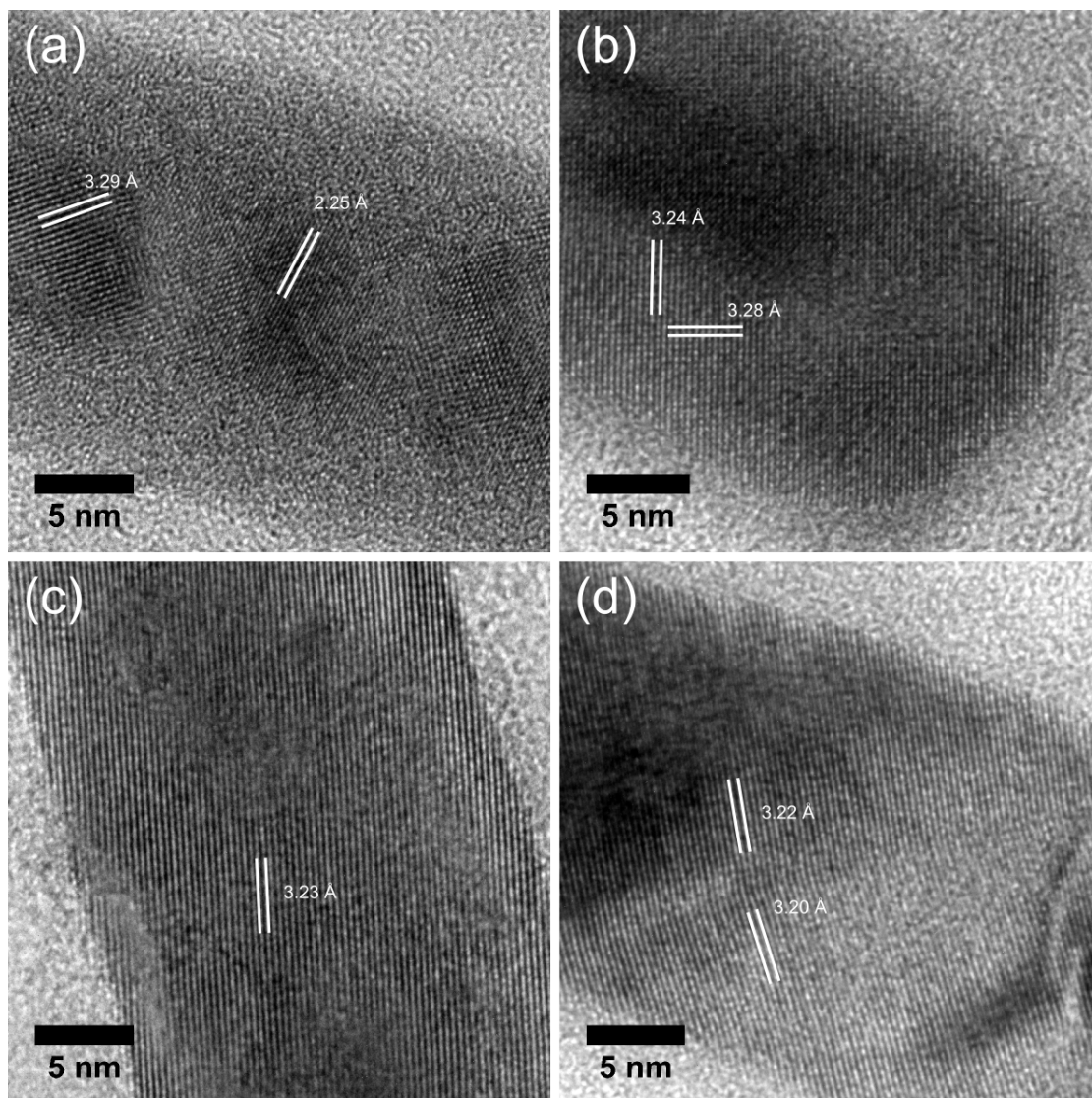Since the determination of the composition in nanowires with small diameters

61

Figure 3.13: HR-TEM images taken of $20 - 30$ nm diameter nanowires deposited from electrolytes with $c(\text{Sb}) = 0.01$, 0.02, 0.03, and 0.04 mol/l at $U = -200$ mV vs. SCE. d-spacings are given for selected grains.
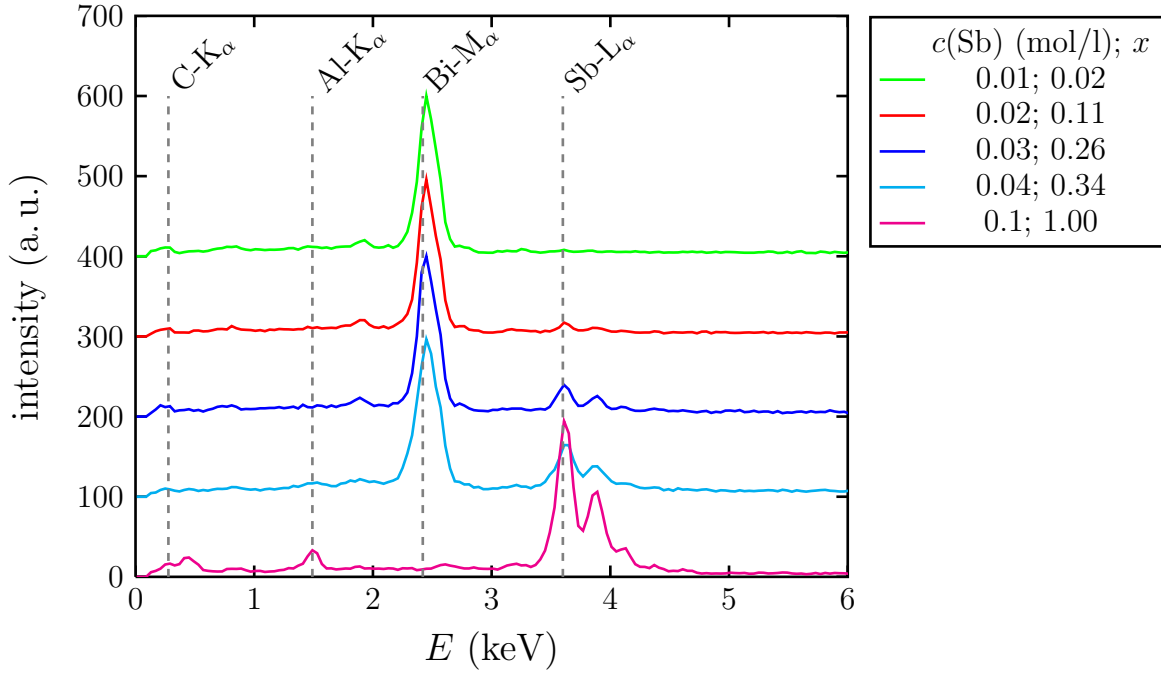
Figure 3.14: SEM-EDX spectra taken of caps on 30 nm diameter nanowires deposited from electrolytes with different $c(Sb)$ at $U = -200\,\text{mV}$ vs. SCE. (Quantification with EDAX ZAF Quant.)

by EDX is time consuming and difficult, it is tempting to use the caps grown on top of such nanowires as indicator. EDX measurements performed on caps of 30 nm diameter nanowires deposited using $U = -200\,\text{mV}$ vs. SCE and different electrolyte compositions in a Philips XL30 SEM are summarized in Figure 3.14. Compared to the resulting composition measured on nanowires by TEM-EDX (Figure 3.12), the Sb concentration was found to be significantly lower in the caps for Bi-rich alloys. This can be attributed to changes in the deposition process when the growth of the nanowires changes over to the deposition of caps.
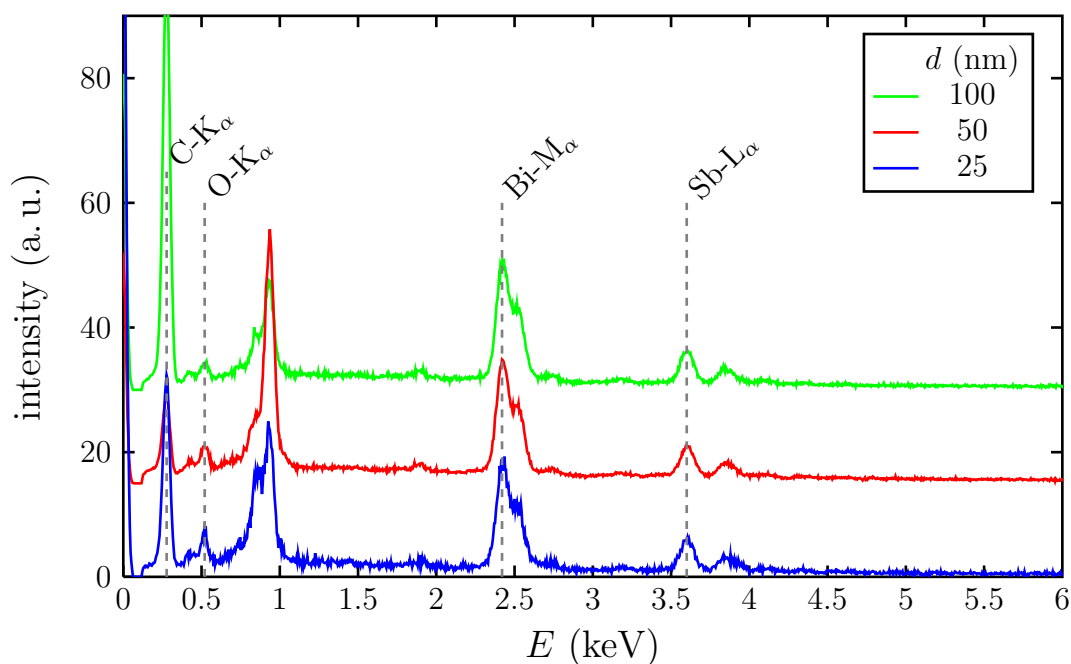
Figure 3.15: Typical SEM-EDX spectra taken of nanowires deposited from an electrolyte with $c(\mathrm{Sb}) = 0.04\,\mathrm{mol/l}$ at $U = -230\,\mathrm{mV}$ vs. SCE and different wire diameters.

Diameter Dependent Composition As discussed in Section 3.1.3, the quantitative analysis of materials with reduced size is challenging. To study the influence of the wire diameter on the composition, a series of nanowires with diameters $d = 100$, 50, and 25 nm was prepared. All samples were deposited under the same deposition conditions, $c(\mathrm{Sb}) = 0.04\,\mathrm{mol/l}$ and $U = -230\,\mathrm{mV}$ vs. SCE, and analyzed by SEM-EDX, TEM-EDX, and XRD.

As shown in Section 3.1.3, much less signal is expected for smaller nanowire samples. This is also observed in the spectra depicted in Figure 3.15. Furthermore, Ni and Cu-L lines were observed. They originated from stray radiation from the surrounding grid and a Cu cooling ring in front of the detector. O and C radiation are most likely from polymer remains at the nanowire and at the surrounding grid. In some cases, polymer rests remain attached to the nanowire and carbon deposition is observed in the form of an increasing C-K peak.

Closer looks on representative spectra and the resulting series fitting of the Esprit software for wire diameter 50 and 100 nm are depicted in Figure 3.16. For Bi and Sb, the important lines are indicated (compare with Figure 3.3) Because of the resolution of 123 eV at Mn-K_α ($\approx 5.9\,\mathrm{keV}$), which is typical of EDX devices,

not all lines are resolved. The background was subtracted manually by defining background areas in the Esprit software such that the unnormalized sum of elements is as close as possible to 100 %. At very low energies the background is not described well. This, however, does not influence the quantification using the Bi-M and Sb-L lines.

Since the statistics of EDX spectra is improved by a longer acquisition time ($\propto \sqrt{t}$), it would be best to measure as long as possible. That would require a precise drift correction for the samples, and 300 s of life time were chosen as compromise. The Bi-M and Sb-L lines are taken by the program for the determination of the concentrations, while the other lines and lines of other elements are just fitted to the spectrum. Surprisingly, the C-K and O-K lines are sometimes attributed to the Sb-M lines to a much larger amount than expected, as seen for the spectrum in Figure 3.16(b). The peak at 0.28 keV should be attributed mostly to carbon.

Figure 3.17 shows TEM-EDX spectra measured on nanowires of the same samples in the Zeiss 912Ω. For these measurements, a spot size of 32 nm was selected and counts were also acquired for 300 s. The self-calibrated system provided an average composition of $x = 0.454(9)$, $0.426(12)$, $0.427(6)$ for $d = 25$, 50, and 100 nm, respectively. Importantly, no concentration gradient along the nanowire was observed.

Tables 3.2.1, 3.2.1, and 3.4 show the composition measured by three different methods as function of the wire diameter. For EDX, the mean value $\bar{x}$ and the standard deviation were evaluated. The minimal and maximal values obtained are also included (Tables 3.2.1 and 3.2.1). For XRD, x was computed from the peak positions of the {012} and {110} reflections. The d-spacing and the error Δx derived from the FWHM values are also presented.

In Figure 3.18, the results of all methods are presented. For 50 and 100 nm wire diameter, TEM-EDX and XRD {110} have the same values within the error bars. SEM-EDX tends to provide higher values. However, the SEM-EDX system was not specially calibrated and absorption effects may also have a systematic influence on the evaluation. For 25 nm wire diameter, the error of the XRD {110} measurement may be underestimated, since the signal is very weak. For the {012} reflections, broad peaks are measured for all samples. This presumably corresponds to heterogeneities in the chemical composition which are a function of the growth direction. In addition, unlike the EDX measurements, XRD distinguishes between grains with different orientations. However, the d-spacings may be different for nanomaterials than for bulk material. Thus, a discrepancy between the methods could also be explained.
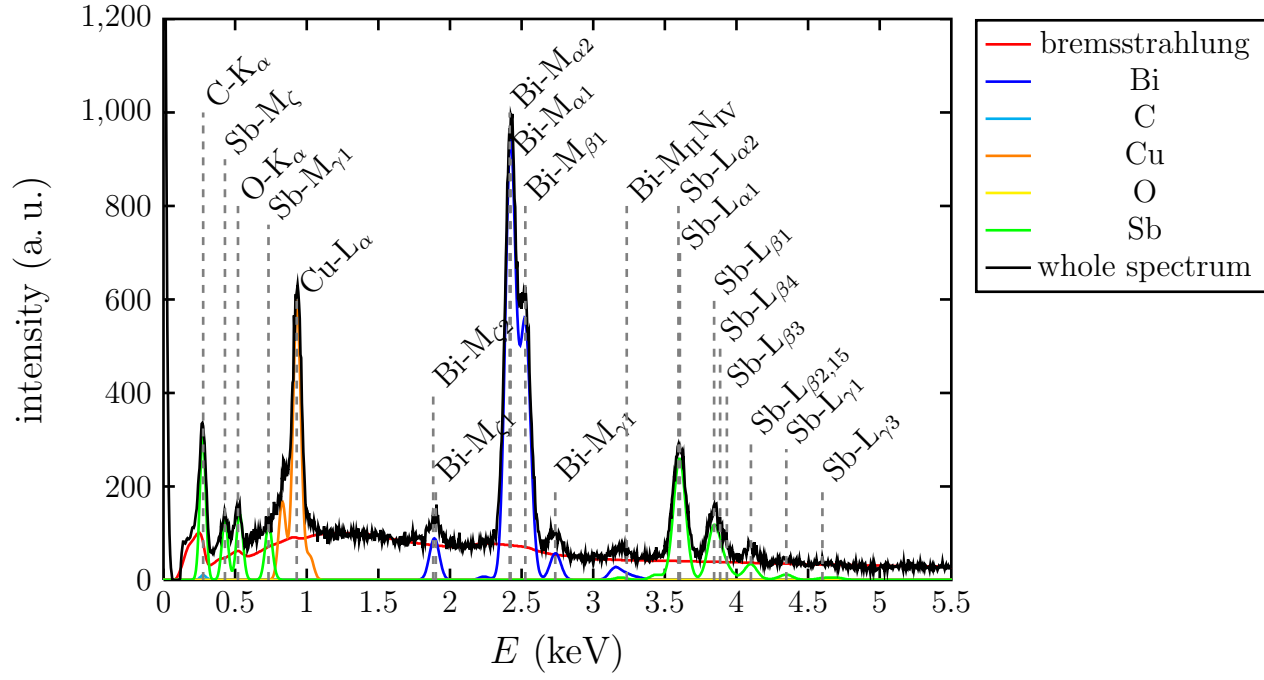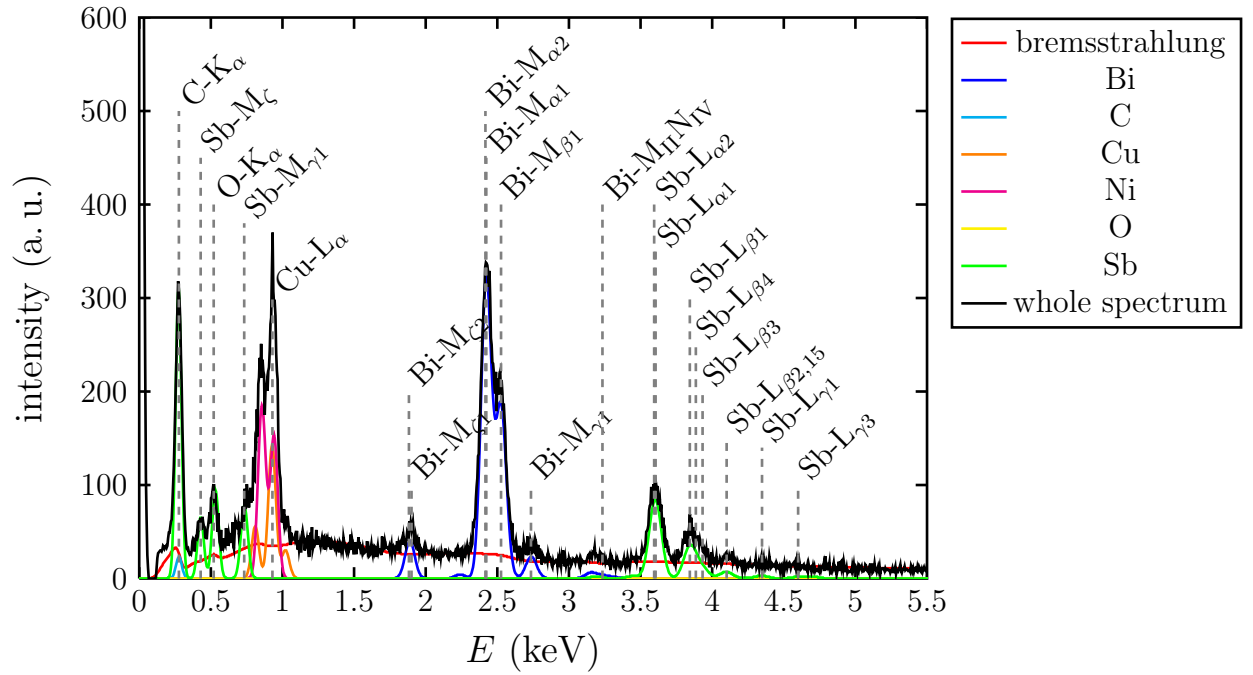
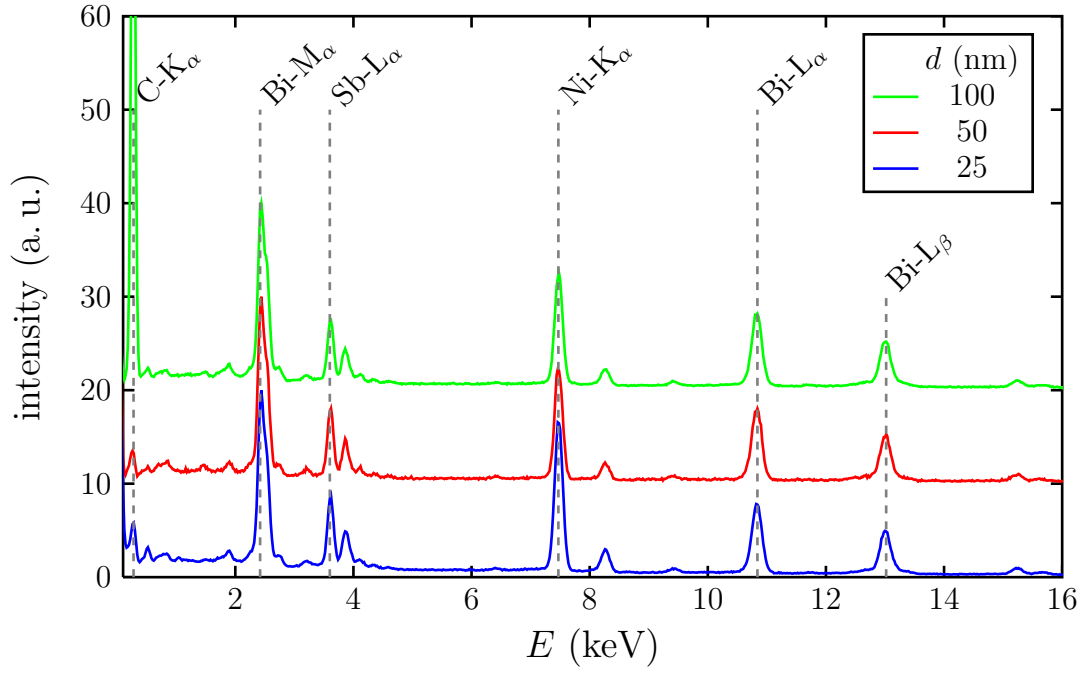Figure 3.16: SEM-EDX spectra of selected nanowires with diameters (a) 100 and (b) 25 nm.

Figure 3.17: Representative TEM-EDX spectra taken of nanowires deposited from an electrolyte with $c(\text{Sb}) = 0.04\,\text{mol/l}$ at $U = -230\,\text{mV}$ vs. SCE and different wire diameters.
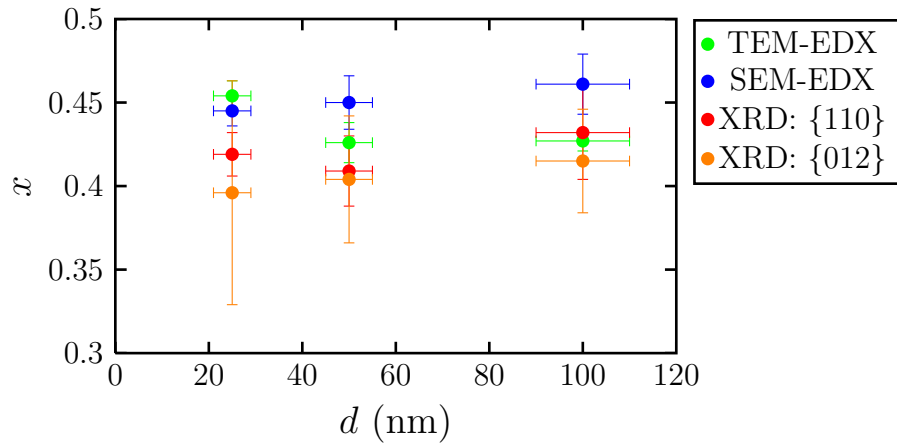

Figure 3.18: Comparison of the Sb concentration x obtained from different quantitative methods, TEM-EDX, SEM-EDX, and XRD, as function of wire diameter.

d (nm)	$\bar{x}$ (%)	σ_x (%)	$x_{\max}$ (%)	$x_{\min}$ (%)
100	42.7	0.6	43.9	41.9
50	42.6	1.2	44.3	41.1
25	45.4	0.9	46.7	44.3

Table 3.2: Results of TEM-EDX measurements performed on several individual nanowires and at various positions as a function of mean wire diameter d. The concentrations were evaluated with self-calibrated Cliff-Lorimer coefficients.

d (nm)	$\bar{x}$ (%)	σ_x (%)	$x_{\max}$ (%)	$x_{\min}$ (%)
100	46.1	1.8	48.1	44.2
50	45.0	1.6	48.3	42.0
25	44.5	0.9	45.1	43.0

Table 3.3: Results of SEM-EDX measurements. The concentrations were evaluated with the proprietary software Esprit 1.8 by Bruker.

$\{hkl\}$	$d = 100$ nm			$d = 50$ nm			$d = 25$ nm		
	d_{hkl} (Å)	x	Δx	d_{hkl} (Å)	x	Δx	d_{hkl} (Å)	x	Δx
$\{012\}$	3.211	0.415	0.031	3.213	0.404	0.038	3.213	0.396	0.067
$\{110\}$	2.220	0.432	0.028	2.223	0.409	0.021	2.222	0.419	0.013
$\{113\}$	1.929	0.418	0.026	–	–	–	–	–	–
$\{202\}$	1.827	0.425	0.017	–	–	–	–	–	–
$\{024\}$	1.606	0.410	0.026	1.607	0.402	0.020	–	–	–
$\{122\}$	1.411	0.425	0.024	1.413	0.400	0.037	–	–	–
$\{214\}$	1.302	0.412	0.039	–	–	–	–	–	–

Table 3.4: Results of XRD measurements performed on nanowire arrays, embedded in a PC matrix, as a function of mean wire diameter d.

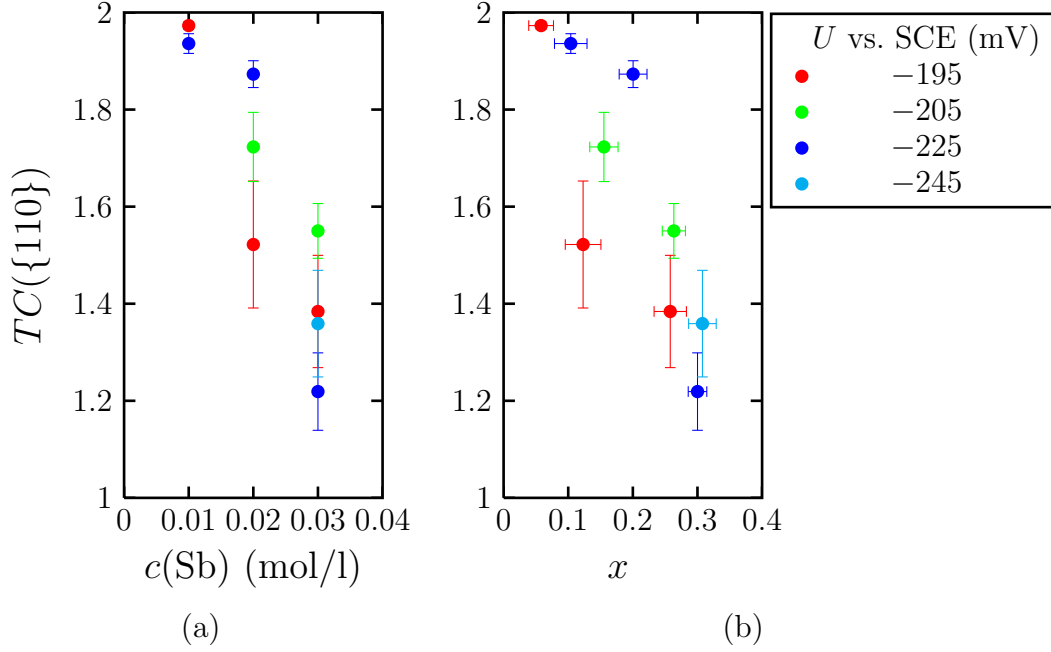Figure 3.19: Texture coefficients for {110} reflections of nanowires ($d = 65-75\,\text{nm}$) deposited at different potentials and different electrolyte concentrations as functions of (a) $c(\text{Sb})$ and (b) x.

Crystalline Structure As discussed above, nanowire arrays were deposited using electrolytes with $c(\text{Sb}) = 0.01$, 0.02, and 0.03 mol/l, deposition potentials of -195, -205, -225, and $-245\,\text{mV}$ vs. SCE and diameters of $\sim 70\,\text{nm}$ and $\omega - 2\theta$ scans were recorded for each sample. Since the back electrode was still attached, mostly only two reflections ({110} and {012}) were observed. For these samples with $n = 2$, the intensities of the reflections have been evaluated to study the texture of the nanowires as a function of $c(\text{Sb})$ and U via Equation 3.9. Figure 3.19(a) shows the influence on the texture coefficient of {110} as function of electrolyte composition $c(\text{Sb})$, and in Figure 3.19(b) the same data is presented as function of the respective x values obtained from the peak position. In general, there is a decrease in the $TC(\{110\})$ for increasing Sb concentration.

In order to investigate the texture coefficient as a function of wire diameter, two series with $d = 25$, 50, and 100 nm were prepared using two electrolytes with $c(\text{Sb}) = 0.04$ and 0.1 mol/l. Figure 3.20 displays the diffractograms recorded for each sample. In this case, the Au layer was dissolved. The diffractograms show less reflections with decreasing wire diameter, probably due to a worse signal-to-noise ratio. All pure Sb nanowires and $Bi_{1-x}Sb_x$ nanowires with 50 and 100 nm
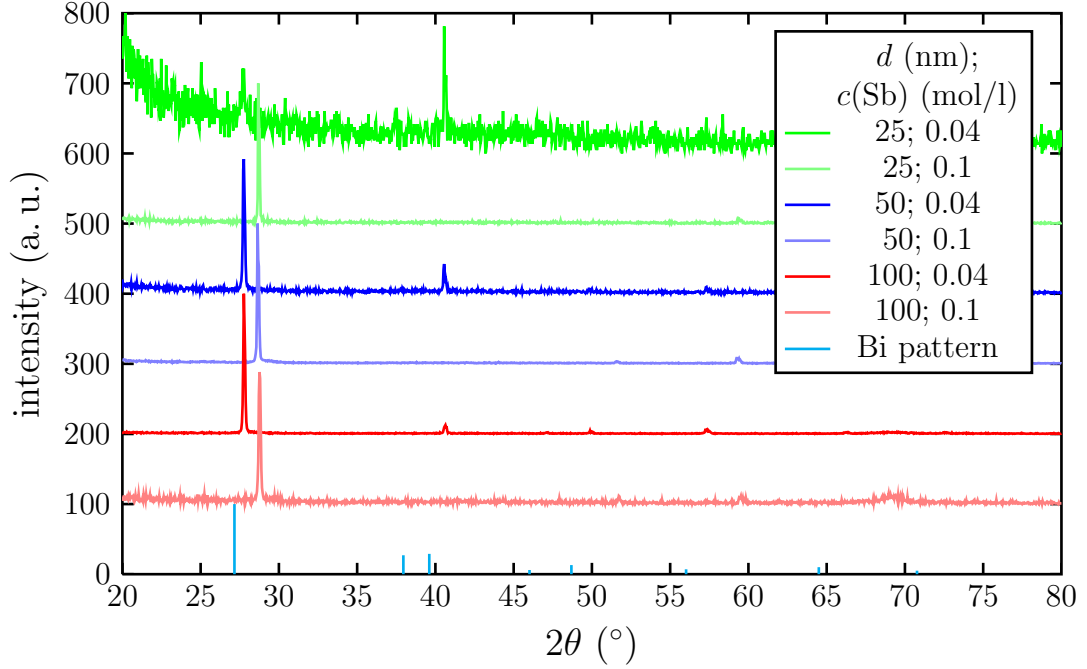
Figure 3.20: X-Ray diffractograms of nanowire arrays deposited with $c(\mathrm{Sb}) = 0.04$ and $0.1 \, \mathrm{mol}$ and different wire diameters.

wire diameter display a strong $\{012\}$ texture. For $\mathrm{Bi}_{1-x}\mathrm{Sb}_x$ nanowires, the $\{110\}$ reflection becomes stronger with respect to the $\{012\}$ reflection for smaller wire diameter.

In addition, individual nanowires of this series were also characterized by dark field (DF) and bright field (BF) imaging in TEM (compare Figures 3.21–3.23). The color of the DF images and the diffractions patterns (DP) were inverted, and the DP were rotated to fit to the corresponding BF images. In the BF images, the normals to the respective lattice planes are indicated by blue lines for comparison with the wire axis.

For a 25 nm diameter nanowire, BF images were taken along the wire (Figure 3.21). At several positions, DP were also taken. Two of these are shown in Figure 3.21. DF imaging along the wire using the (012) reflection revealed a polycrystalline structure. Both short and long crystallites are seen.

Figure 3.22 displays from left to right BF and DF images and the corresponding diffraction pattern (DP) of a 50 nm diameter $\mathrm{Bi}_{1-x}\mathrm{Sb}_x$ wire ($x \approx 0.43$). For the DF image, the (012) reflection was selected, and a long, continuous crystallite is seen. Also, images of a thicker wire with 100 nm diameter were taken as shown in Figure 3.23. DP taken along the wire do not change over several µm. At the end

of the wire (right hand side), several probably smaller crystallites contributed to the patterns.

This TEM analysis shows that the nanowires are polycrystalline with crystallite sizes typically of the order of 100 nm in length for all wire diameters.
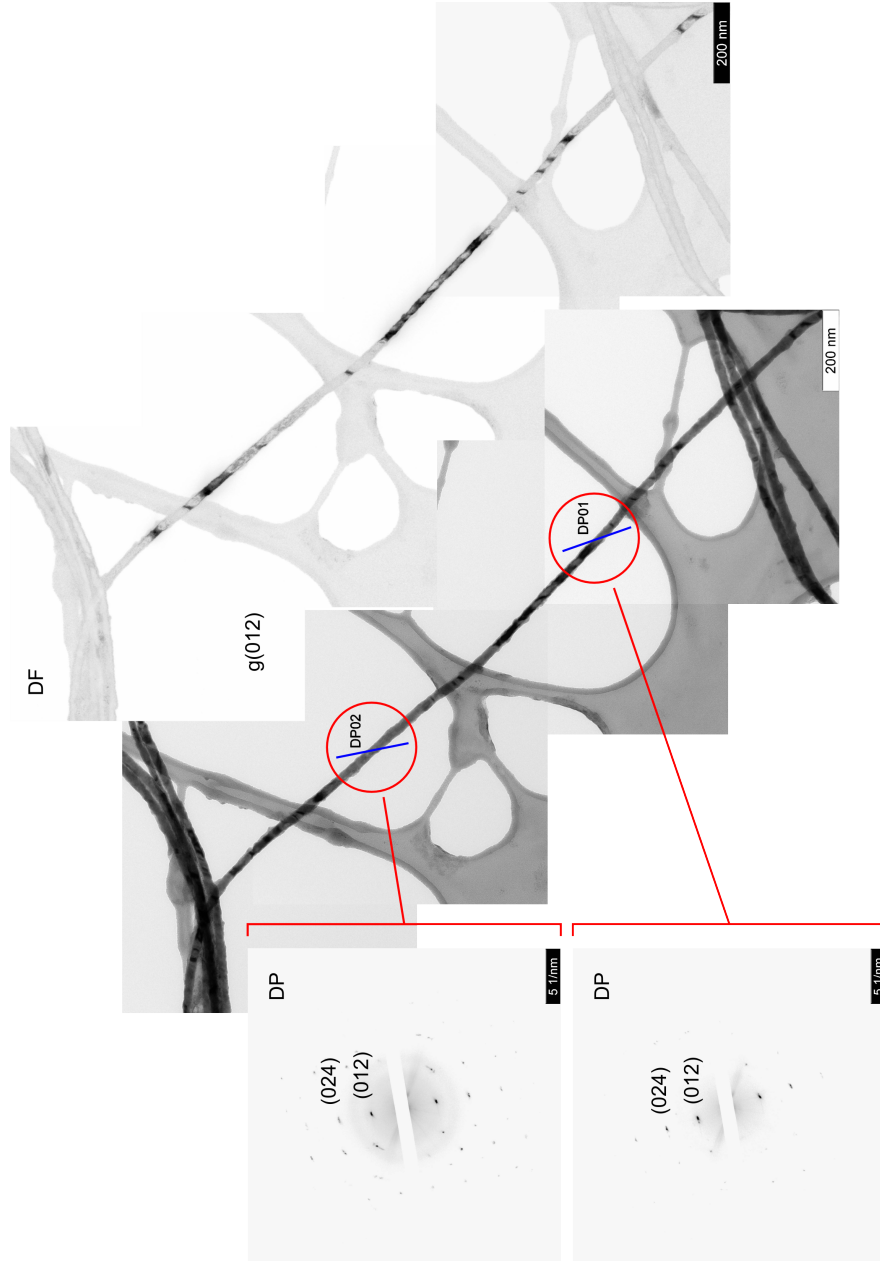
Figure 3.21: TEM image of a $Bi_{1-x}Sb_x$ ($x \approx 0.45$) nanowire with $d = 25\,\text{nm}$ at a magnification of 32k. Diffraction patterns taken at two selected areas of the nanowire (left), bright field images (middle), and dark field images using (012) reflections (right). A blue line indicates the normal to (012) planes.
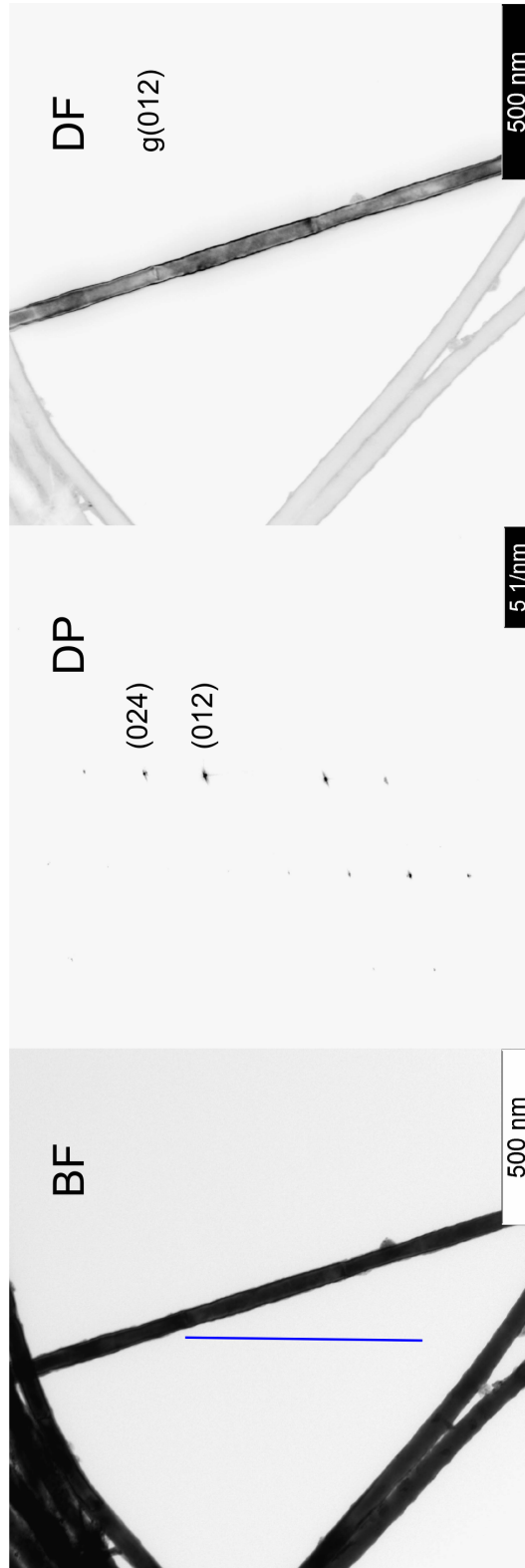
Figure 3.22: TEM images of a $Bi_{1-x}Sb_x$ nanowire with $d = 50\,\mathrm{nm}$ and $x \approx 0.43$. BF at 16k magnification (left), diffraction pattern (middle), and DF (right) using the (012) reflection. The blue line marks the normal to (012) lattice planes.
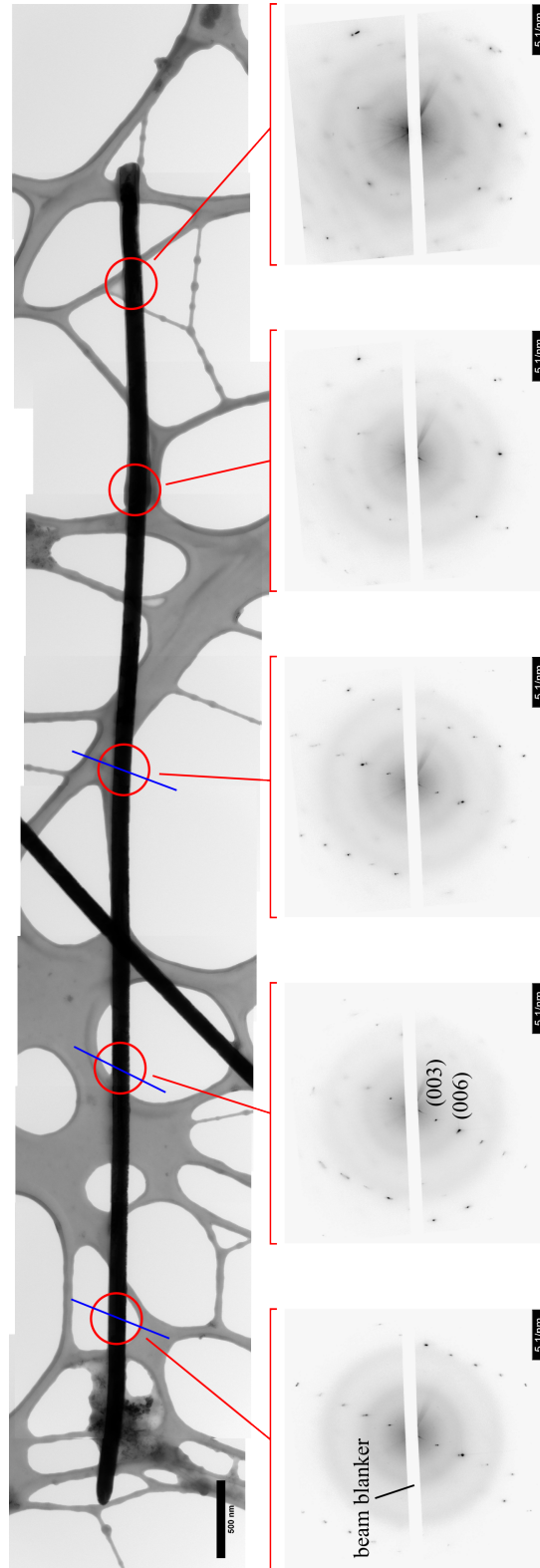
Figure 3.23: TEM BF images of a $Bi_{1-x}Sb_x$ nanowire with $d = 100\,\mathrm{nm}$ and $x \approx 0.43$ and diffraction patterns along the wire. The (003) and (006) reflections are indicated in one pattern. Red circles mark the selected area and blue lines are normals to the (00l) planes.

For stress and strain analysis, the FHWM β of diffractograms taken of nanowire arrays with wire diameters 50 and 100 nm, respectively, were evaluated. In Figure 3.24, the corresponding Williamson-Hall plots are shown for Lorentzian and Gaussian peak form deconvolution. There is no obvious connection between the β and the θ values to evaluate either ϵ or τ. As a conclusion, crystallites may have different growth conditions for different growth directions. It cannot be excluded that the broadening is because of anisotropic strain and dislocations, but the main contribution to the peak broadening is probably mostly due to chemical heterogeneities. A detailed analysis with the modified Williamson-Hall method by Ungár[141] or the Warren-Averbach method[142] using FFT analysis would require a much better resolution of the peaks, e. g. with synchrotron radiation.
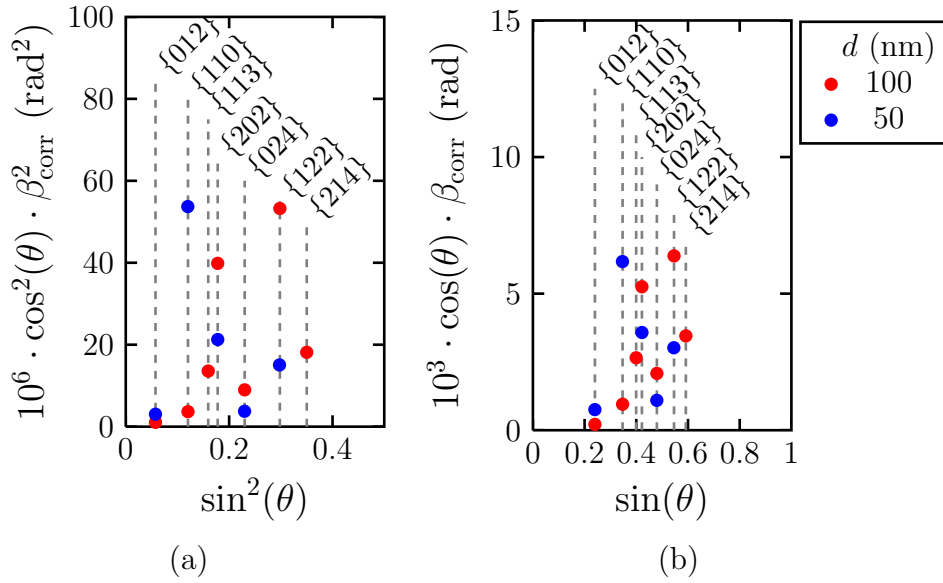

Figure 3.24: Williamson-Hall plots for nanowire arrays with diameters 50 and 100 nm. Deconvolution for (a) Gaussian and (b) Lorentzian peak shape.
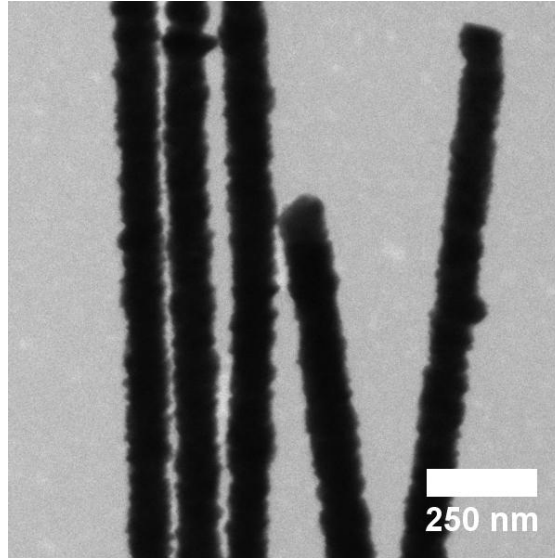
Figure 3.25: SEM micrograph of several 90 nm diameter nanowires grown in ion-track etched PET ($x \approx 0.15$).

3.2.2 Rough Nanowires Deposited in PET Membranes

As discussed in Chapter 2.1, PET has different properties than PC, and thus, the deposition of nanowires in the channels of the template might also differ and result in nanowires with deviating crystallinity and composition. In Figure 3.25, a micrograph of nanowires grown in ion-track etched PET membranes is depicted. The surface roughness can be seen and may originate from inhomogeneous etching rates in the partly crystalline PET.

Nanowires were deposited in PC and PET membranes with similar channel diameter and channel density under equal deposition conditions. By studying the nanowire morphology, composition, and crystallinity, the influence on the template material was investigated.

Crystalline Structure In Figure 3.26, diffractograms are shown for nanowire arrays deposited with $c(\text{Sb}) = 0.04$ and 0.1 mol/l for wire diameters 25, 50, and 100 nm. The line positions given are taken from a Sb powder standard (JCPDS-35-732). The crystallinity of the PET foil was seen in the X-ray diffractograms. Intense, broad reflections were observed at $2\theta \approx 25.9$ and 53.7° which were attributed mainly to PET {100} and PET {200} reflections. The unit cell of PET is triclinic with $a = 4.56$, $b = 5.94$, $c = 10.75$ Å and $\alpha = 98.5$, $\beta = 118$, and $\gamma = 112°$.[143,144] Before the measurement, the Au back layer was removed. The
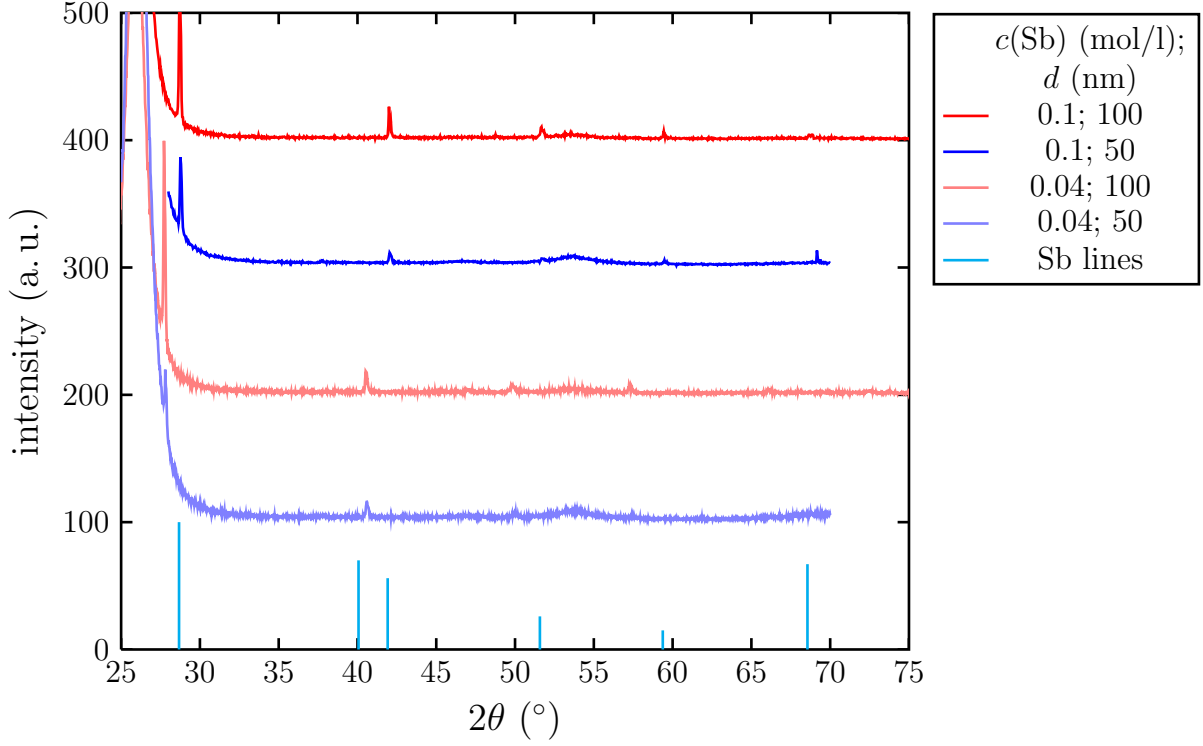
Figure 3.26: X-Ray diffractograms of nanowires deposited in PET membranes with $c(\mathrm{Sb}) = 0.04$ and $0.1\,\mathrm{mol/l}$ and $U = -230\,\mathrm{mV}$ vs. SCE. Sb lines were selected from JCPDS-35-732.

diffractograms of $Bi_{0.6}Sb_{0.4}$ and Sb nanowires revealed a {012} texture in all cases. However, for the samples with smaller wire diameters $d = 50\,\mathrm{nm}$, the {012} texture was less pronounced and in the alloy only slightly stronger than the {110} texture. Again, no {104} reflections, which were almost as strong as the {110} reflections in polycrystalline powder, were observed for all samples.

To investigate the roughness of nanowires deposited in PET with HR-TEM, alloy nanowires with a Sb concentration $x \approx 0.15$ and average diameter $20\,\mathrm{nm}$ were prepared at $U = -220\,\mathrm{mV}$ vs. SCE. In Figure 3.27, the resulting images are depicted at lower magnification in (a) and high resolution in (b–d). The wires where mostly aligned such that (012) lattice planes were observed. As a result, the length of the crystallites is larger than the average diameter of the nanowires in spite of the roughness of the nanochannels. In thin nanowires, the diameter displays a variation of up to $30\,\%$.
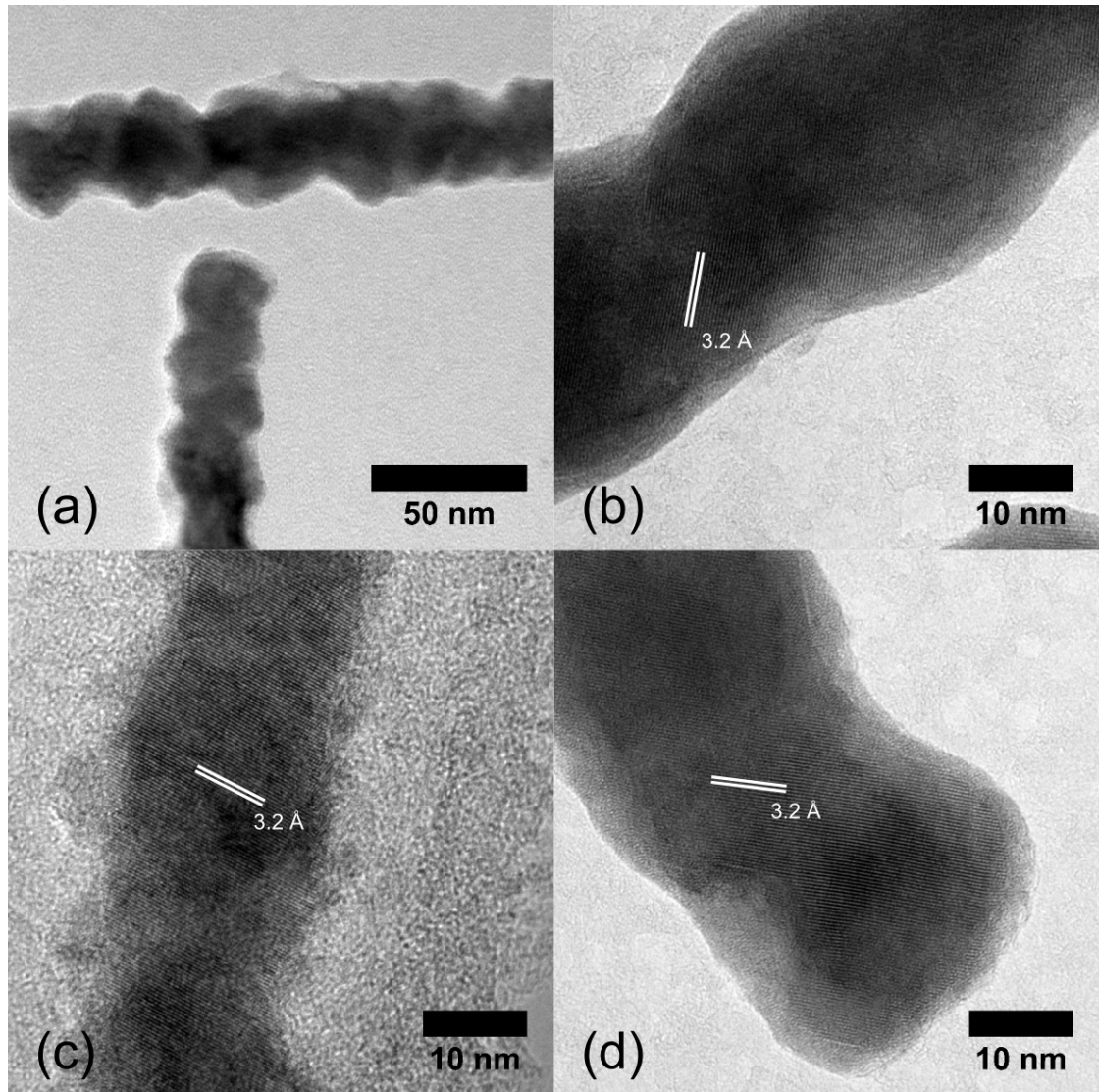
Figure 3.27: HR-TEM images of individual $Bi_{1-x}Sb_x$ nanowires with an average diameter of 20 nm deposited in a PET membrane. (a) Overview micrograph at lower magnification. (b–d) High resolution images of an individual nanowire. *d*-spacings of the (012) lattice planes are indicated by white lines.
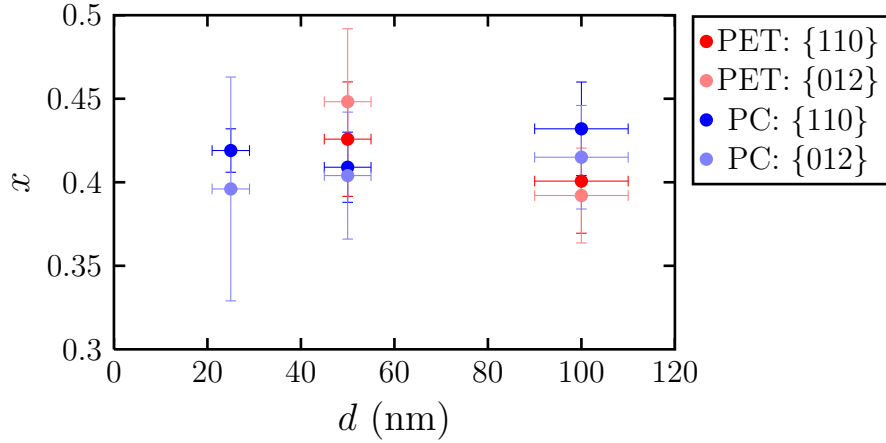
Figure 3.28: Comparison of the composition obtained by XRD of nanowires deposited in PC and PET membranes for different wire diameters, $c(\mathrm{Sb}) = 0.04\,\mathrm{mol/l}$, and $U = -230\,\mathrm{mV}$ vs. SCE.

Composition In Figure 3.28, the results of the compositional analysis by XRD are compared to the results obtained for nanowires deposited in PC membranes for $c(\mathrm{Sb}) = 0.04$ mol/l, $U = -230\,\mathrm{mV}$ vs. SCE, and different wire diameters. However, the PET membrane thicknesses were $36\,\mathrm{\mu m}$ for $d = 100\,\mathrm{nm}$ and $12\,\mathrm{\mu m}$ for $d = 50\,\mathrm{nm}$, instead of $30\,\mathrm{\mu m}$ as for the PC templates. Within the error bars the concentrations are found to be identical for the {110} reflection.

Williamson-Hall plots for the diffractograms in Figure 3.26 are shown in Figure 3.29. As for the nanowires grown in PC, no linear dependence is found which could indicate anisotropic stress or chemical heterogeneities.

Figure 3.29: Williamson Hall plots for nanowire arrays deposited at $U = -230\,\text{mV}$ vs. SCE with $c(\text{Sb}) = 0.04$ and $0.1\,\text{mol/l}$ in PET for different wire diameters. Deconvolution for (a) Gaussian and (b) Lorentzian peak shape.
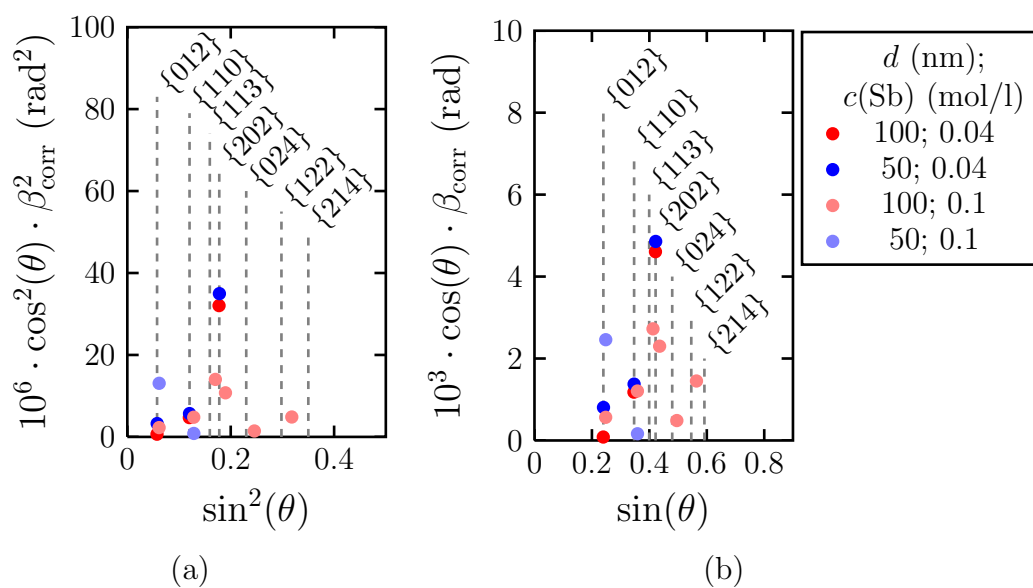
3.3 Nanowires Deposited Using Pulsed Potential

In order to contact nanowire arrays electrically and implement nanowires into microsystems, it is important that all nanowires grow at the same rate. Pulsed electrodeposition has been reported to result in a homogeneous growth of the nanowires.[115] Thus, arrays were prepared by PC membranes of 30 µm thickness under the deposition conditions presented in Section 2.2.3. Then, the nanowires were characterized by SEM-EDX and TEM.

Composition For nanowires prepared by pulsed deposition and $c(Sb) = 0.01$, 0.02, and 0.03 mol/l, EDX measurements were performed to analyze the composition. The results are presented in Table 3.5. The composition of the nanowires was also controlled by the choice of $c(Sb)$. However, for the sample with $c(Sb) = 0.02$ mol/l, the resulting Sb concentration x was lower than expected. Furthermore, the difference between minimum and maximum value seemed to be larger for these samples than for samples prepared potentiostatically (compare Table 3.2.1).

The Bruker EDX system allows one to create a mapping to visualize the distribution of elements in the sample which is useful in order to investigate the homogeneity of the nanowires. In Figure 3.30, an SEM image of several nanowires is depicted and the intensities of Bi-M_α and Sb-L_α are represented by color maps.

This, however, is a demanding task for the drift correction. As a consequence, data acquisition is only possible up to about half an hour under optimal conditions. A better compromise of EDX statistics and elemental distribution is offered by the line scan mode. Here, the evolution of the composition is directly measured along a section of several µm of a nanowire as shown in Figure 3.31. Figure 3.31(a) shows an SEM image in the inset indicating the line chosen for analysis and the resulting cumulative spectrum for all points on this line. In Figure 3.31(b), the intensities of Bi-M_α and Sb-L_α are plotted as function of the position. At about 2 µm, the intensities increase because a second wire crosses. These measurements

$c(Sb)$ (mol/l)	$\bar{x}$ (%)	σ_x (%)	$x_{\max}$ (%)	$x_{\min}$ (%)
0.01	11.3	1.5	13.3	9.0
0.02	15.1	2.0	17.9	10.9
0.03	32.1	2.7	35.7	25.5

Table 3.5: Results of SEM-EDX measurements of nanowires with $d \approx 70$ nm deposited by pulsed electrodeposition. The concentrations were evaluated with the proprietary software Esprit 1.8 by Bruker.
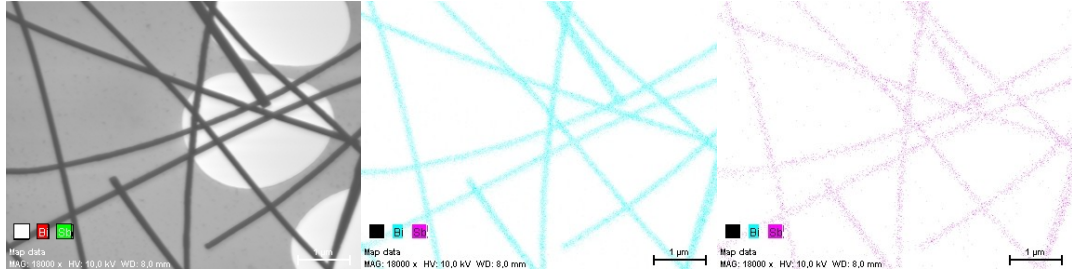
Figure 3.30: SEM-EDX mapping for $Bi_{85}Sb_{15}$ nanowires with $d \approx 70\,nm$ on TEM grid: SEM image (left), Bi distribution from Bi-M_α intensity (middle), Sb distribution from Sb-L_α intensity (right).

show that the nanowires possess no large chemical heterogeneities.

Crystalline Properties   For the analysis of the grain sizes of the nanowires deposited with $c(Sb) = 0.01\,mol/l$ Sb, over 250 DF images were taken at slightly different angles, up to a tilting of at most $30\,mrad$. Then, the difference in contrast indicated grain boundaries in the nanowires. In Figure 3.32, these are marked by red lines. Some nanowires did not seem to have grain boundaries at all along the parts analyzed (black arrows). The average grain size derived from these measurements was $50 - 100\,nm$. If all channels are filled in about $1600\,s$ with pulses repeating every $120\,ms$, the wire should grow by about $2\,nm$ per cycle which is lower than the grain length found in this case. Therefore, it is not yet clear whether the pulses were responsible for a formation of grain boundaries. However, the distances found between grain boundaries seemed to be very uniform (Figure 3.32).

Homogeneity   For some samples, the deposition process was continued until caps form on top of the nanowire arrays. Instead of some scattered caps over the sample as obtained for the potentiostatic deposition, the caps formed more uniformly for the pulsed deposition. Then a Au layer was sputtered on top of the sample and the resistance was measured. Indeed, it was reduced from typically $100 - 1000\,\Omega$ down to $\sim 1\,\Omega$ and less.

3.4 Conclusion

Bi, Sb, and Bi-rich $Bi_{1-x}Sb_x$ nanowires with diameters 20 to $200\,nm$ were successfully prepared. The composition of the alloy nanowires was analyzed as function of the deposition parameters, $c(Sb)$ and U, and the wire diameter. For a control

(a)

(b)
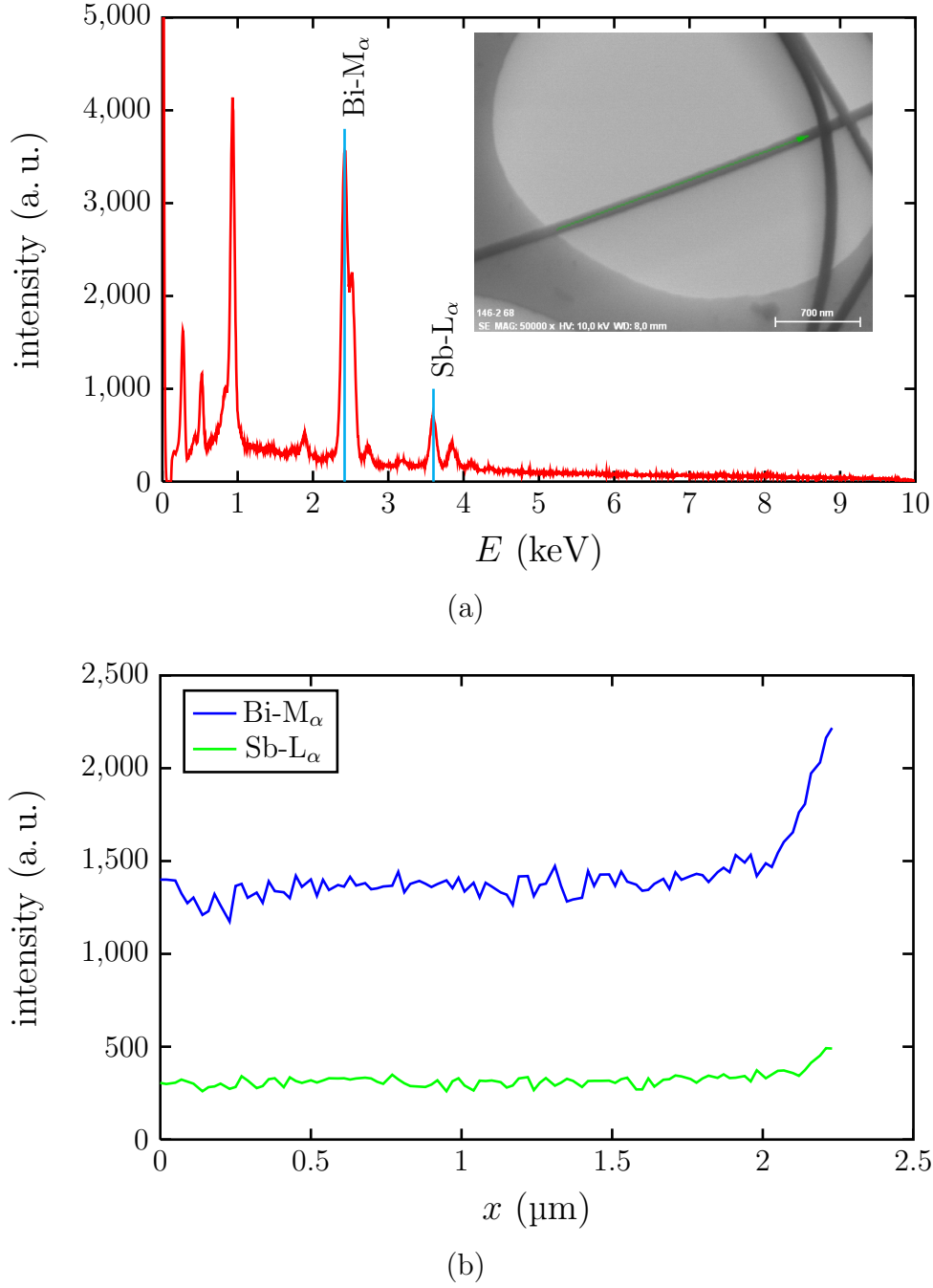
Figure 3.31: SEM-EDX linescan for a $Bi_{68}Sb_{32}$ nanowire with $d \approx 70\,\text{nm}$ on TEM grid. (a) Cumulative sum spectrum along a line (green arrow in the inset SEM image) on the nanowire and (b) intensities of Bi-M_α and Sb-L_α lines along the same line.
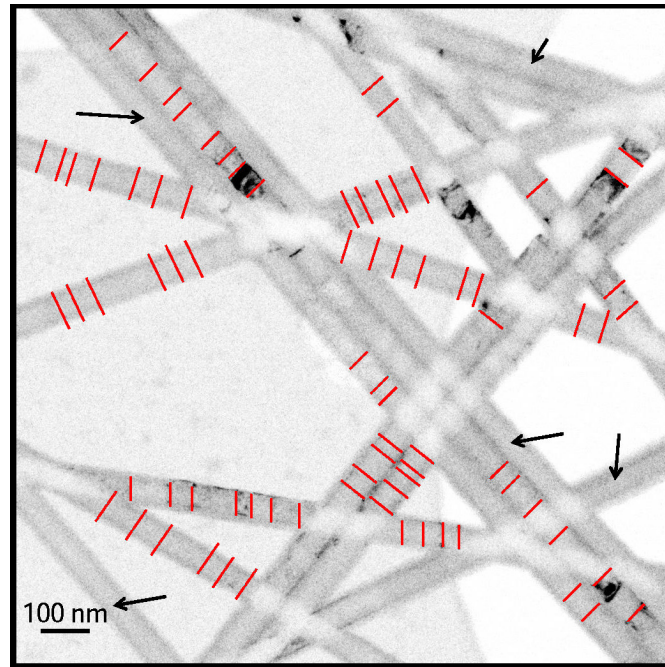
Figure 3.32: Positions of possible grain boundaries of several nanowires (red lines) obtained from a series of over 250 DF images. Wires without observed grain boundaries are indicated by black arrows.

over the composition, the electrolytes presented in the previous chapter were suitable. Furthermore, the choice of the deposition potential had also a small influence on the composition. From diffraction peak positions in $\omega - 2\theta$ scans, the mean compositions of the arrays were deduced. It was shown that the nanowires have a preferred orientation perpendicular to {110} lattice planes for bismuth-rich alloys. For an increasing Sb content, the {110} texture is decreasing. Sb nanowires exhibit a strong {012} texture.

Measurements using HR-TEM and DF imaging revealed that the crystallite size is on average of the order of 100 nm. Thus, the peak broadening in XRD may not be largely influenced by the crystallite size, and the peak broadening gives probably information about the width of the uncertainty of x for the quantification by XRD.

Using PET as template, nanowires with an enhanced surface roughness were fabricated. This is an interesting parameter, since an enhanced phonon scattering at the surface may decrease the thermal conductivity. For these rough nanowires, crystallites are typically longer than the wire diameter. Composition and the average wire diameter can be adjusted in the same ranges like for the smooth nanowires.

By pulsed electrodeposition, a more uniform growth process was attained. The nanowires were also polycrystalline and the composition could be adjusted by the composition of the electrolyte. First nanowires analyzed quantitatively exhibit variations in x larger than for nanowires deposited potentiostatically. Further experiments varying the pulse lengths may be performed, to confirm whether the pulses produce grain boundaries and to optimize the stoichiometry. If, however, equidistant grain boundaries could be enforced by pulsed deposition, this technique could be employed to systematically study the model of Mayadas and Shatzkes for $Bi_{1-x}Sb_x$ nanowires (see Section 1.4.1).

4 Seebeck Coefficient of $\mathbf{Bi_{1-x}Sb_x}$ Nanowire Arrays

symbol	quantity
U, R, I	voltage, resistance, current
r	thermal resistance
T	absolute temperature
S	Seebeck coefficient

In this chapter, the setup developed to measure the Seebeck coefficient of embedded nanowire arrays is presented. First results of S and R obtained for nanowire arrays of Bi, Sb, $Bi_{1-x}Sb_x$, and Bi_2Te_3 with wire diameters of $25 - 200\,nm$ will be shown for the temperature range from 30 to $300\,K$.

4.1 Setup

Devices The setup for the measurement of S and R consisted of a cryostat with a helium evaporation cooler COOLPAK 6000, a temperature controller LTC60 by Leybold, a cooling finger mounted inside a vacuum chamber, a pre-vacuum and a turbomolecular pump, a Keithley 2184A nanovoltmeter, a Keithley 2400 sourcemeter, and a temperature controller M9700 by Scientific Instruments.

In Figure 4.1(a), a schematic of the sample holder is shown, and Figure 4.1(b) displays a photograph of the holder mounted inside the vacuum chamber. The membrane with the embedded nanowires was placed between two copper plates onto which Si diodes and gold-plated contact pins were attached. Then, these copper plates were embedded in a stainless steel frame which is mounted onto the cooling finger. The Si diodes provided T_A, the temperature near to the cooling finger, and T_B, the temperature of the upper copper part. Thin layers of indium made for a good thermal contact of the diodes to the copper blocks. In order to insulate and isolate top and bottom parts, the frame was held together by nylon screws. The leads to the contacts and the sensors were made of non-magnetic phosphor bronze (by LakeShore) because of its low thermal conductivity and Seebeck coefficient over the whole temperature range ($< 1\,\mu V/K$).[145]

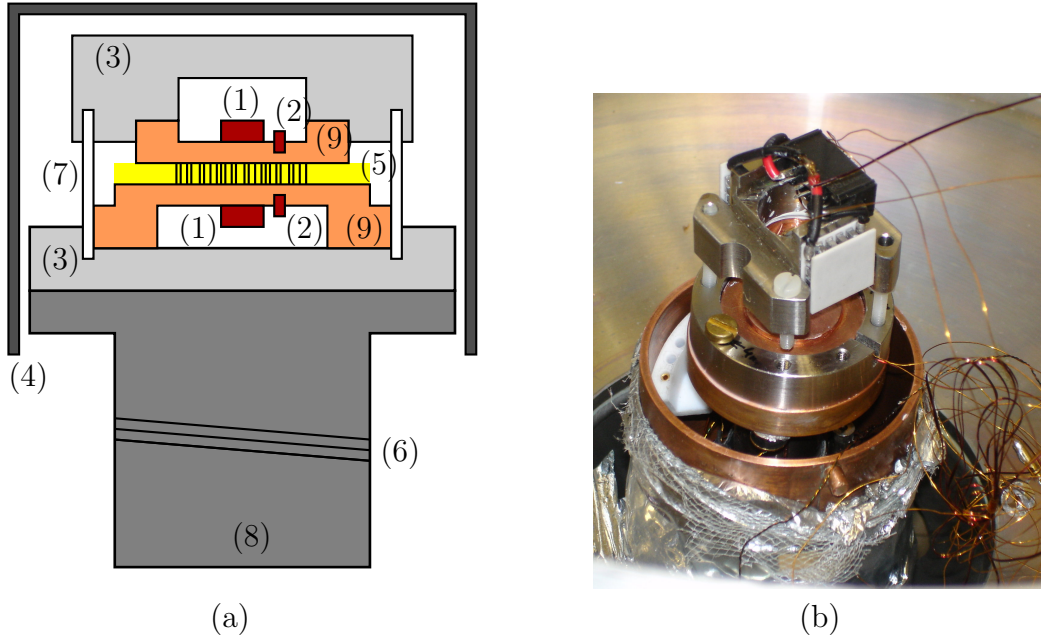(a)   (b)

Figure 4.1: Setup for the measurement of the Seebeck coefficient: (1) Si diodes, (2) contacts, (3) stainless steel frame, (4) shielding, (5) sample with nanowires, (6) heater, (7) nylon screws, (8) cooling finger, (9) copper blocks. (a) Schematic and (b) photograph of the sample holder.
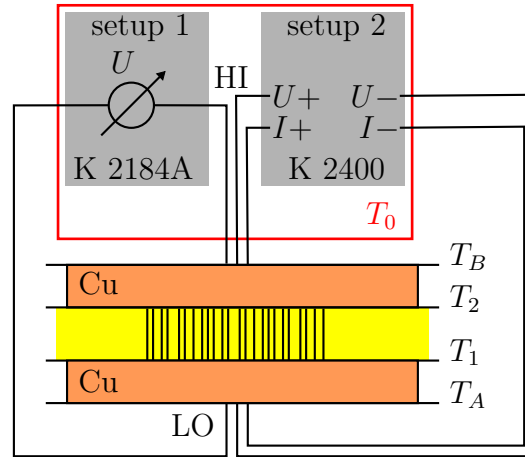

Figure 4.2: Schematic of contacting, devices, and temperatures.

The connections of the sourcemeter and the nanovoltmeter to the sample are shown in Figure 4.2. For the measurement of the voltage at the sample at zero current, the nanovoltmeter was employed, whereas additional $I - U$ curves were obtained with the sourcemeter. In this case, the maximum current $I_{\max}$ was selected, and a sweep from $-I_{\max}$ to $I_{\max}$ was performed to have minimum Joule heating and heat transfer by the Peltier effect, and at the same time, best accuracy for voltage measurement.

The general equation for both kinds of measurement is given by

$$U = RI + S\Delta T. \tag{4.1}$$

Using this equation, the resistance R can be obtained from the slope of the $I - U$ curve, and in principle, the Seebeck coefficient can be determined from the intercept with the U axis. However, the error of the Keithley 2400 is 0.012% of the reading plus a constant value of $300\,\mu V$ in the lowest range, which is not sufficient for measuring the thermovoltage obtained at low temperature differences. Therefore, the Keithley 2184A was employed. For this device the error is only 10^{-6} of the reading plus $10\,nV$.

The cryostat is able to cool the sample down to temperatures as low as $20\,K$. The set-point of the LTC60 heating device is changed only every $60 - 120\,\min$ in steps of $30\,K$. Furthermore, the LTC60 is programmed to produce oscillations in the temperature T_A. T_B follows only slowly, because the upper copper block is thermally separated from the bottom copper block by the polymeric matrix with the nanowires and the nylon screws. These temperature oscillations had a period of about $10\,\min$. Ideally, the voltage measurements followed a straight line in a U-ΔT graph for each set-point. Then, the Seebeck coefficient was obtained as the slope of a linear fit of a U-ΔT plot. For a more accurate measurement of the thermovoltage U, the amplitudes of T_A were chosen of the order of $10\,K$.

A program was written in Qt4/C++ for the data acquisition and control of the devices. The data were acquired every ten seconds starting with the temperatures T_A and T_B and the voltage U at zero current. Then, the temperatures were measured again followed by a current sweep. After this sweep, the temperatures are measured again for comparison with the values taken before. All data were saved into ASCII files and marked with timestamps.

Diode Calibration Since the calibrated Si-diodes have an absolute accuracy of $0.25\,K$, the diode measuring T_A was used as received from LakeShore, and a second diode was calibrated to it by mounting them next to each other on a copper block. Then, the copper block was cooled down to $6\,K$ and the cooling was turned off. T_A and the voltage over the second diode at a current of $10\,\mu A$ were recorded with the M9700 temperature controller during warming up. From these data, a calibration

curve was interpolated with 50 point from $7 - 25\,\mathrm{K}$ and another 50 points from $25.5 - 320\,\mathrm{K}$ and uploaded to the M9700. With this procedure, the resulting error in $\Delta T = T_A - T_B$ was decreased to about $0.02\,\mathrm{K}$.

Contacting   The nanowires were kept embedded in the membranes in order to provide mechanical stability to the array. Due to the softness of the membranes, soldering was impractical, and furthermore, the properties of the nanowires may change, e. g. by annealing or melting, when heating the sample up. However, the membrane also inhibits oxidation of the nanowires, oxidation being a problem discussed in the literature.[38,41] In this work, the electrodeposition was continued until caps grew. Then, a Au layer was sputtered on top of the caps, and the sample was clamped between the two polished Cu blocks described above.

Measurement   Figure 4.3 shows a representative set of data for a nanowire array with wire diameter $200\,\mathrm{nm}$ deposited in a $60\,\mathrm{\mu m}$ thick PC membrane with 10^8 channels cm^{-2}. The values of T_A, T_B, and U are shown as function of time in Figure 4.3(a). In Figure 4.3(b), the same data are also plotted as U versus ΔT for different mean temperatures (marked at the corresponding linear fit). Finally, the resulting Seebeck coefficient is plotted as function of the mean temperature in Figure 4.4.

For the interpretation of the data and a calculation of the absolute Seebeck coefficient of the sample, the leads and copper blocks have to be taken into account as well. Comparing the situation with Figure 4.2 and using linear approximations, one obtains

$$U = -S\Delta T_r + S_{\mathrm{Cu}}(\Delta T_r - \Delta T) + S_{\mathrm{pb}}\Delta T_r, \qquad (4.2)$$

being $\Delta T = T_B - T_A$ and $\Delta T_r = T_2 - T_1$ the measured and the real temperature difference, respectively, and S_{pb} and S_{Cu} the Seebeck coefficients of the leads and copper plates, respectively. If S_{pb} is neglected and the copper plates are ideal heat sinks, then $\Delta T = \Delta T_r$, and thus

$$S = -\frac{U}{\Delta T}. \qquad (4.3)$$

However, if there is a constant heat flow through our sample and both copper blocks, it will be proportional to

$$\frac{T_B - T_A}{2r_{\mathrm{Cu}} + r_s} = \frac{T_B - T_2}{r_{\mathrm{Cu}}} = \frac{T_2 - T_1}{r_s}, \qquad (4.4)$$

being r_{Cu} and r_s the heat resistance across one copper block and the sample, respectively. Therefore, one obtains for the ratio of temperature differences

$$y = \frac{T_B - T_A}{T_2 - T_1} = \frac{\Delta T}{\Delta T_r} = 1 + 2\,\frac{r_{\mathrm{Cu}}}{r_s} = 1 + 2\,\frac{l_{\mathrm{Cu}}\,\kappa_s}{l_s\,\kappa_{\mathrm{Cu}}}, \qquad (4.5)$$
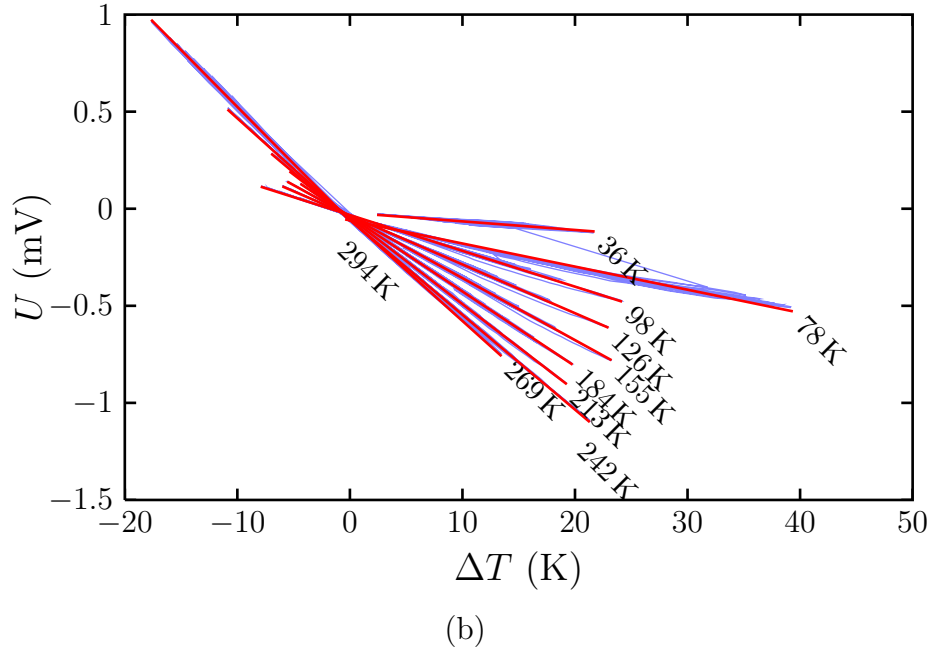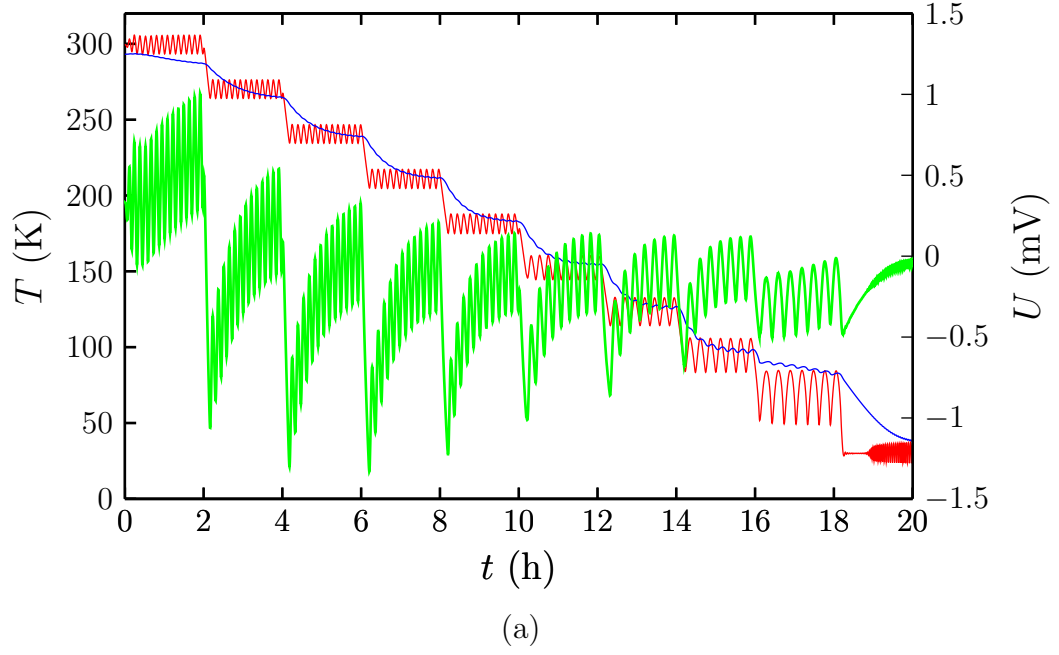
(a)

(b)

Figure 4.3: (a) Measured temperatures T_A (red) and T_B (blue) and voltage U (green) for an array of nanowires with $x \approx 0.15$, $d = 200\,\mathrm{nm}$, and a channel density of 10^8 cm^{-2}. (b) Voltage versus temperature difference during oscillations. The mean temperatures are noted in graph.
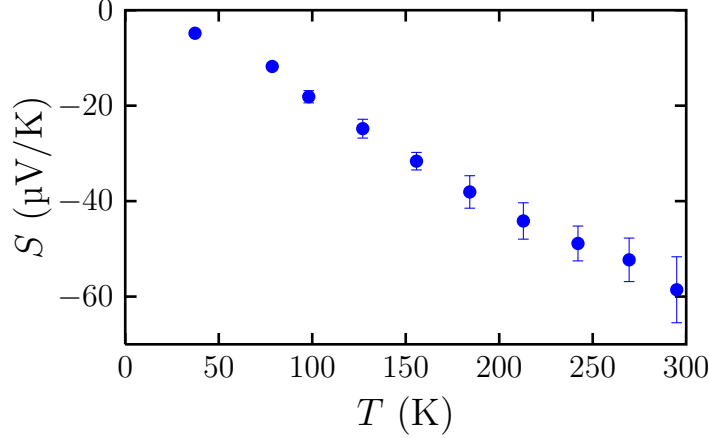
Figure 4.4: Seebeck coefficient S resulting from the data in Figure 4.3 as function of the mean temperature.

introducing the thickness l and the thermal conductivity κ. In our case, the nanowires represent only a few per mille to percent of the sample volume. Therefore, their heat conductance is neglected here, and we have $l_s = 30\,\mu\mathrm{m}$, $l_{\mathrm{Cu}} = 3\,\mathrm{mm}$, and $\kappa_{\mathrm{Cu}} = 400$ [146] and $\kappa_s = 0.2\,\mathrm{Wm^{-1}K^{-1}}$. Thus, $\Delta T = 1.1\,\Delta T_r$. This should give an estimate of the maximum deviation in our measurements. Inserting this result into Equation 4.2 (still neglecting the phosphor bronze contribution) to estimate the S under these conditions, provides

$$S = -\frac{U}{\Delta T}y + S_{\mathrm{Cu}}(1-y). \qquad (4.6)$$

4.2 Results

Figure 4.5 shows the results of the Seebeck coefficients evaluated from the slopes of $U - \Delta T$ curves for nanowire arrays with different wire diameters as function of the absolute temperature. The nanowires were prepared as described in Section 2.2.3. In Figure 4.5(a), the values measured for Sb nanowires are shown. For all samples S was positive, lower than the bulk value (Figure 1.5), and decreased with decreasing temperature. There is no clear dependence of the wire diameter on the Seebeck coefficient.

For Bi nanowires, a mostly negative Seebeck coefficient was measured for both samples (Figure 4.5(b)). Only at 30 K, the sample with 100 nm wire diameter exhibited a small positive S. $|S|$ was smaller for smaller wire diameter. In Figure 4.5(c), the results for $\mathrm{Bi}_{1-x}\mathrm{Sb}_x$ alloy nanowires are presented. The arrays with

50 nm diameter exhibit a small positive S at lower temperatures. For 100 nm diameter and $c(\text{Sb}) = 0.01\,\text{mol/l}$ ($x \approx 0.1$) the absolute value of the Seebeck coefficient was larger than for the other samples and exhibited a maximum at 180 K.

In general, the absolute value of S were lower than the respective bulk value (compare Figure 1.5) as also found by Heremans et al. for 200 nm diameter Bi nanowires.[50] S was also decreasing with decreasing temperature in most cases. Boukai et al. observed this in their studies on polycrystalline Bi nanowires.[41] However, they found both individual p- and n-type Bi nanowires. For sub-µm Bi wires, Nikolaeva et al. even found wires with changing sign of the Seebeck coefficient and $S > 70\,\text{µV/K}$ at 50 K.[53] This behavior was not observed in this work for Bi nanowires. $|S|$ seemed to follow a trend towards lower values for smaller wire diameter. However, a conclusive connection between wire diameter and S was not found and values reported in the literature for Bi nanowires also do not give a uniform picture. The crystalline orientation and crystallite sizes may play an important role for the correct interpretation of the Seebeck coefficients. Even for bulk Bi a large influence of these parameters on S was reported.[75] Furthermore, when measuring an array, an average value, similar to Equation 1.30, is obtained.

In Figure 4.6, the resistance ratios $R/R(273.15\,\text{K})$ are shown as a function of temperature for Bi, Sb, and Bi$_{1-x}$Sb$_x$ nanowire arrays with different wire diameters. The values were computed as mean values of the slopes of the $I - U$ curves taken at a mean temperature and subsequently normalized to the value obtained for $T = 273.15\,\text{K}$. For Sb nanowires, Figure 4.6(a) shows that the temperature dependence of resistance is metal-like, The resistance decreases with decreasing temperature as for bulk Sb (compare Figure 1.5). However, the resistance of the nanowire arrays is less influenced by the temperature than for bulk. This is in accordance with measurements made by Heremans et al. on Sb nanowire arrays.[147] The mean free paths of charge carriers in Sb are $100 - 200\,\text{nm}$.[148] Thus, finite-size effects could explain the difference between the values for bulk and nanowires. Again, we measure a combined value for a parallel connection of individual nanowires. Thus,

$$\frac{1}{R} = \sum_i \frac{1}{R_i} = \sum_i \frac{A_i}{\rho_i l}, \tag{4.7}$$

being l the length of the nanowires and A_i the cross-sectional area.

Figure 4.6(b) shows the resistance ratio for Bi nanowire arrays. A non-monotonic dependence on the temperature with one maximum is observed. Such a behavior was reported in the literature and attributed to finite- and quantum-size effects.[50,51,53,81,149,150] The mean free path of charge carries in Bi is of the order of 100 µm.[9,10] Thus, a larger effect is expected for Bi than for Sb nanowires.

For the arrays of Bi$_{1-x}$Sb$_x$ nanowires, a metal-like resistance was found for
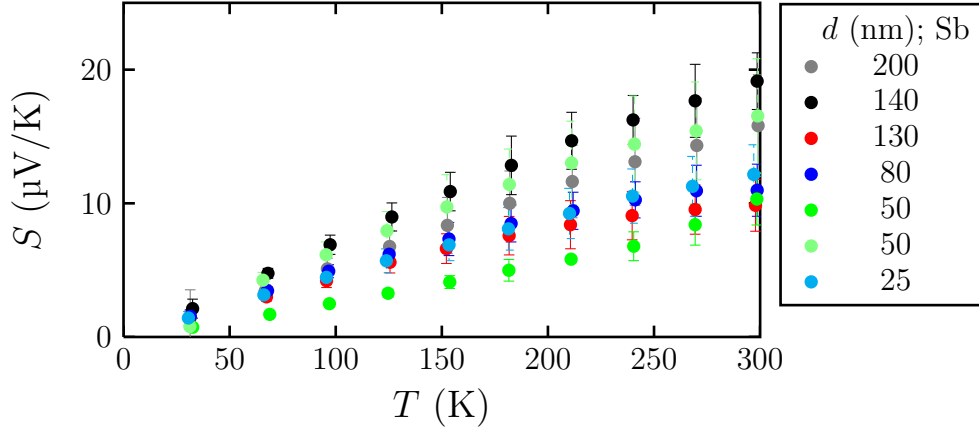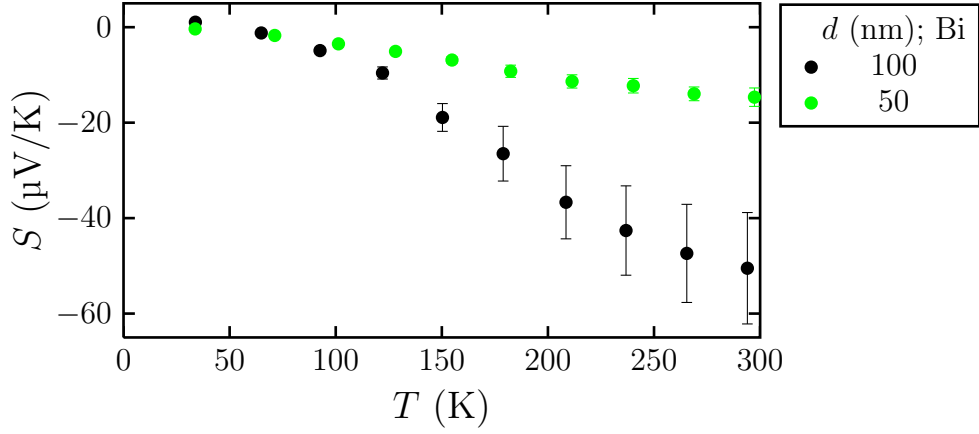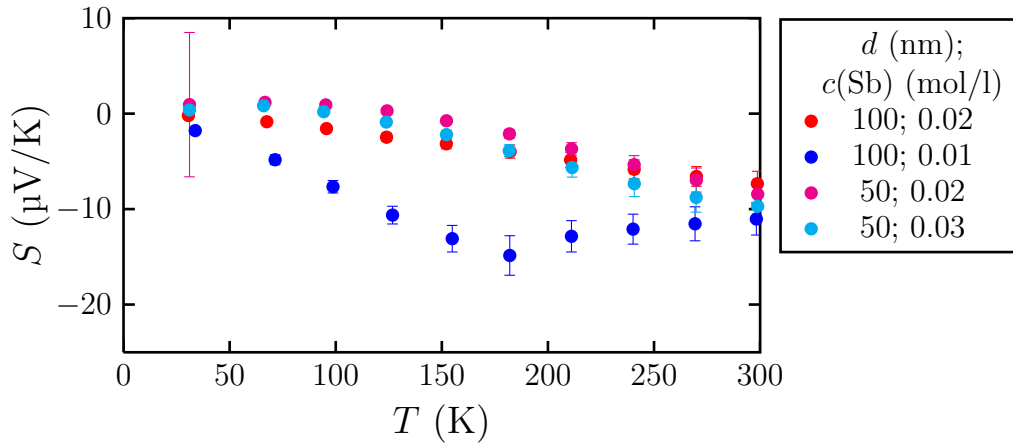
Figure 4.5: Seebeck coefficients of nanowire arrays with different composition and nanowire diameter separated into (a) Sb, (b) Bi, and (c) $Bi_{1-x}Sb_x$ alloy nanowire arrays.

100 nm wire diameter and $c(\text{Sb}) = 0.02\,\text{mol/l}$ ($x \approx 0.15$), whereas for the other two samples with 50 nm wire diameter, maxima were measured. This is not in agreement with the findings of Lin et al.[151] They reported a monotonically increasing resistance ratio for 40 nm wire diameter and a {012} texture of the wires.

The setup was also used to measure the Seebeck coefficient of Bi$_2$Te$_3$ nanowire arrays with wire diameters of 30 nm.[112,152] Depending on the exact stoichiometry, bulk Bi$_2$Te$_3$ can be p- or n-type, where the n-type material has an excess of Te.[153] At room temperature $S \approx \pm 200\,\mu\text{V/K}$ was found for bulk p- and n-type Bi$_2$Te$_3$, respectively, and a decreasing $|S|$ for decreasing T was reported.[153]

For these measurements, Bi$_2$Te$_3$ nanowire arrays were deposited potentiostatically with $U = 0\,\text{mV}$ vs. SCE at $4\,^\circ\text{C}$ from electrolytes (labelled L, H, and J) with different concentration ratios of Bi and Te: 3.75/5, 7.5/5, and 10/5 mmol/mmol, respectively. In Figure 4.7, the results are summarized as function of temperature. Also for Bi$_2$Te$_3$ nanowires, S is decreasing with decreasing temperature. The absolute value of S at room temperature is comparable to the values presented by Lee et al. for p-type Bi$_2$Te$_3$ nanowires prepared by pulsed electrodeposition and a wire diameter of 50 nm.[154] Thus, they also report S values lower than bulk. In our case, all samples were found to be n-type.

4.3 Conclusion

Nanowire arrays prepared by potentiostatic and pulsed deposition were contacted by sputtering a Au layer on top of caps grown on the nanowire array. The resistance of nanowire arrays prepared by pulsed deposition was much smaller indicating a more homogeneous growth, and thus, a larger number of contacted wires. These nanowire arrays were suitable for the measurement of the Seebeck coefficient.

In this work, any contacting method that is likely to change the properties of the nanowires or the membrane by heating, oxidation, or corrosion was avoided, such as using silver epoxy, Wood's metal, or silver paint. Due to the low thermal conductivity of the polymeric matrix, it is possible to create larger temperature gradients across the samples by periodic heating and cooling. For most samples, the absolute value of the Seebeck coefficient is decreasing with decreasing temperature and lower than the bulk value. In addition, the resistance was obtained by measuring $I - U$ curves.

The dependence of the resistivity ratios $R/R(273.15\,\text{K})$ on temperature was in agreement with values presented in the literature except for Bi$_{1-x}$Sb$_x$ alloy nanowire arrays. For Bi$_{1-x}$Sb$_x$ nanowire arrays, it was found that the ratio decreased with decreasing temperature, while previous works reported an increasing ratio. Values previously reported in the literature and these measurements do not yet show a clear connection between the wire diameter and the thermoelectric

(a)

(b)

(c)
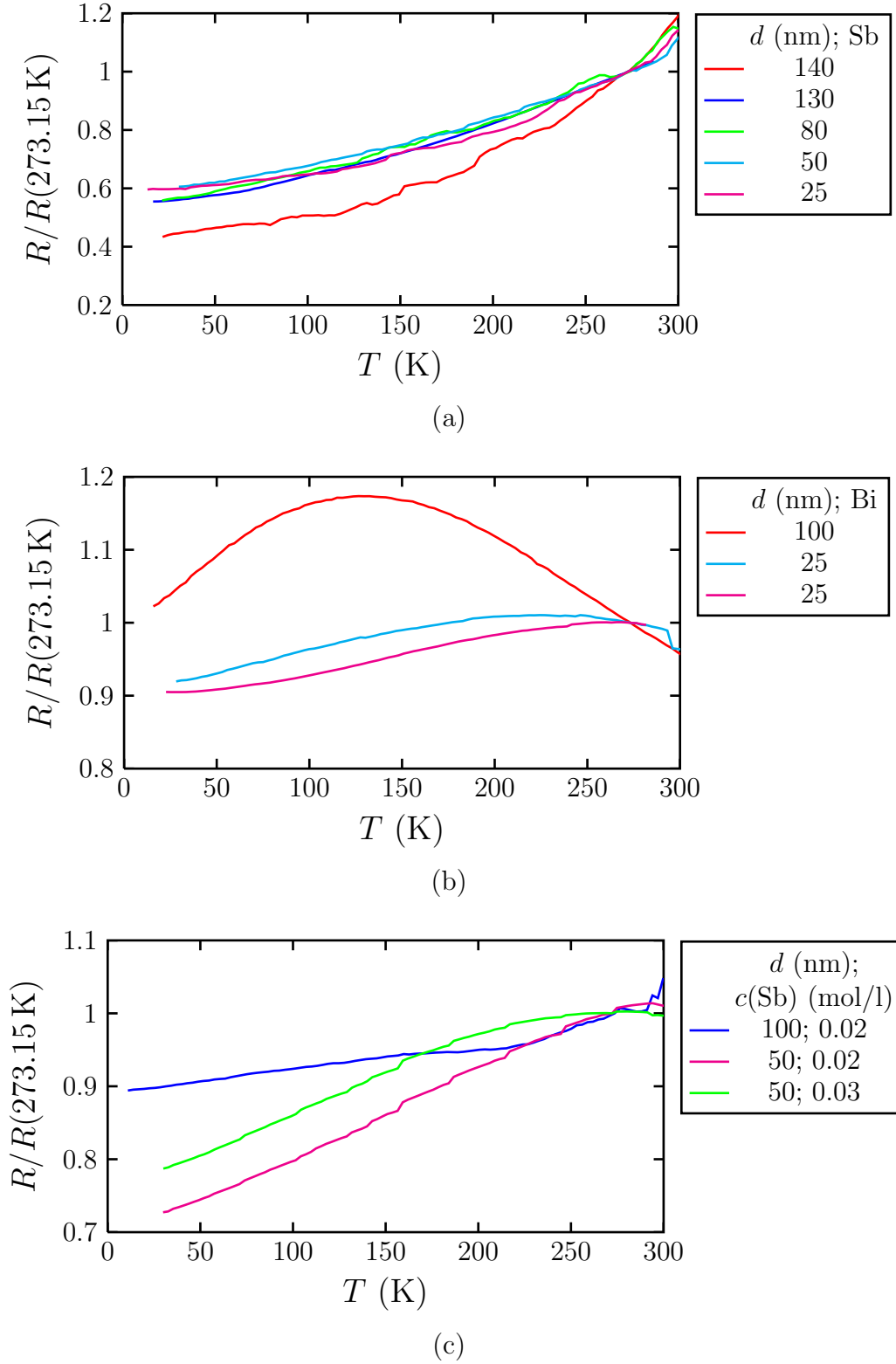
Figure 4.6: Resistivity ratios as a function of temperature, composition, and wire diameter for (a) Sb, (b) Bi, and (c) $Bi_{1-x}Sb_x$ alloy nanowire arrays.
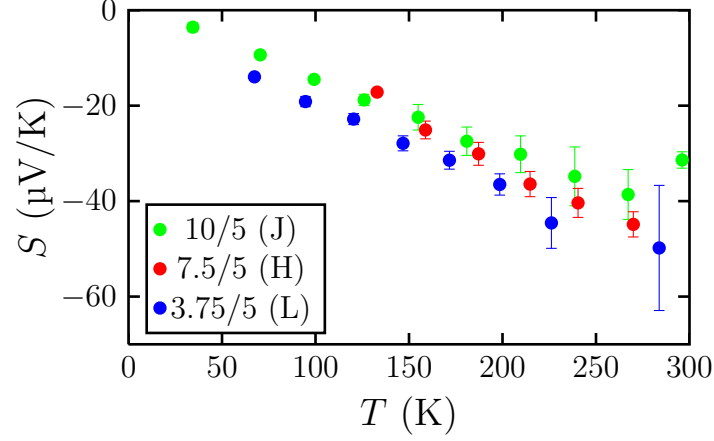
Figure 4.7: Seebeck coefficients of 30 nm diameter Bi$_2$Te$_3$ nanowire arrays deposited from electrolytes with different Bi/Te ratios (mmol/mmol).

properties. Thus, more detailed studies of the crystallite sizes and the crystalline orientation are necessary to study finite- and quantum-size effects due to scattering at grain boundaries and at the surface.

It was found that Bi, Bi-rich Bi$_{1-x}$Sb$_x$ alloys, and Bi$_2$Te$_3$ nanowires are mostly n-type materials, whereas the investigated Sb nanowires were p-type. Hence, these p- and n-type materials can be combined for nanostructured Peltier devices.

5 Summary and Outlook

In this work, the synthesis of $Bi_{1-x}Sb_x$ nanowires with controlled composition $0 < x < 0.5$ and diameter between 20 and 200 nm was demonstrated for two different template materials, PC and PET. Wires grown in PET membranes exhibited an enhanced surface roughness which may lead to an enhanced phonon scattering at the surface, and thus, to a higher thermoelectrical efficiency.

The nanowires were characterized by XRD to evaluate the composition and the texture. Bi-rich nanowires showed a {110} texture, whereas a more pronounced {012} texture is observed for the Sb nanowires. In addition to the XRD measurements, quantitative analysis by SEM-EDX and TEM-EDX was performed on the nanowires. It was shown, that the composition was controlled by the concentrations of Bi and Sb in the electrolyte and the choice of the deposition potential. Further characterization by BF and DF imaging and HR-TEM, revealed that the nanowires are polycrystalline with average crystallite size of the order of 100 nm.

In order to improve the homogeneity of the deposition process, pulsed electrodeposition was employed. The resulting nanowire arrays were more suitable for the measurement of Seebeck coefficient and resistance. These two thermoelectrical properties were characterized on Bi, Sb, and $Bi_{1-x}Sb_x$ nanowire arrays with different wire diameter and, for the alloy nanowires, different compositions at temperatures of 30 to 300 K. Additionally, the Seebeck coefficient of Bi_2Te_3 nanowire arrays was measured. The absolute value of the Seebeck coefficient was found to be smaller than for the respective bulk counterpart and also the temperature dependance of the resistance showed a behaviour different from bulk.

Further measurements of the thermoelectric transport properties are necessary to understand transport mechanisms in confined $Bi_{1-x}Sb_x$ structures. To minimize the error in measuring S with the presented method and for sensing applications, it is desirable to have thick templates and long nanowires. 60 and 100 µm thick PC foils are available. However, the aspect ratio of the nanochannels is limited by Equation 2.4. The minimum wire diameter is, therefore, about 1000 times smaller than the template thickness. Thus, the nanowires characterized in Section 4.2 were prepared in 30 µm thick membranes. In order to fabricate thin nanowires also in such thick membranes, further treatment of the ion-track etched templates is necessary to make the nanochannels thinner again in a controlled way, e. g., by atomic layer deposition of an insulating material. In parallel, the group of Prof. Völklein (Hochschule RheinMain) developed microchips for the characterization of

σ, S, and κ on individual nanowires.[155] The results will be compared to the data presented in this work.

At GSI, also polymer templates with a single nanochannel can be fabricated. Thus, individual nanowires could be contacted in order to measure the resistivity.[156] Up to now, the thermoelectric transport properties of rough $Bi_{1-x}Sb_x$ nanowires have not been characterized. PET foils have a smooth surface on both sides. In order to measure S and R on nanowire arrays embedded in PET, the adhesion of the back electrode has to be improved.

At the European Synchrotron Radiation Facility, nuclear inelastic scattering measurements were performed on nanowires in collaboration with the group of Prof. Hermann (Forschungszentrum Jülich) in order to study the influence of surface roughness and wire diameter on the phonon density of states. The data are currently under evaluation.

The realization of miniaturized Peltier elements relevant for sensing applications should be pursued. For potential applications based on nanowire arrays, e. g. in sensors, it is important to fabricate structured arrays.

1. Infra-red sensors could consist of small neighboring p- and n-type wire arrays. However, these arrays have to be made of different materials and need to be well separated from each other. Therefore, polymer foils will be irradiated using masks thick enough to stop ions in selected areas, in order to produce ion tracks only in special regions to have a pre-structuring of the template. Preliminary experiments of subsequent deposition of two different materials in an electrochemical cell were successful. Four patches of 1 mm diameter were filled separately with Bi and Sb nanowires. For the deposition of each material, the electrolyte was exchanged. In the next step, these structures have to be scaled down by, e. g., lithographic techniques.

2. Such sensors are more efficient, when the matrix is removed. However, Bi and Sb are brittle, and the nanowires break more easily for smaller wire diameters. At the irradiation setup at the UNILAC (GSI), it is possible to irradiate polymer foils under various angles.[157] Thus, templates for nanowire networks, i. e. interconnected nanowires,[158] and freestanding nanostructures with enhanced mechanical stability will be fabricated.

A further investigation of pulsed deposition and the resulting nanowires by XRD, EDX, and TEM is necessary to achieve a more homogeneous growth and a better control over the texture and the crystalline structure. This is necessary to study the influence of these properties on the thermoelectric transport properties and integration into devices. In addition, the deposition from the $Bi_{1-x}Sb_x$ electrolyte should be stopped inside the membrane and continued with Au electrolyte to

improve the contact to the $Bi_{1-x}Sb_x$ nanowires and avoid effects of $Bi_{1-x}Sb_x$ caps during transport measurements on nanowire arrays.

The influence of diameter, channel length, and channel density on the electrochemical deposition of $Bi_{1-x}Sb_x$ in nanochannels is not yet fully understood. Here, more theoretical work might help to find optimal deposition conditions. Additionally, materials related to $Bi_{1-x}Sb_x$ and Bi_2Te_3 like the ternary $(Bi_{1-x}Sb_x)_2Te_3$ compound can be prepared by electrodeposition from aqueous solutions. Doping with Te, Sb, and Sn can in general improve the thermoelectric performance of $Bi_{1-x}Sb_x$.

Acknowledgments

I would like to thank . . .

- **Prof. Dr. Annemarie Pucci**
  for acting as referee.

- **Prof. Dr. Reinhard Neumann**
  for supervision during the studies, proofreading the manuscript, and acting as referee.

- the **DFG**
  for financial support within the priority program 1386.

- **Dr. M. Eugenia Toimil-Molares**
  for supervision, proofreading, and many ideas.

- **Dr. Kay-Obbe Voss**
  for help with the cryostat and other devices.

- **Dr. Oliver Picht**
  for helpful discussions and providing Bi_2Te_3 samples.

- **Christian Schötz**, **Michael Wagner**, and **Marco Cassinelli**,
  for assistance during the nanowire fabrication.

- **Arne Siegmund**, **Elko Schubert**, and the **GSI workshop**
  for help with manufacturing pieces, mechanical drawings, and the setups.

- **Dr. Siegfried Klaumünzer** and **Dr. Daniel Severin**
  for helpful discussions about XRD.

- **Prof. Oliver Eibl** and **Dr. Nicola Peranio**
  for many TEM measurements and a great and interesting introduction into transmission electron microscopy.

- **Dr. Wilfried Sigle**, **Dr. Peter Kopold**, and **Burak Özdöl**
  for studious (HR-)TEM measurements, helpful discussions, and a fruitful collaboration.

List of Software

Data acquisition: Programs written in LabView 7.1, C++, and Qt4.7/C++ with NI-DAQmx libraries and parts of the GNU Scientific Library 1.15.

Data processing, conversion, and plotting: Scripts written in Perl 5.12, Octave 3.2.4, and pgfplots.

XRD: Seifert Analysis RayfleX 2.405.

EDX: Esprit 1.8 (Darmstadt), Noran System SIX (Stuttgart), Oxford Instruments (Tübingen).

SEM/TEM image processing: ImageJ 1.46, GIMP 2.7.5.

Vector graphics, CAD, printed circuit board design: Inkscape 0.48, AUTO CAD-2002, EAGLE 5.6.

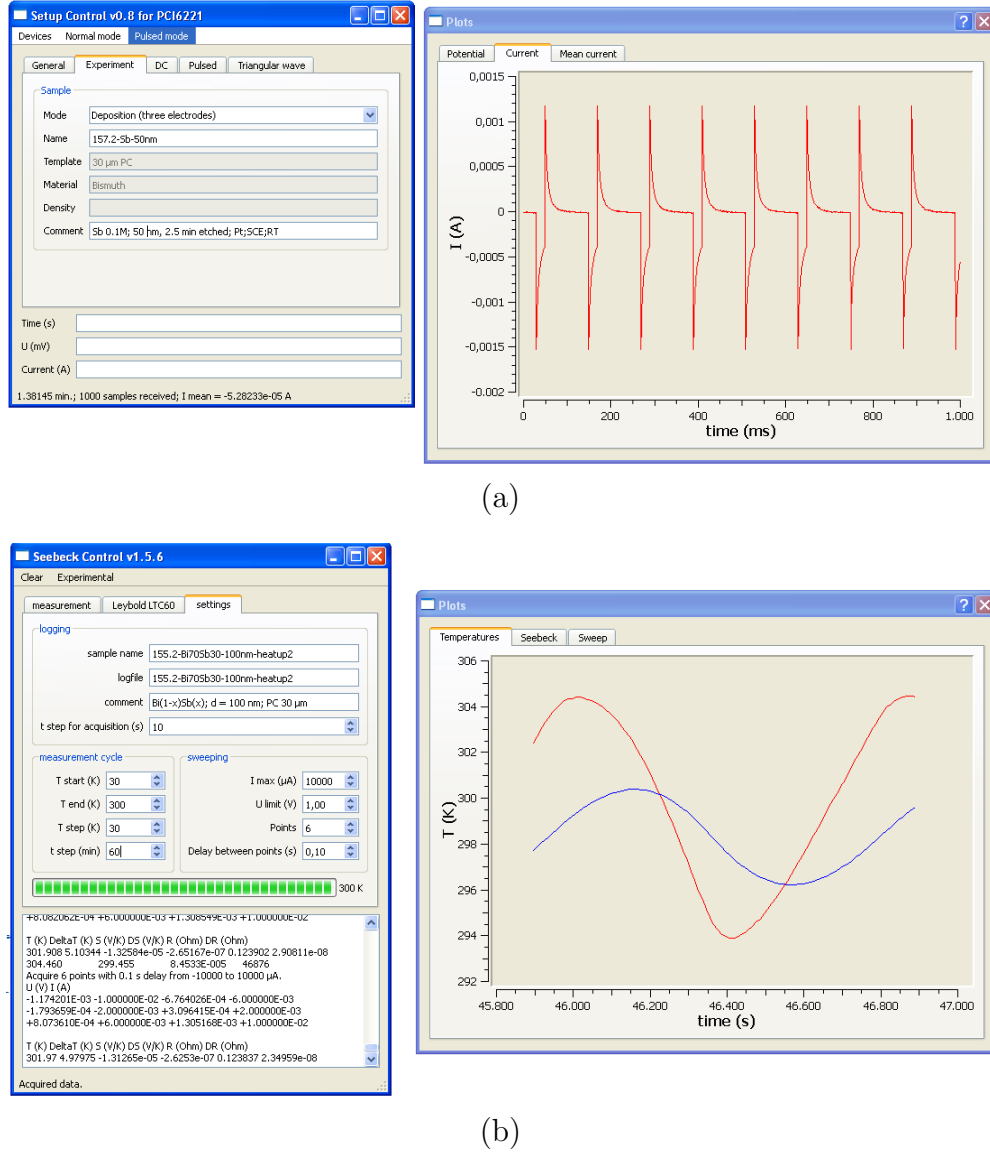**Simulations:** CASINO V2.42, SRIM-2008.

(a)

(b)

Figure 5.1: Graphical user interfaces of the programs written in Qt4/C++: (a) program written to set different $U(t)$ output voltages and acquire data at up to $1\,\mathrm{kHz}$ during electrodeposition and (b) program written to control the devices involved in the Seebeck measurements.

Bibliography

[1] T. J. Seebeck. Ueber die magnetische Polarisation der Metalle und Erze durch Temperatur-Differenz. *Annalen der Physik*, 3:253–286, 1826.

[2] G. S. Nolas, J. Sharp, and H. J. Goldsmid. *Thermoelectrics - Basic Principles and New Materials Developments*. Springer, 2001.

[3] NASA. *Cassini Mission: Final supplemental environmental impact statement*. NASA, 1995.

[4] L. D. Hicks and M. S. Dresselhaus. Effects of quantum-well structures on the thermoelectric figure of merit. *Physical Review B*, 47:12727–12731, 1993.

[5] L. D. Hicks, T. C. Harman, and M. S. Dresselhaus. Use of quantum-well superlattices to obtain a high figure of merit from nonconventional thermoelectric materials. *Applied Physics Letters*, 63:3230–3232, 1993.

[6] L. D. Hicks and M. S. Dresselhaus. Thermoelectric figure of merit of a one-dimensional conductor. *Physical Review B*, 47:16631–16634, 1993.

[7] Shadyar Farhangfar. Quantum size effects in a one-dimensional semimetal. *Physical Review B*, 74:205318–1–5, 2006.

[8] N. Garcia, Y. H. Kao, and M. Strongin. Galvanomagnetic Studies of Bismuth Films in the Quantum-Size-Effect Region. *Physical Review B*, 5:2029–2039, 1972.

[9] E. H. Sondheimer. The Mean Free Path of Electrons in Metals. *Philosophical Magazine*, 1:1–42, 1952.

[10] V. F. Gantmakher and Yu. S. Leonov. Temperature Dependence of Electron Mean Free Path in Bismuth. *ZhETF Pis ma Redaktsiiu*, 8:264–269, 1968.

[11] Yu. F. Ogrin, V. N. Lutskii, and M. I. Elinson. Observation of Quantum Size Effects in Thin Bismuth Films. *Zhurnal eksperimental'noi i teoreticheskoi fiziki*, 3:114–118, 1966.

[12] Yu. F. Komnik and E. I. Bukhshtab. Observation of Quantum Oscillations of Conductivity in Thin Antimony Films. *Zhurnal eksperimental'noi i teoreticheskoi fiziki*, 6:536–540, 1967.

[13] Yu. F. Komnik and E. I. Bukhshtab. Observation of the Quantum and Classical Size Effects in Polycrystalline Thin Bismuth Films. *Zhurnal eksperimental'noi i teoreticheskoi fiziki*, 54:63–68, 1968.

[14] V. Damodara Das and N. Jayaprakash. Oscillatory behaviour of resistivity with thickness in bismuth thin films. *Vacuum*, 31:199–202, 1981.

[15] E. I. Rogacheva, S. N. Grigorov, O. N. Nashchekina, S. Lyubchenko, and M. S. Dresselhaus. Quantum-size effects in n-type bismuth thin films. *Applied Physics Letters*, 82:2628–2630, 2003.

[16] C. A. Hoffman, J. R. Meyer, F. J. Bartoli, A. Di Venere, X. J. Yi, C. L. Hou, H. C. Wang, J. B. Ketterson, and G. K. Wong. Semimetal-to-semiconductor transition in bismuth thin films. *Physical Review B*, 48:11431–11434, 1993.

[17] F. Y. Yang, Kai Liu, Kimin Hong, D. H. Reich, P. C. Searson, and C. L. Chien. Large Magnetoresistance of Electrodeposited Single-Crystal Bismuth Thin Films. *Science*, 284:1335–1337, 1999.

[18] F. Völklein and E. Kessler. A Method for the Measurement of Thermal Conductivity, Thermal Diffusivity, and Other Transport Coefficients of Thin Films. *physica status solidi (a)*, 81:585–596, 1984.

[19] F. Völklein and E. Kessler. Analysis of the Lattice Thermal Conductivity of Thin Films by Means of a Modified Mayadas-Shatzkes Model: The Case of Bismuth Films. *Thin Solid Films*, 142:169–181, 1986.

[20] F. Völklein and E. Kessler. Thermal Conductivity and Thermoelectric Figure of Merit of Thin Antimony Films. *physica status solidi (b)*, 158:521–529, 1990.

[21] D. T. Morelli, D. L. Partin, and J. Heremans. Galvanomagnetic properties of single-crystal bismuth-antimony thin films. *Semiconductor Science and Technology*, 5:S257–S259, 1990.

[22] Yu-Ming Lin, Xiangzhong Sun, and M. S. Dresselhaus. Theoretical investigation of thermoelectric transport properties of cylindrical Bi nanowires. *Physical Review B*, 62:4610–4623, 2000.

104

[23] O. Rabin, Y.-M. Lin, and M. S. Dresselhaus. Anomalously high thermo-electric figure of merit in $Bi_{1-x}Sb_x$ nanowires by carrier pocket alignment. *Applied Physics Letters*, 79:81–83, 2001.

[24] J. E. Cornett and O. Rabin. Thermoelectric figure of merit calculations for semiconducting nanowires. *Applied Physics Letters*, 98:182104–1–3, 2011.

[25] T. W. Cornelius, M. E. Toimil-Molares, R. Neumann, G. Fahsold, R. Lovrin-cic, A. Pucci, and S. Karim. Quantum size effects manifest in infrared spectra of single bismuth nanowires. *Applied Physics Letters*, 88:103114–1–3, 2006.

[26] B. Lenoir, M. Cassart, J. Michenaud, H. Scherrer, and S. Scherrer. Transport Properties of Bi-rich Bi-Sb Alloys. *Journal of Physics and Chemistry of Solids*, 57:89–99, 1996.

[27] B. Lenoir, A. Dauscher, M. Cassart, Yu. I. Ravich, and H. Scherrer. Effect of Antimony Content on the Thermoelectric Figure of Merit of $Bi_{1-x}Sb_x$ Alloys. *Journal of Physics and Chemistry of Solids*, 59:129–134, 1998.

[28] P. M. Vereecken, S. Ren, L. Sun, and P. C. Searson. Electrodeposition of $Bi_{1-x}Sb_x$ Thin Films. *Journal of the Electrochemical Society*, 150:C131–C139, 2003.

[29] F. Besse, C. Boulanger, and J. M. Lecuire. Preparation of $Bi_{1-x}Sb_x$ films by electrodeposition. *Journal of Applied Electrochemistry*, 30:385–392, 2000.

[30] F. Besse, C. Boulanger, B. Bolle, and J. J. Heizmann. Influence of electro-chemical deposition conditions on the texture of bismuth antimony alloys. *Scripta Materialia*, 54:1111–1115, 2006.

[31] Sunglae Cho, Antonio DiVenere, George K. Wong, John B. Ketterson, and Jerry R. Meyer. Thermoelectric transport properties of n-doped and p-doped $Bi_{0.91}Sb_{0.09}$ alloy thin films. *Journal of Applied Physics*, 85:3655–3660, 1999.

[32] Doriane Del Frari, Sebastien Diliberto, Nicolas Stein, Clotilde Boulanger, and Jean-Marie Lecuire. Pulsed electrodeposition of $(Bi_{1-x}Sb_x)_2Te_3$ thermo-electric thin films. *Journal of Applied Electrochemistry*, 36:449–454, 2006.

[33] Chien-Neng Liao, Kuen-Ming Liou, and Hsu-Shen Chu. Enhancement of thermoelectric properties of sputtered Bi-Sb-Te thin films by electric current stressing. *Applied Physics Letters*, 93:042103–1–3, 2008.

[34] Liang Li, Yong Zhang, Guanghai Li, and Lide Zhang. A route to fabricate single crystalline bismuth nanowire arrays with different diameters. *Chemical Physics Letters*, 378:244–249, 2003.

[35] T. W. Cornelius, J. Brötz, N. Chtanko, D. Dobrev, G. Miehe, R. Neumann, and M. E. Toimil Molares. Controlled fabrication of poly- and single-crystalline bismuth nanowires. *Nanotechnology*, 16:S246–S249, 2005.

[36] Y. Zhang, G. Li, Y. Wu, B. Zhang, W. Song, and L. Zhang. Antimony Nanowire Arrays Fabricated by Pulsed Electrodeposition in Anodic Alumina Membranes. *Advanced Materials*, 14:1227–1230, 2002.

[37] Xincun Dou, Guanghai Li, and Hechang Lei. Kinetic versus thermodynamic control over growth process of electrodeposited Bi/BiSb superlattice nanowires. *Nano Letters*, 8:1286–1290, 2008.

[38] Stephen B. Cronin, Yu-Ming Lin, Oded Rabin, Marcie R. Black, Jackie Y. Ying, Mildred S. Dresselhaus, Pratibha L. Gai, Jean-Paul Minet, and Jean-Paul Issi. Making electrical contacts to nanowires with a thick oxide coating. *Nanotechnology*, 13:653–658, 2002.

[39] F. Zhou, J. H. Seol, A. L. Moore, L. Shi, Q. L. Ye, and R. Scheffler. One-dimensional electron transport and thermopower in an individual InSb nanowire. *Journal of Physics: Condensed Matter*, 18:9651–9657, 2006.

[40] P. Chiu and I. Shih. A study of the size effect on the temperature-dependent resistivity of bismuth nanowires with rectangular cross-sections. *Nanotechnology*, 15:1489–1492, 2004.

[41] A. Boukai, K. Xu, and J. R. Heath. Size-Dependent Transport and Thermoelectric Properties of Individual Polycrystalline Bismuth Nanowires. *Advanced Materials*, 18:864–869, 2006.

[42] Wooyoung Shim, Jinhee Ham, Kyoung-il Lee, Won Young Jeung, Mark Johnson, and Wooyoung Lee. On-film formation of Bi nanowires with extraordinary electron mobility. *Nano Letters*, 9:18–22, 2009.

[43] Kornelius Nielsch, Julien Bachmann, Johannes Kimling, and Harald Böttner. Thermoelectric Nanostructures: From Physical Model Systems towards Nanograined Composites. *Advanced Energy Materials*, 1:713–731, 2011.

[44] Eyal Shapira, Amir Holtzman, Debora Marchak, and Yoram Selzer. Very high thermopower of Bi nanowires with embedded quantum point contacts. *Nano Letters*, 12:808–812, 2012.

[45] Li Shi, Choongho Yu, and Jianhua Zhou. Thermal characterization and sensor applications of one-dimensional nanostructures employing microelectromechanical systems. *Journal of Physical Chemistry B*, 109:22102–22111, 2005.

[46] Anastassios Mavrokefalos, Arden L. Moore, Michael T. Pettes, Li Shi, Wei Wang, and Xiaoguang Li. Thermoelectric and structural characterizations of individual electrodeposited bismuth telluride nanowires. *Journal of Applied Physics*, 105:104318–1–8, 2009.

[47] T. W. Cornelius. *Fabrication and Characterisation of Bismuth Nanowires*. PhD thesis, University of Heidelberg, 2006.

[48] T. W. Cornelius, O. Picht, S. Müller, R. Neumann, F. Völklein, S. Karim, and J. L. Duan. Burnout current density of bismuth nanowires. *Journal of Applied Physics*, 103:103713–1–5, 2008.

[49] M. Black, Y.-M. Lin, S. B. Cronin, O. Rabin, and M. S. Dresselhaus. Infrared absorption in bismuth nanowires resulting from quantum confinement. *Physical Review B*, 65:195417–1–9, 2002.

[50] J. Heremans and C. M. Thrush. Thermoelectric power of bismuth nanowires. *Physical Review B*, 59:12579–12583, 1999.

[51] Zhibo Zhang, Xiangzhong Sun, M. S. Dresselhaus, Jackie Y. Ying, and J. Heremans. Electronic transport properties of single-crystal bismuth nanowire arrays. *Physical Review B*, 61:4850–4861, 2000.

[52] Joseph P. Heremans, Christopher M. Thrush, Donald T. Morelli, and Ming-Cheng Wu. Thermoelectric Power of Bismuth Nanocomposites. *Physical Review Letters*, 88:216801–1–4, 2002.

[53] A. Nikolaeva, T. E. Huber, D. Gitsu, and L. Konopko. Diameter-dependent thermopower of bismuth nanowires. *Physical Review B*, 77:035422–1–10, 2008.

[54] Arden L. Moore, Michael T. Pettes, Feng Zhou, and Li Shi. Thermal conductivity suppression in bismuth nanowires. *Journal of Applied Physics*, 106: 034310–1–7, 2009.

[55] Jong Wook Roh, Kedar Hippalgaonkar, Jin Hee Ham, Renkun Chen, Ming Zhi Li, Peter Ercius, Arun Majumdar, Woochul Kim, and Wooyoung Lee. Observation of Anisotropy in Thermal Conductivity of Individual Single-Crystalline Bismuth Nanowires. *ACS Nano*, 5:3954–3960, 2011.

[56] A. I. Boukai, Y. Bunimovich, J. Tahir-Kheli, J.-K. Yu, W. A. Goddard III, and J. R. Heath. Silicon nanowires as efficient thermoelectric materials. *Nature*, 451:168–171, 2008.

Bibliography

[57] A. I. Hochbaum, R. Chen, R. D. Delgado, W. Liang, E. C. Garnett, M. Najarian, A. Majumdar, and P. Yang. Enhanced thermoelectric performance of rough silicon nanowires. *Nature*, 451:163–168, 2008.

[58] T. Elbel. Miniaturized thermoelectric radiation sensors covering a wide range with respect to sensitivity or time constant. *Sensors and Actuators A*, 25-27: 653–656, 1991.

[59] T. Elbel, R. Lenggenhager, and H. Baltes. Model of thermoelectric radiation sensors made by CMOS and micromachining. *Sensors and Actuators A*, 35: 101–106, 1992.

[60] A. W. van Herwaarden and P. M. Sarro. Thermal sensors based on the Seebeck effect. *Sensors and Actuators*, 10:321–346, 1986.

[61] J. Happich. Building ultra-thin flexible IR sensors from thermoelectric nanowires. *Electronic Engineering Times*, December:36–37, 2010.

[62] F. Völklein, G. Min, and D. M. Rowe. Modelling of a microelectromechanical thermoelectric cooler. *Sensors and Actuators*, 75:95–101, 1999.

[63] W. Wang, F. Jia, Q. Huang, and J. Zhang. A new type of low power thermoelectric micro-generator fabricated by nanowire array thermoelectric material. *Microelectronic Engineering*, 77:223–229, 2005.

[64] M. Lindeberg and K. Hjort. Interconnected nanowire clusters in polyimide for flexible circuits and magnetic sensing applications. *Sensors and Actuators A*, 105:150–161, 2003.

[65] Hanna Yousef, Klas Hjort, and Mikael Lindeberg. Vertical Thermopiles Embedded in a Polyimide-Based Flexible Printed Circuit Board. *Journal of Microelectromechanical Systems*, 16:1341–1348, 2007.

[66] E. Koukharenko, X. Li, I. Nandhakumar, N. Frety, S. P. Beeby, D. Cox, M. J. Tudor, B. Schiedt, C. Trautmann, A. Bertsch, and N. M. White. Towards a nanostructured thermoelectric generator using ion-track lithography. *Journal of Micromechanics and Microengineering*, 18:104015–1–9, 2008.

[67] Alenka Razpet, Anders Johansson, Göran Possnert, Marek Skupiński, Klas Hjort, and Anders Hallén. Fabrication of high-density ordered nanoarrays in silicon dioxide by MeV ion track lithography. *Journal of Applied Physics*, 97:044310–1–4, 2005.

[68] E. J. Menke, M. A. Thompson, C. Xiang, L. C. Yang, and R. M. Penner. Lithographically patterned nanowire electrodeposition. *Nature Materials*, 5: 914–919, 2006.

[69] Minhee Yun, Nosang V. Myung, Richard P. Vasquez, Choonsup Lee, Erik Menke, and Reginald M. Penner. Electrochemically Grown Wires for Individually Addressable Sensor Arrays. *Nano Letters*, 4:419–422, 2004.

[70] Cynthia G. Zoski, Nianjun Yang, Peixin He, Luca Berdondini, and Milena Koudelka-Hep. Addressable nanoelectrode membrane arrays: fabrication and steady-state behavior. *Analytical Chemistry*, 79:1474–1484, 2007.

[71] Sven Müller, Christian Schötz, Oliver Picht, Wilfried Sigle, Peter Kopold, Markus Rauber, Ina Alber, Reinhard Neumann, and Maria E. Toimil-Molares. Electrochemical Synthesis of $Bi_{1-x}Sb_x$ Nanowires with Simultaneous Control on Size, Composition, and Surface Roughness. *Journal of Crystal Growth & Design*, 12:615–621, 2012.

[72] F. Völklein, H. Reith, T. W. Cornelius, M. Rauber, and R. Neumann. The experimental investigation of thermal conductivity and the Wiedemann-Franz law for single metallic nanowires. *Nanotechnology*, 20:325706–1–8, 2009.

[73] D. M. Rowe (also editor). *General Principles and Basic Considerations (Chapter 1 of Thermoelectrics Handbook: Makro to Nano)*. CRC Press, 2006.

[74] U. Birkholz, R. Fettig, and J. Rosenzweig. Fast semiconductor thermoelectric devices. *Sensors and Actuators*, 12:179–184, 1987.

[75] J.-P. Issi. *Thermoelectric Properties of the Group V Semimetals (Chapter 30 of Thermoelectrics Handbook: Makro to Nano edited by D. M. Rowe)*. CRC Press, 2006.

[76] J. Sommerlatte, K. Nielsch, and H. Böttner. Thermoelektrische Multitalente. *Physik Journal*, 6:35–41, 2007.

[77] P. Cucka and C. S. Barrett. The Crystal Structure of Bi and of Solid Solutions of Pb, Sn, Sb and Te in Bi. *Acta Crystallographica*, 15:865–872, 1962.

[78] A. Authier, editor. *International Tables for Crystallography Volume D: Physical Properties of Crystals*. Kluwer Academic Publishers, 2003.

Bibliography

[79] J. P. Dismukes, R. J. Paff, R. T. Smith, and R. Ulmer. Lattice parameter and density in bismuth-antimony alloys. *Journal of Chemical and Engineering Data*, 13:317–320, 1968.

[80] B. Lax, J. G. Mavroides, H. J. Zeiger, and R. J. Keyes. Infrared magnetoreflection in bismuth. I. High fields. *Physical Review Letters*, 5:241–243, 1960.

[81] Y.-M. Lin, S. B. Cronin, J. Y. Ying, M. S. Dresselhaus, and J. P. Heremans. Transport properties of Bi nanowire arrays. *Applied Physics Letters*, 76: 3944–3946, 2000.

[82] X. Sun. *The Effect of Quantum Confinement on the Thermoelectric Figure of Merit*. PhD thesis, Massachusetts Institute of Technology, 1999.

[83] J.-P. Issi. Low Temperature Transport Properties of the Group V Semimetals. *Australian Journal of Physics*, 32:585–628, 1979.

[84] R. B. Dingle. The electrical conductivity of thin wires. *Proceedings of the Royal Society of London. Series A, Mathematical and Physical Sciences*, 201: 545–560, 1949.

[85] A. F. Mayadas and M. Shatzkes. Electrical-resistivity model for polycrystalline films: the case of arbitrary reflection at external surfaces. *Physical Review B*, 1:1382–1389, 1970.

[86] K. Fuchs. The conductivity of thin metallic films according to the electron theory of metals. *Proc. Cambridge Philos. Soc.*, 34:100, 1937.

[87] Y.-M. Lin. *Thermoelectric Properties of $Bi_{1-x}Sb_x$ Nanowires and Lead Salt Superlattice Nanowires*. PhD thesis, Massachusetts Institute of Technology, 2003.

[88] Mobay Chemical Corporation. Product information - Makrofol, 2012.

[89] Mitsubishi Corporation. Data sheet and web presence: `http://www.m-petfilm.com/america/PetData.htm`, 2012.

[90] W.-M. Yao et al. Passage of particles through matter. *Journal of Physics G*, 33:258–270, 2006.

[91] M. M. Meier and G. Reitz. Determination of charge states of single swift heavy projectiles by high-energy delta-electrons. *Radiation Measurements*, 34:281–285, 2001.

110

[92] C. Trautmann, S. Bouffard, and R. Spohr. Etching threshold for ion tracks in polyimide. *Nuclear Instruments and Methods in Physics Research Section B*, 116:429–433, 1996.

[93] J. F. Ziegler. Srim-2003. *Nuclear Instruments and Methods in Physics Research Section B*, 219–220:1027–1036, 2004.

[94] R. L. Fleischer, P. B. Price, and R. M. Walker. Ion explosion spike mechanism for formation of charged-particle tracks in solids. *Journal of Applied Physics*, 36:3645–3652, 1965.

[95] Z. G. Wang, Ch. Dufour, E. Paumier, and M. Toulemonde. The S_e sensitivity of metals under swift-heavy-ion irradiation: a transient thermal process. *Journal of Physics: Condensed Matter*, 6:6733–6750, 1994.

[96] C. Trautmann, W. Brüchle, R. Spohr, J. Vetter, and N. Angert. Pore geometry of etched ion tracks in polyimide. *Nuclear Instruments and Methods in Physics Research B: Beam Interactions with Materials and Atoms*, 111: 70–74, 1996.

[97] T. W. Cornelius, B. Schiedt, D. Severin, G. Pépy, M. Toulemonde, P. Yu. Apel, P. Boesecke, and C. Trautmann. Nanopores in track-etched polymer membranes characterized by small-angle x-ray scattering. *Nanotechnology*, 21:155702–1–7, 2010.

[98] W. Ensinger and P. Vater. Diameter distributions of metallic nanowires formed by galvanic deposition inside polymer matrix pores. *Materials Science and Engineering C*, 25:609–613, 2005.

[99] W. DeSorbo. Ultraviolet effects and aging effects on etching characteristics of fission tracks in polycarbonate film. *Nuclear Tracks*, 3:13–32, 1979.

[100] C. G. Zoski (editor). *Handbook of Electrochemistry*. Elsevier, 2007.

[101] M. E. Toimil Molares, N. Chtanko, T. W. Cornelius, D. Dobrev, I. Enculescu, R. H. Blick, and R. Neumann. Fabrication and contacting of single Bi nanowires. *Nanotechnology*, 15:S201–S207, 2004.

[102] L. Li, G. Li, Y. Zhang, Y. Yang, and L. Zhang. Pulsed Electrodeposition of Large-Area, Ordered $Bi_{1-x}Sb_x$ Nanowire Arrays from Aqueous Solutions. *Journal of Physical Chemistry B*, 108:19380–19383, 2004.

[103] E. Budevski, G. Staikov, and W. J. Lorenz. *Electrochemical Phase Formation and Growth*. VCH, 1996.

Bibliography

[104] C. H. Hamann and W. Vielstich. *Elektrochemie.* Wiley-VCH, Weinheim, 2005.

[105] Alan M. Bond, M. Fleischmann, and J. Robinson. Electrochemistry in organic solvents without supporting electrolyte using platinum microelectrodes. *Journal of Electroanalytical Chemistry*, 168:299–312, 1984.

[106] Alan M. Bond, Darryl Luscombe, Keith B. Oldham, and Cynthia G. Zoski. A comparison of the chronoamperometric response at inlaid and recessed disc microelectrodes. *Journal of Electroanalytical Chemistry*, 249:1–14, 1988.

[107] Alan M. Bond, Keith B. Oldham, and Cynthia G. Zoski. Theory of electrochemical processes at an inlaid disc microelectrode under steady-state conditions. *Journal of Electroanalytical Chemistry*, 245:71–104, 1988.

[108] Koichi Aoki and Janet Osteryoung. Diffusion-controlled current at the stationary finite disk electrode. *Journal of Electroanalytical Chemistry*, 122: 19–35, 1981.

[109] David Shoup and Attila Szabo. Chronoamperometric current at finite disk electrodes. *Journal of Electroanalytical Chemistry*, 140:237–245, 1982.

[110] Keith B. Oldham, Jan C. Myland, and Jerome Spanier. *An atlas of functions: with Equator, the atlas function calculator.* Springer Verlag, 2009.

[111] Kourosh Malek and Marc-Olivier Coppens. Knudsen self- and Fickian diffusion in rough nanoporous media. *Journal of Chemical Physics*, 119:2801–2811, 2003.

[112] Oliver Picht. *Growth and Characterization of Bismuth Telluride Nanowires.* PhD thesis, University of Heidelberg, 2010.

[113] T. W. Cornelius, P. Yu. Apel, B. Schiedt, C. Trautmann, M. E. Toimil-Molares, S. Karim, and R. Neumann. Investigation of nanopore evolution in ion track-etched polycarbonate membranes. *Nuclear Instruments and Methods in Physics Research Section B*, 265:553–557, 2007.

[114] Yan He, Dirk Gillespie, Dezsö Boda, Ivan Vlassiouk, Robert S. Eisenberg, and Zuzanna S. Siwy. Tuning transport properties of nanofluidic devices with local charge inversion. *Journal of the American Chemical Society*, 131: 5194–5202, 2009.

[115] Xincun Dou, Yonggang Zhu, Xiaohu Huang, Liang Li, and Guanghai Li. Effective deposition potential induced size-dependent orientation growth of

Bi-Sb alloy nanowire arrays. *The Journal of Physical Chemistry B*, 110: 21572–21575, 2006.

[116] J. H. Hubbell and S. M. Seltzer. Tables of X-Ray Mass Attenuation Coefficients and Mass Energy-Absorption Coefficients from 1 keV to 20 MeV for Elements $Z = 1$ to 92 and 48 Additional Substances of Dosimetric Interest, 2004. URL `http://www.nist.gov/pml/data/xraycoef/index.cfm`.

[117] David B. Williams and C. Barry Carter. *Transmission Electron Microscopy: A Textbook for Materials Science.* Springer, 2009.

[118] Masashi Watanabe, Zenji Horita, and Minoru Nemoto. Absorption correction and thickness determination using the ζ factor in quantitative X-ray microanalysis. *Ultramicroscopy*, 65:187–198, 1996.

[119] M. Watanabe and D. B. Williams. The quantitative analysis of thin specimens: a review of progress from the Cliff-Lorimer to the new ζ-factor methods. *Journal of Microscopy*, 221:89–109, 2006.

[120] N. Peranio and O. Eibl. Quantitative EDX microanalysis of Bi_2Te_3 in the TEM. *physica status solidi (a)*, 204:3243–3255, 2007.

[121] Nicola Peranio. *Structural, chemical, and thermoelectric properties of Bi_2Te_3 Peltier materials: bulk, thin films, and superlattices.* PhD thesis, University of Tübingen, 2008.

[122] P. F. Schmidt. *Praxis der Rasterelektronenmikroskopie und Mikrobereichsanalyse.* Expert Verlag, 1994.

[123] J. A. Bearden. X-ray wavelengths. *Reviews of Modern Physics*, 39:78–124, 1967.

[124] Günter Zschornack. *Atomdaten für die Röntgenspektralanalyse – Tafel 1*, pages 174–244. VEB Deutscher Verlag für Grundstoffindustrie (Leipzig), 1989.

[125] T. P. Schreiber and A. M. Wims. Relative intensity factors for K, L and M shell X-ray lines. *X-Ray Spectrometry*, 11:42–45, 1982.

[126] D. Drouin, A. R. Couture, D. Joly, X. Tastet, V. Aimez, and R. Gauvin. CASINO V2.42—A Fast and Easy-to-use Modeling Tool for Scanning Electron Microscopy and Microanalysis Users. *Scanning*, 29:92–101, 2007.

Bibliography

[127] G. Hölzer, M. Fritsch, M. Deutsch, J. Härtwig, and E. Förster. $K_{\alpha1,2}$ und $K_{\beta1,3}$ x-ray emission lines of the $3d$ transition metals. *Physical Review A*, 56: 4554–4568, 1997.

[128] Theo Hahn, editor. *International Tables for Crystallography Volume A: Space-Group Symmetry*. Springer, 2005.

[129] T. Ungár. Microstructural parameters from X-ray diffraction peak broadening. *Scripta Materialia*, 51:777–781, 2004.

[130] T. Ungár, J. Gubicza, G. Ribárik, and A. Borbély. Crystallite size distribution and dislocation structure determined by diffraction profile analysis: principles and practical application to cubic and hexagonal crystals. *Journal of Applied Crystallography*, 34:298–310, 2001.

[131] Rudolf Allmann and Arnt Kern. *Röntgenpulverdiffraktometrie: Rechnergestützte Auswertung, Phasenanalyse und Strukturbestimmung*. Springer, 2003.

[132] D. Y. Li and J. A. Szpunar. A Monte Carlo simulation approach to the texture formation during electrodeposition—II. Simulation and experiment. *Electrochimica Acta*, 42:47–60, 1997.

[133] A. L. Patterson. The Scherrer Formula for X-Ray Particle Size Determination. *Physical Review*, 56:978–982, 1939.

[134] S. Lele and T. R. Anantharaman. Influence of crystallite shape on particle size broadening of Debye-Scherrer reflections. *Proceedings of the Indian Academy of Sciences, Section A*, 64:261–274, 1966.

[135] Debra L. Kaiser and Robert L. Watters, Jr. Certificate of analysis: Standard Reference Material 1976a. *NIST Certificate*, 2008.

[136] U. Shmueli, editor. *International Tables for Crystallography Volume B: Reciprocal Space*. Kluwer Academic Publishers, 2001.

[137] G. Caglioti, A. Paoletti, and F. P. Ricci. Choice of collimators for a crystal spectrometer for neutron diffraction. *Nuclear Instruments*, 3:223–228, 1958.

[138] W. H. Hall. X-Ray Line Broadening in Metals. *Proceedings of the Physical Society. Section A*, 62:741–743, 1949.

[139] G. K. Williamson and W. H. Hall. X-ray line broadening from filed aluminium and wolfram. *Acta Metallurgica*, 1:22–31, 1953.

114

[140] A. R. Stokes. A Numerical Fourier-analysis Method for the Correction of Widths and Shapes of Lines on X-ray Powder Photographs. *Proceedings of the Physical Society*, 61:382–391, 1948.

[141] T. Ungár and A. Borbély. The effect of dislocation contrast on x-ray line broadening : A new approach to line profile analysis. *Applied Physics Letters*, 69:3173–3175, 1996.

[142] B. E. Warren and B. L. Averbach. The Separation of Cold-Work Distortion and Particle Size Broadening in X-Ray Patterns. *Journal of Applied Physics*, 23:497–498, 1952.

[143] R. de P. Daubeny and C. W. Bunn. The Crystal Structure of Polyethylene Terephthalate. *Proceedings of the Royal Society A*, 226:531–542, 1954.

[144] N. S. Murthy, K. Zero, and H. Minor. Resolution Enhancement of Polymer X-ray Diffraction Scans Using Maximum Entropy Methods: Poly(ethylene terephthalate). *Macromolecules*, 27:1484–1488, 1994.

[145] L. S. Sharath Chandra, Archana Lakhani, Deepti Jain, Swati Pandya, P. N. Vishwakarma, Mohan Gangrade, and V. Ganesan. Simple and precise thermoelectric power measurement setup for different environments. *Review of Scientific Instruments*, 79:103907–1–5, 2008.

[146] David R. Lide. *CRC handbook of chemistry and physics: a ready-reference book of chemical and physical data.* CRC Press, 1992.

[147] J. Heremans, C. M. Thrush, Yu-Ming Lin, S. B. Cronin, and M. S. Dresselhaus. Transport properties of antimony nanowires. *Physical Review B*, 63: 085406–1–8, 2001.

[148] L. Harris and F. B. Corrigan. The mean free paths for the carriers in antimony. *Journal of Physics and Chemistry of Solids*, 26:307–310, 1965.

[149] J. Heremans, C. M. Thrush, Y.-M. Lin, S. Cronin, Z. Zhang, and M. S. Dresselhaus. Bismuth nanowire arrays: Synthesis and galvanomagnetic properties. *Physical Review B*, 61:2921–2930, 2000.

[150] T. W. Cornelius, M. E. Toimil-Molares, R. Neumann, and S. Karim. Finite-size effects in the electrical transport properties of single bismuth nanowires. *Journal of Applied Physics*, 100:114307–1–5, 2006.

[151] Y.-M. Lin, S. B. Cronin, O. Rabin, J. Y. Ying, and M. S. Dresselhaus. Transport properties of $Bi_{1-x}Sb_x$ alloy nanowires synthesized by pressure injection. *Applied Physics Letters*, 79:677, 2001.

Bibliography

[152] Oliver Picht, Sven Müller, Ina Alber, Markus Rauber, Jessica Lensch-Falk, Douglas L. Medlin, Reinhard Neumann, and Maria Eugenia Toimil-Molares. Tuning the Geometrical and Crystallographic Characteristics of Bi_2Te_3 Nanowires by Electrodeposition in Ion-Track Membranes. *The Journal of Physical Chemistry C*, 116:5367–5375, 2012.

[153] H. J. Goldsmid. The Electrical Conductivity and Thermoelectric Power of Bismuth Telluride. *Proceedings of the Physical Society*, 71:633–646, 1958.

[154] Jongmin Lee, Yunseok Kim, Laurent Cagnon, Ulrich Gösele, Jaeyoung Lee, and Kornelius Nielsch. Power factor measurements of bismuth telluride nanowires grown by pulsed electrodeposition. *physica status solidi (RRL)*, 4:43–45, 2010.

[155] F. Völklein, M. Schmitt, T. W. Cornelius, O. Picht, S. Müller, and R. Neumann. Microchip for the Measurement of Seebeck Coefficients of Single Nanowires. *Journal of Electronic Materials*, 38:1109–1115, 2009.

[156] T. W. Cornelius, M. E. Toimil-Molares, S. Karim, and R. Neumann. Oscillations of electrical conductivity in single bismuth nanowires. *Physical Review B*, 77:125425–1–6, 2008.

[157] M. Rauber, I. Alber, S. Müller, R. Neumann, O. Picht, C. Roth, A. Schökel, M. E. Toimil-Molares, and W. Ensinger. Highly-Ordered Supportless Three-Dimensional Nanowire Networks with Tunable Complexity and Interwire Connectivity for Device Integration. *Nano Letters*, 11:2304–2310, 2011.

[158] P. Apel. Swift ion effects in polymers: industrial applications. *Nuclear Instruments and Methods in Physics Research Section B*, 208:11–20, 2003.

Erklärung

Ich versichere, dass ich diese Arbeit selbständig verfasst und keine anderen als die angegebenen Quellen und Hilfsmittel benutzt habe.

Darmstadt, den 03.05.2012